# Strong Shock Wave Generation by Fast Electron Energy Deposition in Shock Ignition Relevant Plasmas

Thomas Edward Fox

Doctor of Philosophy

University of York
Physics

June 2014

# Abstract

The potential role of fast electrons is one of the major unknowns in shock ignition inertial confinement fusion. Of particular interest is the possibility that they may play a beneficial role in the generation of the ignitor shock by contributing to the ablation pressure. Here, some of the fundamental relations governing fast electron driven shock wave generation in dense plasmas are determined. To that end, a 1D planar hybrid model of fast electron transport through dense plasmas is presented. It is found that, using quasi-realistic electron populations, it is possible to generate shock waves with peak pressures that agree with a simple scaling law and have sustained shock pressures of several hundred Mbars. However, the spatial and temporal scales required for shock waves to fully develop increase with fast electron temperature and can become significant. Careful consideration of this effect is needed when assessing their usefulness as shock wave drivers.

A characteristic time of shock wave formation is reinterpreted as the definitive time taken for a localised source of internal energy in an otherwise uniform fluid to drive a blast wave containing its maximum kinetic energy. This relation is of utility in inertial confinement fusion where ignition relies on the conversion of kinetic energy to internal energy at implosion stagnation. However, it is not straightforwardly reproducible by fast electron heating, which highlights the difficulties that may be encountered if fine control over shock wave formation is required.

The shape of the density profile seems to be of secondary importance when compared with the consequences of heating using hotter electron populations. When heating times are on the time scale of the ignitor pulse, the density profile affects the efficiency of shock wave formation by determining the transition from an explosive regime to a driven regime of shock wave formation. However, the time taken for the shock wave to contain its maximum kinetic energy is not significantly affected.

It is shown that an externally applied magnetic field can constrain the range of fast electrons in solid density planar plastic targets, and enhance localised energy deposition. This mitigates the need for significant spatial and temporal scales when using fast electron populations with extended energy distributions to drive shock waves. However, this comes at the expense of the strength of the shock wave.

*per ardua ad astra*

# Contents

# List of Figures

# List of Tables

# Acknowledgements

The completion of this thesis would not have been possible without the help, guidance and support of a large number of people, to all of whom I will always be grateful.

To my supervisors, John Pasley and Alex Robinson whose enduring warmth, patience and encouragement have enabled this work to be accomplished; their advice will forever guide me. To Nathan Sircombe and Stephen Hughes at AWE for their support and to AWE itself for funding my studies. To my advisory panel member Roland Kröger for his guidance on my future.

To the plasma physics group at the CLF, Peter Norreys, Holger Schmitz, Robbie Scott, Raoul Trines and Tony Bell, who always made me feel welcome and whose continued advice has been greatly appreciated. To other members of the CLF, David Neely and Bob Bingham for many enthusiastic discussions. To my doctoral training comrades Peta, Lucy, Graeme and Dean for their empathy and for exploring my silly questions with me.

To my parents whose continued love and support has sustained me throughout my endeavours; I could never have reached this far without them. To my siblings for pulling me back to the real world when I needed it and finally, a very special thank you to Mark for choosing to walk this path with me.

# Declaration

I declare that the work presented in this thesis is based on my own research and has not previously been submitted for a degree at this or any other university. The work was supervised by Dr Alex Robinson (RAL) and Dr John Pasley (Univ. of York). Since all of the work was carried out on-site at RAL, Dr Robinson has been principally responsible for supervising the work described here-within. I am responsible for the development of the hybrid model presented in Chapter 3, and for obtaining and interpreting the results presented in Chapters 5 through 8. The model represents an amalgamation of standard 'textbook' numerical algorithms, modified versions of algorithms found in peer reviewed journals, and algorithms that I developed. Where an external source has been used, that source is clearly cited. Where work has been published as an article in a peer reviewed journal, it is clearly identified as such. The following is a list of the publications resulting from the work described here-within:

T. E. Fox, A. P. L. Robinson, H. Schmitz, J. Pasley, *"Characterising the Acceleration Phase of Blast Wave Formation",* submitted to Physics of Plasmas,

T. E. Fox, A. P. L. Robinson, J. Pasley, *"Strong shock generation by fast electron energy deposition",* Phys. Plasmas, **20**, 122707 (2013),

T. E. Fox, A. P. L. Robinson, J. Pasley, *"Development and Validation of a 1D2V Vlasov-Fokker-Planck Model",* Theory and Computation Report, Central Laser Facility, UK, Annual Report 2011-2012.

Thomas Edward Fox

# Chapter 1

# Introduction

## 1.1 Motivation for Fusion Energy

The World Energy Council, the UN-accredited global energy body, predicts that the global population could increase by nearly 2.5 billion people by the year 2050 [1]. This astonishing figure represents a 36% increase over three and a half decades. By considering factors such as increased wealth and access to energy supplies, the World Energy Council predicts that the global energy demand will correspondingly increase by up to 61%. Despite advances in renewable energy technology, the Council warns that this demand will be met primarily by fossil fuels and that global $CO_2$ emissions targets are unlikely to be met without stricter global agreements and potentially unacceptable carbon pricing. If realised, controlled fusion energy has the potential to ease this energy crisis by offering a complementary method of generating useful energy that is clean, safe, abundant and secure.

A number of approaches to achieving controlled fusion energy are currently being explored. This thesis is concerned with one of the more dominant approaches called inertial confinement fusion. First proposed in 1972 [2], the field of inertial confinement fusion by laser compression of fusion targets has matured over the decades to the point where facilities exist, such as the National Ignition Facility [3, 4], or are nearing completion, such as the Laser Megajoule Facility [5–7], that may be capable of demonstrating ignition of inertial confinement fusion targets for the first time.

Within the field of inertial confinement fusion, there are a number of different schemes such as indirect-drive [8], conventional central hot spot ignition [2], fast ignition [9] and shock ignition [10]. These differ in their details and their technological requirements but all share some fundamental similarities. That is, in each scheme a spherical fusion target made of cryogenic deuterium-tritium is uniformly irradiated by electromagnetic radiation and compressed to high densities, a hot spot is created where ignition occurs and from which thermonuclear burn can spread. Thermonuclear burn is spread primarily by alpha particle energy deposition while the bulk of the neutron energy is captured by a thermal blanket and is then extracted via a coolant and power production proceeds in a conventional manner.

The body of work presented in this thesis is conducted in the context of shock ignition, which, being proposed as recently as 2007 [10], is the relative newcomer to the ensemble of inertial confinement fusion schemes. As the reader will discover in the following chapters, shock ignition relies on the generation of shock waves of varying strengths to compress the spherical target to high densities and to create the conditions required for ignition. The laser parameters required to perform the latter are sufficient to stimulate parametric instabilities and the generation of suprathermal electron populations [11]. The potential role of these hot electron populations in shock wave formation and their implication for shock ignition are the focus of this thesis.

## 1.2 Thesis Outline

This thesis concerns the development and application of a hybrid model of relativistic electron transport through dense plasmas to the problem of relativistic electron driven shock wave generation in the context of shock ignition inertial confinement fusion. The numerical model is detailed in Chapter 3 and the subsequent chapters explore the problem at hand.

**Chapter 2 - Background:** A brief introduction to the hydrodynamic, kinetic and hybrid descriptions of plasmas is given. This focusses on the governing equations and the assumptions that are made in each description. This is followed by an introduction to inertial confinement fusion and the shock ignition scheme in particular, and a discussion of external studies on fast electron driven shock waves in dense plasmas.

**Chapter 3 - Numerical Solution of the Model** The motivation for developing a hybrid model is reasoned and its limitations are discussed. This is followed by a detailed description of the numerical algorithms used in the model.

**Chapter 4 - A Précis of Electron Generation in the Context of the Shock Ignition Regime:** A précis of recent numerical and experimental results pertaining to fast electron generation in the shock ignition regime is given. This motivates our choice of fast electron populations in the following chapters.

**Chapter 5 - The Effect of Extended Energy Distributions on Shock Peak Pressure:** A comparison of shock wave generation by electron populations with monoenergetic and Maxwellian energy distributions is presented. It will be shown that they produce equivalent peak pressures in the shock waves and that the peak pressure obeys a simple scaling law. The crucial difference between the two scenarios is the time taken for the peak pressure to be achieved, with Maxwellian populations taking significantly longer due to their more extended energy deposition profiles in step-like targets. This work has been published in Fox et al. [12].

**Chapter 6 - On the Characteristic Time Scale of Explosive Shock Wave Generation:** A long recognised characteristic timescale of blast wave formation in a uniform fluid is given a more definitive interpretation as the time taken for a localised source of internal energy to drive a blast wave containing it maximum amount of kinetic energy. This scaling is confirmed using the hydrodynamic module of the hybrid model. The difficulties encountered when trying to reproduce the scaling by fast electron energy deposition in step-like targets are discussed. As of May 2014, this work has been submitted to Physics of Plasmas.

**Chapter 7 - The Effect of Density Profile on Shock Wave Formation:** The effect of the target density profile on the fast electron deposition profile and subsequent shock wave formation is assessed. It will be shown that while any deviation from a step-like profile is detrimental to the efficiency of shock wave formation, it should be possible to manage this effect in a shock ignition scheme design.

**Chapter 8 - Shock Wave Formation in Magnetised Targets:** A preliminary study on enhancing localised fast electron energy deposition using externally applied strong magnetic fields has demonstrated that the spatial and temporal scales required to generate shock waves using electron populations with extended energy distributions can be reduced. However, this is achieved at the expense of the strength of the shock wave.

**Chapter 9 - Conclusions:** The results of the preceding chapters are summarised and their implications for shock ignition are discussed. Potential extensions or adaptations of the work presented in this thesis are briefly discussed.

# Chapter 2

# Background

## 2.1 Introduction

The body of work presented in this thesis bridges several vast areas of physics including the fundamental theory of plasma physics, fluid theory, shock waves, relativistic particle transport and inertial confinement fusion. It is not possible to do justice to each of these areas here as one could write volumes on each. As such, only the most salient points from each topic will be presented and, in lieu of a more detailed treatise, the reader will be directed to excellent references for further study.

This chapter proceeds with an overview of the fluid and kinetic descriptions of a plasma and how their combination in a hybrid description allows for the modelling of problems with a large dynamic range. It will become apparent that such a capability is desirable when modelling fast electron transport through dense plasmas. En route, the fundamentals of shock wave physics will be introduced. The importance of shock waves and fast electron transport is then highlighted in a discussion of the conventional central hotspot ignition and shock ignition schemes. Finally, a summary of external studies on the role of fast electrons in shock ignition is given.

## 2.2 Fluid Theory

A plasma consists of at least two species, electrons and ions, with opposite charges and very different masses. These properties can give rise to phenomena that do not occur in neutral fluids [13]. However, a single-fluid description of a plasma is acceptable in many situations and is widely used. This involves representing the plasma as a set of average macroscopic hydrodynamic quantities that are continuous in space and time. These quantities are mass density $\rho$, fluid velocity $\mathbf{u}$ and total energy density $e$. For these quantities to be smooth functions in space and time requires that the phenomena of interest vary on length scales that are much greater than the mean inter-particle distance and times scales much larger than the mean inter-particle collision time. This leads naturally to the concept of a fluid element. A fluid element is a volume of fluid that is small enough that the hydrodynamic quantities vary negligibly across it and the fluid can be described by average quantities, but large enough that it contains so many particles as to be insensitive to particle fluctuations.

By considering the conservation of the hydrodynamic quantities within a fluid element one obtains the single-fluid hydrodynamic equations [14]:

$$\frac{\partial \rho}{\partial t} + \nabla.(\rho \mathbf{u}) = 0, \tag{2.1a}$$

$$\rho \left( \frac{\partial u}{\partial t} + (\mathbf{u}.\nabla)\mathbf{u} \right) + \nabla P = 0, \tag{2.1b}$$

and

$$\frac{\partial e}{\partial t} + \nabla. \left[ (e + P)\, \mathbf{u} \right] = 0, \tag{2.1c}$$

where $P$ is the thermal pressure. This set of equations is closed with an equation of state such as that for an ideal gas with an adiabatic index $\gamma$:

$$P = (\gamma - 1)\left(e - \frac{1}{2}\rho|\mathbf{u}|^2\right). \tag{2.2}$$

It is equally possible to derive the fluid equations formally from the kinetic description of a plasma. Although this is a rather involved process, it does serve to highlight the assumptions made and the information lost by choosing a fluid model over the full kinetic description. That is, by adopting a fluid model one resigns oneself to working with average, macroscopic quantities whilst losing all of the microscopic information related to the distribution of momenta of the particles within a fluid element.

In laser-plasma interactions, it is not uncommon for the electron and ion temperatures to differ greatly. In such a case it is preferable to treat the electrons and ions with distinct temperatures. As will be shown in Section 3.5.2, this amounts to adding another equation to Eqs. 2.1:

$$\frac{\partial r}{\partial t} + u\frac{\partial r}{\partial x} = 0, \tag{2.3}$$

where $r$ is the fraction of total internal energy density associated with the electrons. With two distinct temperatures, one can consider thermal conduction and electron-ion thermal equilibration. This brings the discussion of fluid models to another of their limitations. It is necessary to prescribe additional models to include physics such as resistivity and thermal conductivity. These can be from a theoretical model (Spitzer resistivity [15] or Lee-More [16]), an empirical model, or a heuristic model. See Section 3.5 for a discussion of the prescriptions used in the hybrid model and the numerical schemes employed to solve them. Section 3.5 also details the numerical scheme used to solve Eqs. 2.1 and 2.3.

### 2.2.1 Shock Waves

The solutions to the hydrodynamic equations may be discontinuous. This means that, in theory at least, the hydrodynamic variables may change discontinuously or have discontinuous spatial

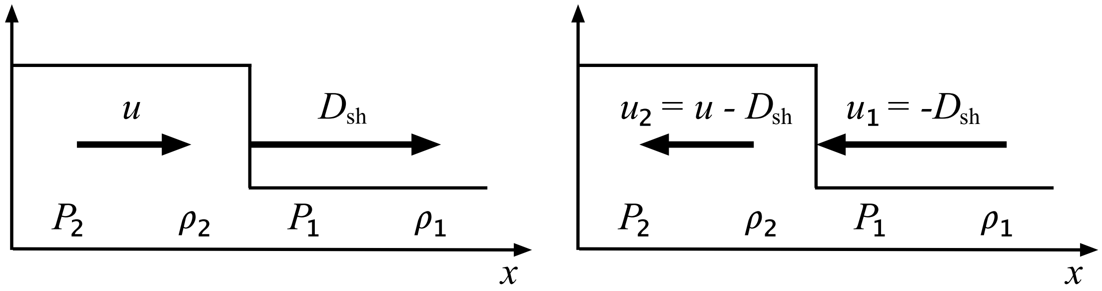

**(a) Laboratory frame** **(b) Shock rest frame**

**Figure 2.1: Schematics of a shock wave in the laboratory frame (Fig. 2.1a) and in its rest frame (Fig. 2.1b), and the pre- and post-shock nomenclature. In the laboratory frame, the shock wave travels at velocity $D_{sh}$ into undisturbed, stationary pre-shock fluid that has density $\rho_1$ and pressure $P_1$. Upon passage of the shock front, the fluid is accelerated to velocity $u$ and has density $\rho_2$ and pressure $P_2$. In the rest frame of the shock, the pre-shock fluid moves with velocity $u_1$ towards the shock front and the post-shock fluid has velocity $u_2$.**

derivatives. These solutions are called shocks. Their importance to inertial confinement fusion in general and to shock ignition specifically is discussed in Section 2.5. This section is limited to the fundamental properties of shock waves in a polytropic gas that are relevant to that discussion. For extensive studies on the subject of shock waves see, for example, Refs. 17 and 18.

Figure 2.1 shows the convention used when discussing the hydrodynamic variables pre- and post-shock. Consideration of the conservation laws across the shock leads to the Rankine-Hugoniot relations, which relate the pre- and post-shock hydrodynamic quantities when $\gamma$ is constant across the shock:

$$\frac{\rho_2}{\rho_1} = \frac{u_1}{u_2} = \frac{(\gamma+1)\frac{P_2}{P_1} + (\gamma-1)}{(\gamma+1) + (\gamma-1)\frac{P_2}{P_1}}, \tag{2.4}$$

and

$$\frac{P_2}{P_1} = \frac{(\gamma+1)\rho_2 - (\gamma-1)\rho_1}{(\gamma+1)\rho_1 - (\gamma-1)\rho_2}, \tag{2.5}$$

where $\gamma = C_p/C_V$ is the ratio of specific heats. In the limit of a strong shock, $P_2 \gg P_1$ and Eq. 2.4 yields,

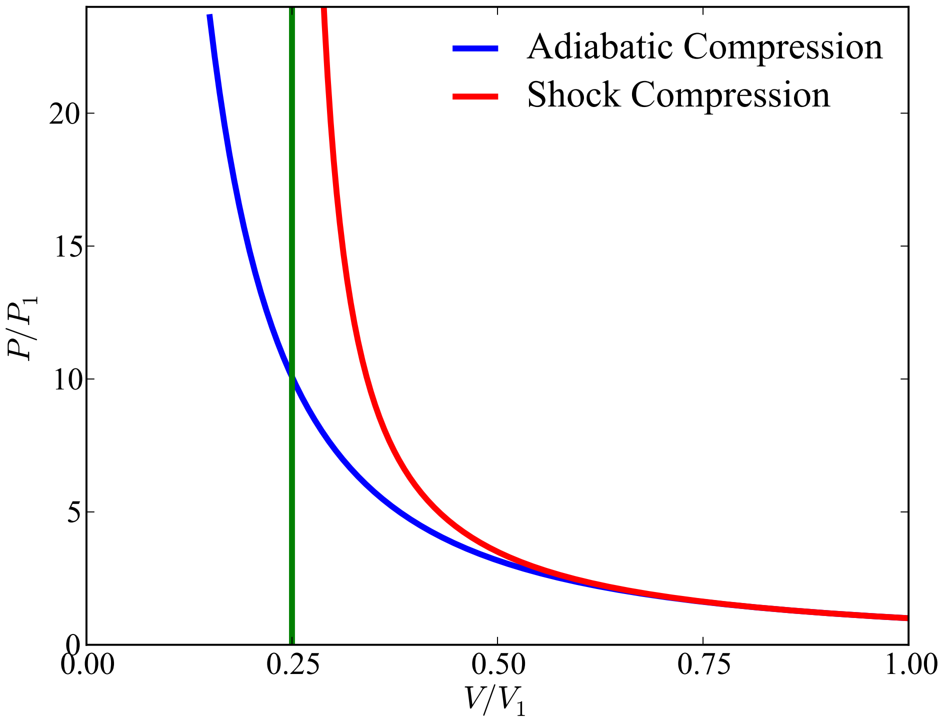

**Figure 2.2: A comparison of the final states that are accessible to an ideal gas with $\gamma = 5/3$ and described by the state $(P_1, V_1)$, under pure adiabatic (blue) and shock (red) compression are shown. In the limit of a weak shock the two curves agree but as the shock strength increases, the entropy generated under shock compression limits the achievable compression to a factor of four. This limit is indicated by a green line.**

$$\frac{\rho_2}{\rho_1} = \frac{u_1}{u_2} = \frac{\gamma + 1}{\gamma - 1}. \tag{2.6}$$

Thus, in contrast to purely adiabatic compression which can achieve arbitrarily high compression ratios, shock compression has an upper bound. For a monatomic gas, with $\gamma = 5/3$, a single shock can increase the density by, at most, a factor of four. This is demonstrated in Fig. 2.2, where the final states that are accessible to an ideal gas with $\gamma = 5/3$ and described by the state $(P_1, V_1)$, under pure adiabatic (blue) and shock (red) compression are shown. Here, $V$ represents volume. In the limit of a weak shock the two curves agree but as the shock strength increases, the entropy generated under shock compression limits the achievable compression to a factor of four.

From Eqs. 2.4 and 2.5 one can write the change in entropy brought about by the passage of the shock as,

$$S_1 - S_0 = C_V \ln\left(\frac{P_2 \rho_1^\gamma}{P_1 \rho_2^\gamma}\right) = C_V \ln\left(\frac{P_2}{P_1}\left[\frac{(\gamma+1)+(\gamma-1)\frac{P_2}{P_1}}{(\gamma+1)\frac{P_2}{P_1}+(\gamma-1)}\right]^\gamma\right). \tag{2.7}$$

Thus a shock is a non-reversible, dissipative process that acts to increase the entropy of the fluid it is passing through by converting ordered kinetic energy into random thermal energy. This is a particularly salient point to the discussion on shock ignition in Section 2.5.

Radiation transport can play an important role in determining the nature of the shock front. The radiation flux is proportional to $T^4$, so radiation transport can become significant at high temperatures and remove energy from the shock wave. The long mean free path and high speed of the photons mean that they can propagate ahead of the shock wave and pre-heat the pre-shock fluid. This broadens the shock front structure such that the classical step-like description of a shock front depicted in Fig. 2.1 is no longer valid. Radiation transport is not included in the hybrid model. The implications of this for the studies presented in this thesis are discussed in Section 5.6, where it is argued that radiation transport, had it been included, would not greatly affect the conclusions of this thesis.

## 2.3 Kinetic Theory

A fluid description is macroscopic and represents the fluid variables as functions of space and time but loses all information about the distribution of particle momenta in a fluid element. Any physical properties of the plasma that rely on this microscopic information can only be captured by a description in six-dimensional $(\mathbf{r}, \mathbf{p})$ space. This leads to the idea of a distribution function, $f(\mathbf{r}, \mathbf{p}, t)$, which is the number density of particles in the infinitesimal volume of phase-space $(\mathrm{d}\mathbf{r}, \mathrm{d}\mathbf{p})$ at time $t$. The evolution of this distribution function is described by kinetic theory. For extensive treatments of kinetic theory see Refs. 13 and 19.

Assuming that there are no sinks or sources of particles in the system, the evolution of $f$ obeys the continuity equation in phase-space,

$$\frac{\partial f}{\partial t} + \mathbf{v}.\frac{\partial f}{\partial \mathbf{r}} + \mathbf{F}.\frac{\partial f}{\partial \mathbf{p}} = 0, \tag{2.8}$$

where $\mathbf{F}$ is the force acting the particles at the point $(\mathbf{r}, \mathbf{p})$ at time $t$. Equation 2.8 is the collisionless kinetic equation, or more commonly known as the Vlasov equation. By taking moments of the distribution function and applying an argument for closure of the chain of moments, it is possible to derive the fluid equations (Eqs. 2.1) from the Vlasov equation. This exercise serves to highlight the fact that the fluid equations describe the evolution of inherently averaged quantities.

The zeroth order moment of the distribution function defines scalar quantities such as the spatial distribution of the number density of particles as,

$$n(\mathbf{r}) = \int f \; \mathrm{d}\mathbf{p}, \tag{2.9}$$

and the first order moment defines momentum averaged vector properties such as particle fluxes as,

$$\phi = \int \mathbf{v} f \; \mathrm{d}\mathbf{p}. \tag{2.10}$$

In general, the $k^{\text{th}}$ moment, $\mathbf{\Pi}_k$, of the distribution function $f(\mathbf{r}, \mathbf{p}, t)$ is written,

$$\mathbf{\Pi}_k = \int \mathbf{v}\mathbf{v} \cdots \mathbf{v} f \; \mathrm{d}^3\mathbf{p}, \tag{2.11}$$

with $k$ factors of $\mathbf{v}$, $\mathbf{\Pi}_k$ is a tensor of rank $k$ and the integral is performed over all of momentum space. Note that here the order of the moment refers to the tensor rank, while other authors use the order of the moment to refer to the power of the velocity in the integrand. The concept of moments of a distribution function will be revisited in Section 3.4.1.

The effects of collisions on the evolution of $f$ are included by modifying the Vlasov equation in a conceptual way to yield,

$$\frac{\partial f}{\partial t} + \mathbf{v}.\frac{\partial f}{\partial \mathbf{r}} + \mathbf{F}.\frac{\partial f}{\partial \mathbf{p}} = \left(\frac{\partial f}{\partial t}\right)_{coll}, \tag{2.12}$$

where $\left(\frac{\partial f}{\partial t}\right)_{coll}$ represents the change in $f$ due to collisional interactions inside the volume element. The exact form of this term depends on the system being studied and the level of detail desired. The Fokker-Planck collision term is expected to be appropriate for the work undertaken in this thesis.

### 2.3.1 The Fokker-Planck Collision Term

Suppose that $f(\mathbf{r}, \mathbf{p} - \Delta\mathbf{p}, t - \Delta t)$ is the distribution function of electron position and momenta at time $t - \Delta t$. The transition probability for a collision causing a small change in momentum of $\Delta\mathbf{p}$ in time $\Delta t$ is $\psi(\mathbf{p}, \Delta\mathbf{p})$. The distribution function at time $t$ is therefore given by,

$$f(\mathbf{r}, \mathbf{p}, t) = \int f(\mathbf{r}, \mathbf{p} - \Delta\mathbf{p}, t - \Delta t)\psi(\mathbf{p} - \Delta\mathbf{p}, \Delta\mathbf{p})\mathrm{d}(\Delta\mathbf{p}). \tag{2.13}$$

Since $\Delta\mathbf{p}$ is small, the integral in Eq. 2.13 can be expanded as a Taylor series for small deflection collisions in momentum space as,

$$\begin{aligned} f(\mathbf{r}, \mathbf{p}, t) = \int \mathrm{d}(\Delta\mathbf{p}) \Big\{ & f(\mathbf{r}, \mathbf{p}, t - \Delta t)\psi(\mathbf{p}, \Delta\mathbf{p}) - \Delta\mathbf{p}.\frac{\partial f}{\partial \mathbf{p}}(f\psi) \\ & + \frac{1}{2}\Delta\mathbf{p}\Delta\mathbf{p} : \frac{\partial^2 (f\psi)}{\partial \mathbf{p}\partial \mathbf{p}} + \dots \Big\}. \end{aligned} \tag{2.14}$$

Using the fact that,

$$\int \psi \, \mathrm{d}(\Delta\mathbf{p}) = 1, \tag{2.15}$$

and defining the rate of change of $f$ due to collisions by,

$$\left(\frac{\partial f}{\partial t}\right)_{coll} = \frac{f(\mathbf{r},\mathbf{p},t) - f(\mathbf{r},\mathbf{p},t-\Delta t)}{\Delta t} \tag{2.16}$$

one arrives at the Fokker-Planck equation,

$$\left(\frac{\partial f}{\partial t}\right)_{coll} = -\frac{\partial}{\partial \mathbf{p}}\left(\frac{\langle \Delta \mathbf{p} \rangle}{\Delta t} f\right) + \frac{1}{2}\frac{\partial^2}{\partial \mathbf{p}\partial \mathbf{p}}\left(\frac{\langle \Delta \mathbf{p}\Delta \mathbf{p} \rangle}{\Delta t} f\right), \tag{2.17}$$

where,

$$\langle \Delta \mathbf{p} \rangle = \int \psi\left(\mathbf{p}, \Delta \mathbf{p}\right) \Delta \mathbf{p} \, \mathrm{d}\left(\boldsymbol{\Delta}\mathbf{p}\right)$$

and

$$\langle \Delta \mathbf{p}\Delta \mathbf{p} \rangle = \int \psi\left(\mathbf{p}, \Delta \mathbf{p}\right) \Delta \mathbf{p}\Delta \mathbf{p} \, \mathrm{d}\left(\boldsymbol{\Delta}\mathbf{p}\right), \tag{2.18}$$

are the average changes in $\Delta p$ and $\Delta p \Delta p$ in time $\Delta t$. The first term in Eq. 2.17 is known as the coefficient of dynamical friction, and it tends to decelerate high-energy particles and accelerate low-energy particles to the average momentum. The second term in Eq. 2.17 is known as the coefficient of diffusion, and it tends to spread out the range of momenta of the particle population to the equilibrium value.

Equation 2.17 is a general equation that can be applied to a number of physical systems but fundamentally assumes that the cumulative effect of many simultaneous small angle interactions far outweighs the effect of rare large angle interactions and that $\psi(\mathbf{p}, \Delta \mathbf{p})$ is independent of time and has no knowledge of previous interactions, i.e. the deflection process is Markovian. As such the Fokker-Planck equation is best suited to weakly coupled plasmas, i.e. plasmas with a large number of particles in the Debye sphere.

Information about the scattering species is contained within the, yet to be determined, transition probability $\psi(\mathbf{p}, \Delta \mathbf{p})$. Various forms of the Fokker-Planck equation have been derived and the present discussion shall follow the approach presented in Ref. 20 where it is assumed that the effect of many simultaneous weak interactions can be obtained by linear addition of each individual interaction to calculate $\langle \Delta \mathbf{p} \rangle / \Delta t$ and $\langle \Delta \mathbf{p} \Delta \mathbf{p} \rangle / \Delta t$. This discussion will continue in Sections 3.4.6 and 3.4.7 where the exact forms of the collision operators used for electron-ion scattering and electron-electron drag are presented along with arguments for their reduced form used in this thesis.

## 2.4 Hybrid Theory

The propagation of suprathermal electrons, which have much longer mean free paths than the thermal population, through a dense, collisional, relatively cool plasma is of interest in inertial confinement fusion. The dynamic range of this problem makes it difficult to apply a single treatment, and the cold and dense background plasma has such small spatial and temporal scales (e.g. collisional mean free path, Debye length and mean collision time) that make a fully kinetic treatment unfeasible. One solution is to take a hybrid approach in which the background plasma is treated as a fluid with a prescribed resistivity, and the fast electrons are treated fully kinetically and injected into the simulation according to a model for their generation by laser-plasma interaction.

The hybrid approach is only valid under a number of assumptions [21]:

1. The fast electron number density must be small compared to the background number density, i.e. $n_f \ll n_b$, even if the fast electron current $j_f$ is not negligible. In this way, the background plasma can be treated as a distinct, quasi-neutral plasma.

2. In the absence of fast electrons, a fluid description of the background plasma must be valid on the time and length scales of interest. Furthermore, the prescribed resistivity models and thermal transport models should be valid and accurate.

3. Approximate current balance between the fast electron current density and the background

current density should be satisfied, i.e. $j_f + j_b \approx 0$.

4. An Ohm's law needs to be prescribed to describe the electric field. In its simplest form, assuming an Ohm's law is valid [22–24], the electric field is given by $E = \eta j_b$. After considering current balance, this becomes $E = -\eta j_f$, so that the electric field can be found directly from the fast electron current.

If these conditions are satisfied, hybrid models have the advantage of relaxing the small spatial and temporal scales that make a fully kinetic treatment unfeasible. They also reduce Maxwell's equations to just an induction equation which simplifies the overall algorithm. Finally, the general structure of a hybrid model makes it relatively easy to develop, maintain and extend. In the simplest case, the hydrodynamic and kinetic descriptions are coupled in a hybrid model through the Ohm's law resulting in Ohmic heating, and through collisional drag on the fast electrons. These heating mechanisms drive the evolution of the background plasma.

## 2.5 Shock Ignition Inertial Confinement Fusion

The strive for inertial confinement fusion has led to the development of a number of different approaches or schemes as our collective understanding of plasma physics and laser-plasma interactions has developed. The dominant laser driven schemes come under the headings indirect-drive [8] and direct-drive [2]. The latter can be further subdivided into conventional central hotspot ignition [2], fast ignition [9] and shock ignition [10]. Shock ignition is the relative newcomer and is the focus of this thesis. An overview of the conventional central hotspot ignition scheme is given for comparison with the later description of shock ignition. This serves to highlight the advantages of the latter over the former.

The main stages of the conventional central hotspot ignition scheme are shown in Fig. 2.3.

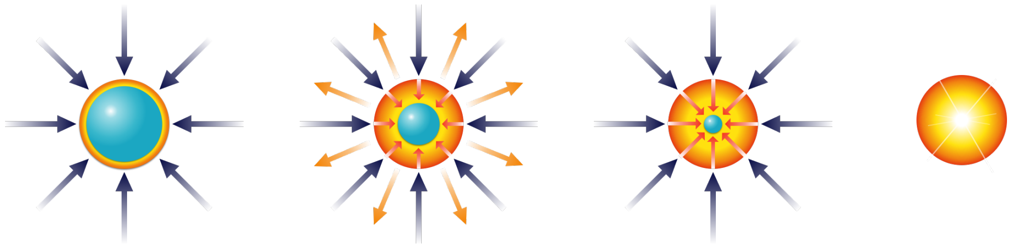

**(a) Corona formation** **(b) Compression** **(c) Ignition** **(d) Burn**

**Figure 2.3: An illustration of the main stages of conventional central hot spot ignition. The target consists of a spherical shell with an outer ablator layer and an inner cryogenic DT layer. The internal volume of the spherical shell is filled with DT gas. The target is uniformly irradiated and accelerated inwards by a series of shock waves. At implosion stagnation, a high density shell surrounds a central hot spot which ignites, sending an outwardly propagating thermonuclear burn wave through the fuel.**

The target consists of a spherical shell with an outer ablator layer and an inner cryogenic DT layer. The internal volume of the spherical shell is filled with DT gas. The target is directly and symmetrically irradiated by a number of lasers. The outer layer of the shell absorbs the radiation and ablates. This creates a plasma corona surrounding the target and prevents the laser from interacting with the target directly (Fig 2.3a). Instead, it couples to electrons in the coronal plasma which transport thermal energy from the critical surface to the ablation surface, and drive further ablation of the target. As a reaction to the expansion of the ablated material, the shell is accelerated inwards by a series of shock waves (Fig. 2.3b).

The accelerated fuel stagnates at the centre where it reaches a high density and is heated by the conversion of its kinetic energy to internal energy. The assembled fuel configuration in conventional central hot spot ignition is isobaric [25]. It consists of a central relatively low density hot spot surrounded by a much denser and colder fuel so that the pressure is nearly uniform across the fuel. This configuration limits power loss by mechanical work done by the hot spot [26]. The central hot spot then ignites (Fig. 2.3c) and a thermonuclear burn wave propagates outwards with the aim of burning a significant fraction of the fuel before it disassembles, i.e. while the fuel is confined by its own inertia (Fig. 2.3d).

This approach, in theory, successfully creates a small central volume of igniting fuel from which burn can spread and efficiently ignite the rest of the fuel. However, a number of issues must be overcome if this is to be achieved with an affordable driver energy [27, 28], including [21],

1. The laser energy should be efficiently coupled to the target to achieve the required implosion velocity. The laser intensity should be high enough to generate a sufficient ablation pressure without being so high as to stimulate parametric instabilities and generate undesirable suprathermal electrons.

2. The energy that is coupled to the target should be used efficiently to achieve the required implosion velocity and compress the fuel. It is desirable to keep the dense fuel as cold as possible during compression as any increase in the thermal back pressure will resist compression. The target can be unduly heated by fast electron penetration (see the previous point) as well as by shock waves (see Section 2.2.1). A single strong shock, generated by a high ablation pressure, would increase the entropy of the fuel too greatly. Instead, a series of not-too-strong shocks are used to accelerate the fuel while approximating adiabatic compression.

3. Spherical symmetry should be maintained during the compression to achieve a symmetric hot spot. Non-uniformities imprinted by the irradiation will introduce non-uniformities into the hot spot and these should be less than 1% [21, 26].

4. Hydrodynamic instabilities, such as the Rayleigh Taylor instability [26] should be minimised as these can affect the symmetry and can also cause mixing of the ablator with the fuel. This can reduce the gain or quench the ignition altogether.

Implosion stability can be improved by reducing the implosion velocity. Assuming that ignition takes place and that the burn wave propagates through the dense fuel, a lower implosion velocity also allows for higher gains [29]. The increased gain comes from being able to assemble more mass for the same laser energy and more massive shells have better hydrodynamic stability. However, one cannot go to arbitrarily low implosion velocities because the energy required for ignition from the central hot spot increases rapidly with decreasing velocity as $E_{ign}^{hs} \sim V_I^{-6}$ [30]. This is because the hot spot temperature increases with velocity and the fusion cross-section is a strong function of temperature. Thus, a solution to achieving reduced susceptibility to hydrodynamic instabilities, low-entropy drive and higher gain is to separate the compression and ignition of the fuel into two phases. Compression can proceed on a low adiabat with a low implosion velocity, and then an igniting hot spot is created by some other heating mechanism.

A proposal to use a converging shock wave to ignite a spherical target that has been compressed to a high density was first put forward in Ref. 31. However, this scheme relied on the shock wave delivering nearly all of the energy needed for ignition, which is unfeasible given current laser technology. A related scheme, known as shock ignition was first proposed in Ref. 10 in 2007 and the first preliminary experiment was reported soon afterwards [32]. In shock ignition, a relatively low laser intensity of a few hundred TW/cm$^2$ is used to create a $\sim$40 Mbar ablation pressure and symmetrically compress a spherical shell target with an implosion velocity of $\sim$250 km/s. This is somewhat slower than conventional central hot spot ignition and results in a central hot spot that is too cold, at 2$-$3 keV, for ignition to occur. A spike in the laser intensity, up to 0.2$-$1 $\times$ 10$^{16}$ W/cm$^2$ with a power of 200$-$400 TW, produces a 300 Mbar ablation pressure that drives a final strong, spherically convergent shock wave. This is carefully timed to meet the coalesced rebounding shock at the interface between the dense fuel and the central region, where it is amplified and delivers the remaining energy to ignite the hot spot. A detailed review of the shock ignition scheme can be found in Refs. 21 and 33. Figure 2.4 is a facsimile of Fig. 4c in Ref. 34

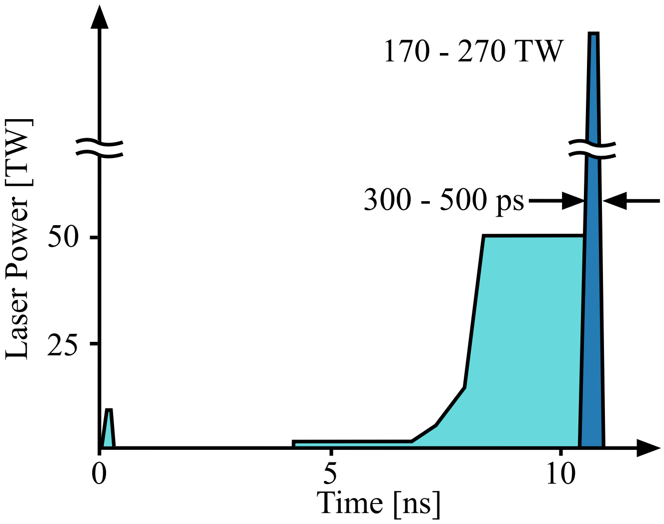

**Figure 2.4: A facsimile of Fig. 4c in Ref. 34 showing the temporal profile of the laser power envisaged for shock ignition of the HiPER baseline target.**

and depicts the temporal profile of the laser power envisaged for shock ignition of the HiPER [35] baseline target [36, 37]. It clearly shows the lower power compression phase followed by a spike in the laser power which launches the final ignitor shock wave.

In contrast to the isobaric configuration produced in conventional central hot spot ignition, the shock ignition scheme produces a non-isobaric configuration which has a lower ignition threshold by roughly a factor of $(P_{\text{non-iso}}/P_{\text{iso}})^3$ [10], where $P_{\text{non-iso}}$ and $P_{\text{iso}}$ are the hot spot pressures in the non-isobaric and isobaric configurations, respectively. In this non-isobaric configuration, the hot spot has a lower density than the surrounding cold, dense fuel but is hotter and has a higher pressure.

Shock ignition is attractive because the relatively low laser intensities and total invested energy mean that it can be tested on existing installations and it offers the potential for a high gain of 100 or more [38, 39], which is necessary for a fusion power plant. This does not mean that shock ignition is without its problems. This thesis is primarily concerned with the consequences of the high intensity of the ignitor pulse. For a detailed review of the physics issues for shock ignition see Ref. 40.

The laser intensity used for compression lies below the threshold for parametric instabilities [11] to dominate the laser-plasma interaction. The laser energy is effectively absorbed by inverse Bremsstrahlung in the plasma corona, with only a relatively small fraction of the energy ($\sim$5%) being coupled to the parametric instabilities. The energy is most efficiently absorbed near the critical density and is transported to high densities by thermal electrons. On the other hand, the ignitor pulse is sufficiently intense that it lies above the threshold and far more energy ($>$25%) may be coupled to the, now more dominant, parametric instabilities. This can affect the efficiency of the laser absorption and can generate hot electron populations. More detail on the generation of hot electrons in shock ignition is given in Chapter 4.

Fast electrons are of great concern in conventional central hotspot ignition because their long mean free paths mean that they are capable of penetrating deep into the assembling fuel, thereby pre-heating it and preventing sufficient compression from taking place. However, in shock ignition, the ignitor pulse comes at the end of the assembly phase so the fast electrons are generated after the fuel has already undergone a significant amount of compression. This is shown in Figure 2.5, which is a facsimile of Fig. 1a in Ref. 41, and shows that the fuel has reached a peak density of $\sim$10 g/cm$^3$ at the time of the ignitor pulse. If the fuel is sufficiently dense, the fast electrons will be stopped in the compressed shell. There they will deposit their energy, contribute to the ablation pressure and help to drive the ignitor shock [10, 31, 39]. Conversely, if the range of the fast electrons is still too great the problem of pre-heat will need to be considered. Ergo, the conditions required for fast electrons to be beneficial to shock ignition need to be assessed and this is the focus of this thesis.

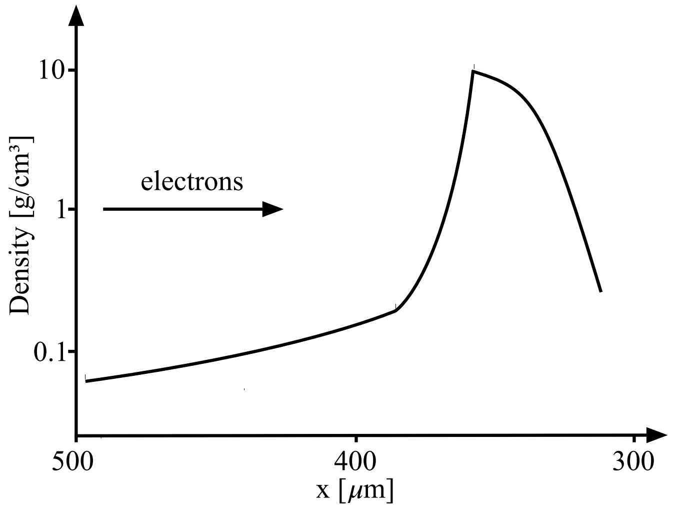

**Figure 2.5: A facsimile of Fig. 1a in Ref. 41 showing the predicted density profile of the HiPER baseline target at the time of the ignitor pulse in shock ignition. The direction of the incoming electrons is also indicated.**

## 2.6 External Studies on the Role of Fast Electrons in Shock Ignition

A study of non-local energy transport in shock ignition [42] found that shock ignition lies on the boundary between the ablative regime where thermal electron diffusion is dominant and the heat front regime where non-local energy transport becomes important. It is argued that non-local effects are significant in shock ignition and that they can increase the efficiency of shock wave generation. However, this study is limited to short times when the heat front regime is applicable. To evaluate the efficacy of fast electrons for shock wave generation one must consider longer electron beams and study the shock wave amplitude over time. Such an initial numerical study on the ability of fast electron populations to drive strong shock waves is presented in Ref. 43, with the accompanying analytic model detailed in Ref. 44. For clarity, the author was not involved in either publication. In this study, a monoenergetic beam of electrons is continuously injected into an initial step-like density profile. To be applicable to shock ignition, and the time of the ignitor pulse, 30 keV and 100 keV (arguments for this choice are discussed in Chapter 4) monoenergetic electron beams are injected into a step-like target at 10 g/cm$^3$ and 1 eV. To perform this study, the

CHIC radiation-hydrodynamic code [45] is used in conjunction with the $M1$ kinetic treatment of the fast electrons [46, 47] to produce a hybrid model. This will be elaborated upon in Chapter 3 where the hybrid model developed as part of this thesis is discussed.

The study concludes that it is indeed possible to drive strong shocks with a pressure amplitude of several hundred Mbar or more with a driver-shock efficiency of about 10% using monoenergetic 30 keV and 100 keV electron populations in step-like targets. However, as an initial study, it naturally makes a number of simplifying assumptions so that the key processes can be studied. Most notable are the assumptions of a monoenergetic electron population and a step-like target. As will be discussed in Chapter 4, there is particle-in-cell modelling and experimental evidence that the electron population will have an approximately Maxwellian distribution. Furthermore, it is reasonable to assume that the target will not be step-like at the time of the ignitor pulse because, by this time, the fuel will have been subjected to laser irradiation of several nanoseconds. In this thesis, the realism of the initial numerical study is improved by relaxing these assumptions and the consequences for fast electron driven shock wave formation in shock ignition are assessed.

At this stage, it is noted that subsequent to the work presented in Chapter 5 being published in Fox et al. [12], a very similar study was published in Nicolai et al. [41]. The results of this later study agree strongly with our own. Both assess the effect of extended electron energy distributions on shock wave formation and conclude that strong shock waves of interest to shock ignition can be generated. However, both also note that the time taken for the shock wave to develop can become significant in the context of shock ignition and that this needs careful consideration when assessing its usefulness.

## 2.7 Summary

A brief primer on some of the wide range of areas of physics that are applicable to this thesis has been given. Only the most salient results from these respective areas has been presented and this represents just a small fraction of the vast literature available on each topic. It is hoped that sufficient detail has been given to orientate the reader so that the following chapters on the development of a hybrid model and its application to the problem of fast electron driven shock wave generation in dense plasmas may be considered in context.

# Chapter 3

# Numerical Solution of the Model

## 3.1 Introduction

A 1D planar hybrid model has been developed to model the generation of fast electron driven shocks waves in dense plasmas. It combines a kinetic description of fast electron transport with a single-fluid, two-temperature hydrodynamic background plasma. This combination retains the kinetic treatment of electron transport required to reliably model energy deposition by a fast electron population, which is lost in a fully hydrodynamic model, and gives a reasonable account of the response of the target plasma without the difficulty and computational expense of a fully kinetic treatment.

The kinetic model solves the relativistic Vlasov-Fokker-Planck equation [19]. It is based on the KALOS method [48, 49] which parameterises momentum space in terms of a spherical geometry and expands the momentum dependence of the distribution function as a series of spherical harmonics. Although the general approach taken is the same, the details of the differencing schemes used in the hybrid model are not necessarily the same as used in KALOS.

The hydrodynamic model is a reduced and modified version of the 3D single-fluid magnetohydrodynamics model presented in Ref. 50. After reducing this model to 1D and excluding the magnetic field, the resulting hydrodynamic equations are solved following the prescription given in Ref. 50, assuming an ideal gas equation of state. It is then extended to include separate electron and ion temperatures, electron-ion thermal equilibration and electron thermal conduction.

This chapter gives a detailed account of the differencing schemes and algorithms used to solve the kinetic and hydrodynamic descriptions and how the two are coupled through energy transfer mechanisms. This is followed by a representative selection of tests used to validate the model. First, the motivation behind the choice of model and its limitations are discussed.

## 3.2 Physical Motivation for the Model

The body of work presented in this thesis is motivated by an initial numerical study of fast electron drive shock wave generation in the context of shock ignition (see Section 2.6) [43]. As such the simulations presented herein exist in the same regimes as those in that study. This means having a dense, relatively cold collisional target plasma with spatial and temporal scales that are small compared to those of an injected relativistic electron population that is, at least initially, fairly collisionless. The dynamic range required to treat both of these populations with the same description is unfeasible so a hybrid approach is taken, as was done in Ref. 43.

The background plasma can be treated as a fluid because it is highly collisional in the regime of interest. In a typical simulation the background plasma will have a density on the order of 10 g/cm$^3$ and maximum temperature of a few hundred eV. With an atomic number of $Z = 1$ and a Coulomb logarithm of $\ln \Lambda = 2$, the electron-ion collision time is a small fraction of a femtosecond. This is much shorter than the typical hydrodynamic temporal scale. This means that locally the plasma can be described by average quantities i.e. the hydrodynamic variables. By choosing a fluid description, one is also committed to prescribing additional models for the plasma such as for resistivity and thermal conduction. The limitations of the model will be further discussed in Section 3.3.

The fast electrons should be treated kinetically because their long mean free paths mean that non-local effects will be important. As this thesis is concerned with the generation of shock waves using fast electron populations, it is important to create realistic deposition profiles. The particle-in cell approach [51] is a staple of kinetic modelling because it is relatively simple to implement, robust and has good conservation properties. However, it must be excluded from consideration because it suffers from noise and is unlikely to produce the smooth profiles that are desired. It is not immediately obvious how important the noise would be in the regime of dense plasmas considered in shock ignition. In its stead, a Vlasov-Fokker-Planck approach is taken for the kinetic modelling because, as a continuum model, it avoids the problem of granularity and will produce smooth, noise free deposition profiles. Examples of models using this finite difference technique are described in Refs. 48, 49 and 52–54.

All computational methods require some degree of data reduction and this hybrid model is no different. To this end, momentum space is represented as a truncated series expansion in spherical harmonics. This formulation has a clear interpretation of the arguments for closure - collisions act to reduce anisotropy in the distribution function and so provide a natural truncation of the series expansion. The kinetic module $M1$ [46, 47] in the code CHIC [45] is used to model fast electron transport in Refs. 43 and 41. This model uses a reduced moment based approach with closure provided by an assumed form for the third moment. This method is formally correct for a quasi-isotropic regime and so provides a good treatment in the collisional regimes of interest.

Overall, the hybrid approach is favoured from a development point of view because it is computationally robust and relatively easy to write and maintain. Also, additional physics can be included easily. From the point of view of use, they allow large time steps to be used compared to fully kinetic models so results can be obtained more efficiently. A few examples of hybrid codes of varying complexity include the unnamed code of Davies [55], PETRA [56], LEDA [53] and ZEPHYROS [57, 58].

## 3.3 Limitations of the Model

Shock ignition relies on the symmetric convergence of shock waves in spherical targets. With a 1D planar geometry, the hybrid model precludes the effect of spherical convergence as well as effects that may prevent symmetric propagation of shock waves. When using fast electrons to drive shock waves, the symmetry of shock wave propagation is determined by the degree of symmetry in the target and the deposition profile. Target symmetry is determined by the assembly phase of shock ignition which is outside the scope of this thesis. Symmetry in the deposition profile will be affected by non-uniformities in the fast electron population resulting from processes such as self-generated magnetic fields and beam filamentation. Their effects on the transverse deposition profile may be mitigated by beam divergence. The degree to which non-uniformities in the fast electron population affect the symmetry of the deposition profile should be assessed in the future.

The scope of the physics included in the model is limited when compared to the CHIC code. For example, CHIC includes detailed radiation transport with tabulated ionisation and opacity data, non-local thermal transport in the hydrodynamic module and a more complete coupling between the kinetic and hydrodynamic modules by additionally taking into account electron collisions with bound electrons and plasmons. However, there is strong agreement between the results presented in Chapter 5 and published in Ref. 12 that used the present hybrid model, and those published by other authors in earlier [43] and later [41] papers that used the hybrid form of the CHIC code. This gives confidence that the present hybrid model does capture the dominant physics in the regime of interest and its relative simplicity draws attention to these key processes.

Despite the limitations described above, a 1D planar model is sufficient to begin to address the possibility of fast electron driven shock wave generation in the context of shock ignition. Its relative simplicity allows us to assess the viability of this process at a fundamental level, before introducing additional complexity.

## 3.4 Kinetic Description

The fast electron population is described using the relativistic Vlasov-Fokker-Planck model. The Vlasov-Fokker-Planck equation for the case of a single electron species and single ion species is given in its general form:

$$\frac{\partial f}{\partial t} + \mathbf{v}.\frac{\partial f}{\partial \mathbf{r}} - e\left(\mathbf{E} + \mathbf{v} \times \mathbf{B}\right).\frac{\partial f}{\partial \mathbf{p}} = C_{ee}(f) + C_{ei}(f). \tag{3.1}$$

Here, $f$ is the fast electron distribution function. The electric, **E** and magnetic, **B** fields are macroscopic fields arising due to large scale collective phenomena. The terms $C_{ee}$ and $C_{ei}$ are the Fokker-Planck electron-electron and electron-ion collision terms, respectively.

The solution of Eq. 3.1 in full six-dimensional coordinate space is extremely challenging so the model is reduced to one spatial dimension and the electron distribution function is represented by a truncated series expansion. For convenience, a set of orthogonal expansion functions is desired. Furthermore, collisional processes act to isotropise the distribution function and the approximately elastic scattering of electrons off the much heavier ions changes the angle of the momentum vector but not its magnitude. These points lead to a spherical harmonic series as a natural expansion of the distribution function. In 1D, with momentum space parameterised in terms of a spherical geometry, i.e. ($|\mathbf{p}|$ , $\theta$, $\phi$), the distribution function expansion is written as,

$$f(x, \mathbf{p}, t) = \sum_{l=0}^{l_{\max}} \sum_{m=-l}^{l} f_l^m(x, p, t) P_l^{|m|}(\cos\theta) \mathrm{e}^{\mathrm{i}m\phi}, \tag{3.2}$$

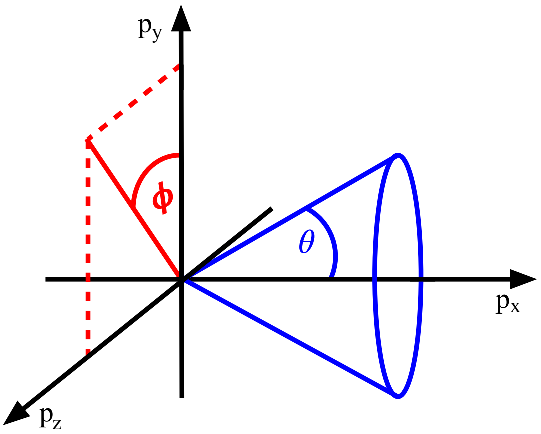

**Figure 3.1: Orientation of the spherical coordinate system used in momentum space relative to the cartesian momentum axes $p_x$, $p_y$ and $p_z$. The distribution function is taken to be axisymmetric about the $p_x$ axis, making it the polar axis.**

where $f_l^{-m} = (f_l^m)^*$ and $P_l^m(\cos\theta)$ are the associated Legendre polynomials. Figure 3.1 shows the orientation of the spherical coordinate system used in momentum space relative to the cartesian momentum axes $p_x$, $p_y$ and $p_z$. The cartesian momentum axis, $p_x$ is the polar axis so that the spherical momentum unit vectors are related to the cartesian momentum unit vectors by,

$$\hat{\boldsymbol{r}} = \cos\theta\hat{\boldsymbol{p}}_{\boldsymbol{x}} + \sin\theta\cos\phi\hat{\boldsymbol{p}}_{\boldsymbol{y}} + \sin\theta\sin\phi\hat{\boldsymbol{p}}_{\boldsymbol{z}} \tag{3.3}$$

$$\hat{\boldsymbol{\theta}} = -\sin\theta\hat{\boldsymbol{p}}_{\boldsymbol{x}} + \cos\theta\cos\phi\hat{\boldsymbol{p}}_{\boldsymbol{y}} + \cos\theta\sin\phi\hat{\boldsymbol{p}}_{\boldsymbol{z}} \tag{3.4}$$

$$\hat{\boldsymbol{\phi}} = -\sin\phi\hat{\boldsymbol{p}}_{\boldsymbol{y}} + \cos\phi\hat{\boldsymbol{p}}_{\boldsymbol{z}} \tag{3.5}$$

As will be seen, substituting Eq. 3.2 into Eq. 3.1 will yield a set of equations for the coefficients $f_l^m(x,p,t)$, while the angular dependence can effectively be ignored during the numerical calculation. This significantly reduces the computational expense while still offering the desired resolution in the magnitude of momentum. Resolution in $(\theta,\phi)$ is somewhat compromised because it is not possible to expand the series *ad infinitum*. However, calculations require less resolution in $(\theta,\phi)$ when collisions are strong as they isotropise the distribution function. It will also be seen that by adopting a spherical harmonic expansion, the collision process of angular scattering by ions is reduced to a simple exponential decay of the amplitude of each harmonic at a rate proportional to $l(l+1)/2$. This provides a natural truncation to the series expansion. It should be noted that a truncated spherical harmonic expansion does not necessarily preserve positivity so care must be taken to ensure physically meaningful results are obtained. Care must also be taken where $p = 0$ to avoid over-resolving $p$ compared to $\theta$ and $\phi$. As will be explained, this is done by truncating the series expansion in the first few momentum grid cells and expanding $f_l^m$ as a power series in small $p$ close to $p = 0$ [54].

Equation 3.1 is solved by adopting the widely used method of operator splitting. This assumes that the terms in Eq. 3.1 are only weakly coupled over the period of a time step so that they can be solved independently and sequentially using finite difference schemes tailored to their individual properties. After each term is solved for a single finite difference time step, the distribution function has been evolved from time $n$ to time $n+1$.

After expanding the distribution function and applying operator splitting, Eq. 3.1 can be written in a somewhat abstract form:

$$\frac{\partial f_l^m}{\partial t} = \mathcal{A}_{l,x}^m + \mathcal{E}_{l,x}^m + \mathcal{E}_{l,y}^m + B_{l,z}^m + C_{l,ei}^m + C_{l,ee}^m, \tag{3.6}$$

where $\mathcal{A}_{l,x}^m$ represents the equation for spatial advection in the $x$-direction, $\mathcal{E}_{l,x,y}^m$ are for acceleration due to electric fields in the $x$- and $y$-directions, $B_{l_z}^m$ is for acceleration by a magnetic field in the $z$-direction and finally $C_{l,ei}^m$ and $C_{l,ee}^m$ are the electron-ion and electron-electron collision terms, respectively.

This section continues with a discussion of how to calculate physical quantities such as number density and current density from the fast electron distribution function now that it has been expanded as a series of spherical harmonics. This is followed by an extended discussion of the kinetic computational domain discretization and of the numerical schemes used to solve the equations represented in Eq. 3.6.

### 3.4.1 Moments of a Distribution Function

The concept of moments of the distribution function as measures of average quantities has been discussed previously. It is revisited here to derive the most useful moments in the context of the spherical harmonic expansion. In general, the $k^{\text{th}}$ moment, $\mathbf{\Pi}_k$, of the distribution function $f(x, \mathbf{p}, t)$ is written:

$$\mathbf{\Pi}_k = \int \mathbf{v}\mathbf{v} \cdots \mathbf{v} f \, \mathrm{d}^3\mathbf{p}, \tag{3.7}$$

with $k$ factors of $\mathbf{v}$, and $\mathbf{\Pi}_k$ is a tensor of rank $k$. Expanding the distribution function into spherical harmonics gives,

$$\mathbf{\Pi}_k = \sum_{l=0}^{l_{max}} \sum_{m=-l}^{l} \int_0^\infty \int_0^{2\pi} \int_0^\pi \mathbf{v}\mathbf{v} \cdots \mathbf{v} f_l^m P_l^{|m|}(\cos\theta) \mathrm{e}^{im\phi} p^2 \sin\theta \, \mathrm{d}\theta \, \mathrm{d}\phi \, \mathrm{d}p. \tag{3.8}$$

The lowest order moments have simple physical interpretations. The zeroth order moment gives the number density, $n$ as,

$$n = \sum_{l=0}^{l_{max}} \sum_{m=-l}^{l} \int_0^\infty \int_0^{2\pi} \int_0^\pi f_l^m P_l^{|m|}(\cos\theta) \mathrm{e}^{im\phi} p^2 \sin\theta \, \mathrm{d}\theta \, \mathrm{d}\phi \, \mathrm{d}p. \tag{3.9}$$

Let $\mu = \cos\theta$ so that $\mathrm{d}\mu = -\sin\theta \, \mathrm{d}\theta$, then,

$$n = \sum_{l=0}^{l_{max}} \sum_{m=-l}^{l} \int_0^\infty \int_0^{2\pi} \int_{-1}^1 f_l^m P_0^0(\mu) P_l^{|m|}(\mu) \mathrm{e}^{im\phi} p^2 \, \mathrm{d}\mu \, \mathrm{d}\phi \, \mathrm{d}p, \tag{3.10}$$

where $P_0^0(\mu) = 1$ has been inserted to help show that, due to the orthogonality of spherical harmonics, only the $l = 0, m = 0$ harmonic will make a non-zero contribution to the summation. The orthogonality of the associated Legendre polynomials can be expressed as,

$$\int_{-1}^1 P_l^m(x) P_{l'}^{m'}(x) \mathrm{d}x = \frac{(l+m)!}{(l-m)!} \frac{2}{2l+1} \delta_{ll'} \delta_{mm'}, \tag{3.11}$$

where $\delta_{ij}$ is the Kronecker delta function. Equation 3.10 then reduces to:

$$\begin{aligned} n &= 2\int_0^\infty \int_0^{2\pi} f_0^0 p^2 \,\mathrm{d}\phi\,\mathrm{d}p \\ &= 4\pi \int_0^\infty f_0^0 p^2 \,\mathrm{d}p. \end{aligned} \tag{3.12}$$

The zeroth order harmonic gives scalar quantities. The first order moment gives vector quantities and so determines the flux density, $\mathbf{\Phi}$ generally as,

$$\mathbf{\Phi} = \sum_{l=0}^{l_{max}} \sum_{m=-l}^{l} \int_0^\infty \int_0^{2\pi} \int_0^\pi \mathbf{v} f_l^m P_l^{|m|}(\cos\theta)\mathrm{e}^{im\phi} p^2 \sin\theta \,\mathrm{d}\theta\,\mathrm{d}\phi\,\mathrm{d}p. \tag{3.13}$$

The $x$-component of the flux density is therefore given by,

$$\Phi_x = \sum_{l=0}^{l_{max}} \sum_{m=-l}^{l} \int_0^\infty \int_0^{2\pi} \int_{-1}^{1} v\mu f_l^m P_l^{|m|}(\mu)\mathrm{e}^{im\phi} p^2 \,\mathrm{d}\mu\,\mathrm{d}\phi\,\mathrm{d}p. \tag{3.14}$$

Now, $P_1^0(\mu) = \mu$ so,

$$\Phi_x = \frac{4\pi}{3} \int_0^\infty f_1^0 p^2 \frac{pc}{\sqrt{p^2 + m_e^2 c^2}} \,\mathrm{d}p. \tag{3.15}$$

Equations 3.16 to 3.19 represent a collection of useful moments that can be derived following the same arguments demonstrated above:

$$n = 4\pi \int_0^\infty f_0^0 p^2 \,\mathrm{d}p \qquad \text{Number density,} \tag{3.16}$$

$$u = 4\pi \int_0^\infty f_0^0 p^2 \left(\sqrt{p^2c^2 + m_e^2c^4} - m_e c^2\right) \mathrm{d}p \qquad \text{Energy density,} \tag{3.17}$$

$$j_x = -\frac{4\pi e}{3} \int_0^\infty f_1^0 p^2 \frac{pc}{\sqrt{p^2 + m_e^2 c^2}} \,\mathrm{d}p \qquad \text{Current density in x-direction,} \tag{3.18}$$

and

$$j_y = -\frac{8\pi e}{3} \int_0^\infty f_1^1 p^2 \frac{pc}{\sqrt{p^2 + m_e^2 c^2}} \,\mathrm{d}p \qquad \text{Current density in y-direction} \tag{3.19}$$

### 3.4.2 Discretization

The computational domain is divided up into $nx \times np$ cells with $nx$ spatial cells and $np$ momentum cells, each of a fixed width $\Delta x$ and $\Delta p$, respectively. The $x$-coordinate of the cell centres are denoted $x_j$ for $j = 1, \ldots, nx$ and lie half-way between the adjacent cell boundaries defined at $x_{j+1/2}$. The boundaries of the domain lie at $x_{1/2}$ and $x_{nx+1/2}$. This indexing scheme is cell centred and requires that ghost cells external to the domain be included at $x_0$ and $x_{nx+1}$ to implement boundary conditions. The momentum grid is similarly defined.

To avoid excessive resolution as $p \to 0$, harmonics of index $l$ are not represented in momentum cells of index $k < l$. This does not cause a problem as low momentum electrons are highly collisional and nearly isotropic.

### 3.4.3 Advection

In 1D, spatial advection is given by,

$$\frac{\partial f}{\partial t} + v_x \frac{\partial f}{\partial x} = 0. \tag{3.20}$$

Substituting in Eq. 3.2, noting that $v_x = v \cos\theta$ and using the recurrence relation for the associated Legendre polynomials $(2l+1)\cos\theta P_l^m = (l-m+1)P_{l+1}^m + (l+m)P_l^m$ yields,

$$\mathcal{A}_{l,x}^m = -\left(\frac{l-m}{2l-1}\right) v \frac{\partial f_{l-1}^m}{\partial x} - \left(\frac{l+m+1}{2l+3}\right) v \frac{\partial f_{l+1}^m}{\partial x}. \tag{3.21}$$

This set of equations can be easily cast in matrix form as $\frac{\partial \mathbf{Q}}{\partial t} + \mathbf{A}\frac{\partial \mathbf{Q}}{\partial x} = 0$ where $\mathbf{Q} = \{f_l\}$ and $\mathbf{A}$ is the $(l_{max}+1) \times (l_{max}+1)$ matrix of constant coefficients defined by Eq. 3.21 [49, 59]. Assuming $\mathbf{A}$ has only real and distinct eigenvalues it can be shown that,

$$\frac{\partial \mathbf{W}}{\partial t} + \mathbf{\Lambda}\frac{\partial \mathbf{W}}{\partial x} = 0, \tag{3.22}$$

where $\mathbf{\Lambda}$ is the matrix of eigenvalues of $\mathbf{A}$, and $\mathbf{W} = \mathbf{K}^{-1}\mathbf{Q}$, where $\mathbf{K}$ is the matrix of eigenvectors of $\mathbf{A}$. Equation 3.21 has now been reduced to a set of uncoupled constant coefficient advection equations which can be solved using standard, well developed methods. The Piecewise Parabolic Method (PPM) [60] is used with reflective and/or open boundary conditions. The boundary conditions are imposed before decomposing the spherical harmonics into the eigenfunctions. Reflective boundaries require $f^m_{l,1-j} = (-1)^{l-m} f^m_{l,j}$ for $j < 1$ and $f^m_{l,2nx+1-j} = (-1)^{l-m} f^m_{l,j}$ for $j > nx$. Open boundary conditions require $f^m_{l,j} = 0$ for $j < 1$ and $j > nx$. The advection solver is subject to a Courant-Friedrich-Lévy (CFL) stability condition, i.e. $\max\{\lambda_i\}\Delta t < \min\{\Delta x_j\}$, where $\lambda_i$ is one of the eigenvalues in $\Lambda$. The domain is uniform in $x$ and since, for a finite number of spherical harmonics, $\lambda_i < v$, it is sufficient to impose that $\max\{v\}\Delta t < \Delta x$. Once the advection solver has evolved $\mathbf{W}^n$ to $\mathbf{W}^{n+1}$, the updated set of harmonics can be retrieved from $\mathbf{Q}^{n+1} = \mathbf{K}\mathbf{W}^{n+1}$.

### 3.4.4 Electric Field

Momentum space is parameterised in terms of a spherical geometry i.e. ($p$, $\theta$, $\phi$) with the distribution function taken to be axisymmetric about the $p_x$ axis, making it the polar axis in this case. In this geometry the electric fields in the $x$- and $y$-directions are, respectively,

$$E_x\hat{\mathbf{x}} = E_x \cos\theta\hat{\mathbf{r}} - E_x \sin\theta\hat{\boldsymbol{\theta}}, \tag{3.23}$$

and

$$E_y\hat{\mathbf{y}} = E_y \sin\theta\cos\phi\hat{\mathbf{r}} + E_y \cos\theta\cos\phi\hat{\boldsymbol{\theta}} - E_y \sin\phi\hat{\boldsymbol{\phi}}. \tag{3.24}$$

Then, momentum advection due to electric fields in the $x$- and $y$-directions is given by,

$$\frac{\partial f}{\partial t} - eE_x\cos\theta\frac{\partial f}{\partial p} - eE_x\frac{\sin^2\theta}{p}\frac{\partial f}{\partial\cos\theta} = 0, \tag{3.25}$$

and

$$\frac{\partial f}{\partial t} - eE_y \sin\theta\cos\phi\frac{\partial f}{\partial p} + eE_y\frac{\cos\theta\cos\phi\sin\theta}{p}\frac{\partial f}{\partial\cos\theta} + eE_y\frac{\sin\phi}{p\sin\theta}\frac{\partial f}{\partial\phi} = 0. \tag{3.26}$$

Upon substitution of Eq. 3.2 and appropriate associated Legendre polynomial recurrence relations, momentum advection due to $E_x$ for all $m$ ($m \geq 0$) is described by,

$$\mathcal{E}^m_{l,x} = eE_x\left[\frac{l-m}{2l-1}G^m_{l-1} + \frac{l+m+1}{2l+3}H^m_{l+1}\right]. \tag{3.27}$$

The two differential functions $G^m_l$ and $H^m_l$ are defined:

$$G^m_l(p) = p^l\frac{\partial(p^{-l}f^m_l)}{\partial p}; \quad H^m_l(p) = \frac{1}{p^{n+1}}\frac{\partial(p^{l+1}f^m_l)}{\partial p}. \tag{3.28}$$

For $m > 0$, momentum advection due to $E_y$ is given by,

$$\begin{aligned}\mathcal{E}^{m>0}_{l,y} &= \frac{1}{2}\frac{eE_y}{2l-1}\left[G^{m-1}_{l-1} - (l-m)(l-m-1)G^{m+1}_{l-1}\right] \\ &- \frac{1}{2}\frac{eE_y}{2l+3}\left[H^{m-1}_{l+1} - (l+m+1)(l+m+2)H^{m+1}_{l+1}\right],\end{aligned} \tag{3.29}$$

and for $m = 0$,

$$\mathcal{E}^0_{l,y} = -eE_y\left[\frac{l(l-1)}{2l-1}G^1_{l-1} - \frac{(l+1)(l+2)}{2l+3}H^1_{l+1}\right]. \tag{3.30}$$

Each of Eqs. 3.27, 3.29 and 3.30 is a set of first-order, coupled PDEs. The PDEs are linear (in that $E_{x,y}(x)$ is a constant in the momentum advection solve) but inhomogenous. This means that the method used in spatial advection cannot be applied and further operator splitting into derivative and '$f/p$' terms would not be conservative. A second order Runge-Kutta scheme [61] has been found to give the desired accuracy and robustness. Having a set of coupled PDEs means that each step of the Runge-Kutta must be carried out for all harmonics before the next step can be carried out. Additionally, the set of dependent variables ($\{f^m_l\}$) is a set of functions of $p$ and the RHS terms contain derivatives with respect to $p$. These should be centre-differenced in momentum to account for electrons accelerating and decelerating during the time, $\Delta t$.

The following is a description of the method used to solve Eq. 3.27. Equations 3.29 and 3.30 are differenced using the same principles. The differential functions defined by Eq. 3.28 are expanded when evolving harmonics with $l > 0$ and the following differencing scheme is used:

- The first step calculates $\{f_l^m(p_{k+1/2}, t + \Delta t/2)\}$, using an explicit first-order Euler integration step:

$$\begin{aligned} f_l^m(p_{k+1/2}, t + \Delta t/2) = & \frac{1}{2}\left(f_l^m(p_k, t) + f_l^m(p_{k+1}, t)\right) \\ & + \frac{\Delta t}{2} eE_x \left(\frac{l-m}{2l-1}\right)\left[\frac{f_{l-1}^m(p_{k+1}, t) - f_{l-1}^m(p_k, t)}{p_{k+1} - p_k}\right] \\ & - \frac{\Delta t}{2} eE_x \left(\frac{l-m}{2l-1}\right)(l-1)\left[\frac{f_{l-1}^m(p_{k+1}, t) + f_{l-1}^m(p_k, t)}{2p_{k+1/2}}\right] \\ & + \frac{\Delta t}{2} eE_x \left(\frac{l+m+1}{2l+3}\right)\left[\frac{f_{l+1}^m(p_{k+1}, t) - f_{l+1}^m(p_k, t)}{p_{k+1} - p_k}\right] \\ & - \frac{\Delta t}{2} eE_x \left(\frac{l+m+1}{2l+3}\right)(l+2)\left[\frac{f_{l+1}^m(p_{k+1}, t) + f_{l+1}^m(p_k, t)}{2p_{k+1/2}}\right]. \end{aligned} \tag{3.31}$$

- The upper momentum boundary assumes $\partial f/\partial p \to 0$ as $p \to \infty$. The lower momentum boundary condition requires that the isotropic part of the distribution has an extremum at $p = 0$ and that $f_{l\geq 1}^m(p \to 0) \sim p^l$. Assuming that $f_0^0(p_{3/2})$ and $f_0^0(p_{5/2})$ lie on the parabola $f_0^0(p) = f_0^0(0) + \alpha_{00}p^2$:

$$f_0^0(p) = f_0^0(0) + [f_0^0(p_{5/2}) - f_0^0(0)]\left(\frac{p}{p_{5/2}}\right)^2, \tag{3.32}$$

and

$$f_0^0(0) = \frac{f_0^0(p_{3/2}) - f_0^0(p_{5/2})p_{3/2}^2/p_{5/2}^2}{1 - p_{3/2}^2/p_{5/2}^2}. \tag{3.33}$$

Thus, the value of $f_0^0(0, t + \Delta t/2)$ is calculated using $f_0^0(p_{3/2}, t + \Delta t/2)$ and

$f_0^0(p_{5/2}, t\ +\ \Delta\ t/2)$. For $l \geq 1$,

$$f_{l\geq 1}^m(p) = f_l^m(p_2)\left(\frac{p}{p_2}\right)^l . \tag{3.34}$$

· The corrector step evaluates $\{f_l^m(p_k, t + \Delta t)\}$:

$$\begin{aligned}
f_l^m(p_k, t+\Delta t) = f_l^m(p_k, t)& \\
&+ \Delta t e E_x\left(\frac{l-m}{2l-1}\right)\times \\
&\left[\frac{f_{l-1}^m(p_{k+1/2}, t+\Delta t/2) - f_{l-1}^m(p_{k-1/2}, t+\Delta t/2)}{p_{k+1/2} - p_{k-1/2}}\right] \\
&- \Delta t e E_x\left(\frac{l-m}{2l-1}\right)(l-1)\times \\
&\left[\frac{f_{l-1}^m(p_{k+1/2}, t+\Delta t/2) + f_{l-1}^m(p_{k-1/2}, t+\Delta t/2)}{2p_k}\right] \\
&+ \Delta t e E_x\left(\frac{l+m+1}{2l+3}\right)\times \\
&\left[\frac{f_{l+1}^m(p_{k+1/2}, t+\Delta t/2) - f_{l+1}^m(p_{k-1/2}, t+\Delta t/2)}{p_{k+1/2} - p_{k-1/2}}\right] \\
&- \Delta t e E_x\left(\frac{l+m+1}{2l+3}\right)(l+2)\times \\
&\left[\frac{f_{l+1}^m(p_{k+1/2}, t+\Delta t/2) + f_{l+1}^m(p_{k-1/2}, t+\Delta t/2)}{2p_k}\right].
\end{aligned} \tag{3.35}$$

Care must be taken to use a conservative finite differencing scheme when evolving the $l = 0$ harmonic from time $t$ to $t + \Delta t$. In this case the differential operators defined in Eq. 3.28 are not expanded in the second step of the Runge-Kutta scheme and the following flux conservative differencing scheme is used instead:

$$\begin{aligned}
f_0^0(p_k, t+\Delta t) = f_0^0(p_k, t)& \\
&+ \Delta t\frac{eE_x}{3p_k^2}\left[\frac{p_{k+1/2}^2 f_1^0(p_{k+1/2}, t+\Delta t/2) - p_{k-1/2}^2 f_1^0(p_{k-1/2}, t+\Delta t/2)}{p_{k+1/2} - p_{k-1/2}}\right].
\end{aligned} \tag{3.36}$$

The CFL stability condition requires that the time step be limited such that $\max\{e|\mathbf{E}|\}\Delta t \leq \Delta p$. The electric field is calculated from a simplified Ohm's law. The details of this calculation are given in Section 3.6.1.

### 3.4.5 Magnetic Field

With the distribution function taken to be axisymmetric about the $p_x$ axis, rotation of the distribution in momentum space due to a magnetic field is given by,

$$\frac{\partial f}{\partial t} + eB_z \left[\cos\phi \frac{\partial f}{\partial \theta} - \sin\phi \cot\theta \frac{\partial f}{\partial \phi}\right] = 0. \tag{3.37}$$

Upon substitution of Eq. 3.2 and appropriate associated Legendre polynomial recurrence relations, this becomes, for $m > 0$,

$$\mathcal{B}_l^m = -\frac{1}{2}\frac{eB_z}{m_e}\left[(l-m)(l+m+1)f_l^{m+1} - f_l^{m-1}\right], \tag{3.38}$$

and, for $m = 0$,

$$\mathcal{B}_l^0 = -\frac{eB_z}{m_e} l(l+1) f_l^1. \tag{3.39}$$

The terms in this equation have the same index $l$ and couple the harmonics $f_l^{m-1}$, $f_l^m$ and $f_l^{m+1}$. This algebraic tri-diagonal matrix equation can be solved by standard methods using a trapezium scheme to integrate implicitly in time to second-order accuracy. The resulting finite difference stencils for Eqs. 3.38 and 3.39 are, respectively:

$$\begin{aligned} \frac{f_l^{m,n+1} - f_l^{m,n}}{\Delta t} = & -\frac{1}{4}\frac{eB_z}{m_e}\Big[(l-m)\,(l+m+1)\left(f_l^{m+1,n+1} + f_l^{m+1,n}\right) \\ & - \left(f_l^{m-1,n+1} + f_l^{m-1,n}\right)\Big], \end{aligned} \tag{3.40}$$

and

$$\frac{f_l^{0,n+1} - f_l^{0,n}}{\Delta t} = -\frac{1}{2}\frac{eB_z}{m_e} l\,(l+1)\left(f_l^{1,n+1} + f_l^{1,n}\right). \tag{3.41}$$

Notice that the isotropic part of the distribution $f_0^0$ is, of course, unaffected by rotation in momentum space so Eq. 3.41 naturally conserves mass and energy.

The magnetic field itself is updated from Maxwell's equation $\partial B_z/\partial t = -\partial E_y/\partial x$ in two steps. As will be presented in Section 3.6.1, $E_y = -\eta j_{f,y} + u_x B_z$, which upon substitution into Maxwell's equation yields,

$$\frac{\partial B_z}{\partial t} = \frac{\partial}{\partial x}(\eta j_{f,y}) - \frac{\partial}{\partial x}(u_x B_z). \tag{3.42}$$

The first term represents a source term and is solved using centred differencing. The second term represents advection of the magnetic field at the hydrodynamic velocity and thus has the same CFL stability condition as for the hydrodynamic description given by Eq. 3.65. This term is solved using upwind or downwind differencing, depending on the local fluid velocity. The fluid velocity is linearly interpolated to the boundaries of cells internal to the domain. Uniform, steady outflow conditions are assumed at both domain boundaries.

The differencing schemes used to update the magnetic field are simple and stable but suffer from numerical diffusion. They have proven to be sufficient for the preliminary studies on the effect of an externally applied magnetic field on fast electron driven shock wave generation presented in Chapter 8 but should be improved in a future version of the hybrid model.

### 3.4.6 Electron-Ion Scattering

Electron-ion scattering is calculated under the assumption that the relativistic electrons are sufficiently fast compared to the background ions so that the ions can be considered to be at rest. In this regime, and when small angular scattering is dominant, the relativistic differential scattering cross-section is:

$$\sigma(p,\theta) = \frac{b_0^2}{4}\csc^4\left(\frac{\theta}{2}\right), \tag{3.43}$$

where $p$ is the momentum of the scattered fast electron, $\theta$ is the scattering angle and $b_0$ is the relativistic impact parameter for $\pi/2$ scattering given by,

$$b_0 = \left(\frac{ZZ_i e^2\left(m_e + m_i\right)}{4\pi\epsilon_0 m_e m_i p v}\right)^2, \tag{3.44}$$

where $v$ is the velocity of the scattered fast electron of mass $m_e$ and atomic number $Z$, and $m_i$ is the mass of the scattering ion with atomic number $Z_i$.

The probability of collisions $\psi$ with scattering angle $\theta$ occurring in time $\Delta t$ is proportional to $\Delta t f_i|\mathbf{p}|\sigma$, where $f_i$ is the distribution function of the scattering ions and is a function of the scattering ion momentum $\mathbf{p}_i$. Substituting this, and Eq. 2.18, into Eq. 2.17 eventually yields,

$$\mathcal{C}_{ei} = \frac{1}{2}\frac{Z^2 n_i e^4}{4\pi\epsilon_0^2}\frac{\ln\Lambda_s}{p^2 v}\frac{1}{\sin\theta}\frac{\partial}{\partial\theta}\left(\sin\theta\frac{\partial f}{\partial\theta}\right). \tag{3.45}$$

Finally, substituting Eq. 3.2 into Eq. 3.45 yields,

$$\mathcal{C}_{ei,l} = \frac{\partial f_l^m}{\partial t} = -\frac{l(l+1)}{2}\frac{Z^2 n_i e^4}{4\pi\epsilon_0^2}\frac{\ln\Lambda_s}{p^2 v}f_l^m. \tag{3.46}$$

Equation 3.46 does not involve any momentum or velocity derivatives and so can be solved analytically:

$$f_{l,k}^{m,n+1} = f_{l,k}^{m,n}\exp\left(-\frac{l(l+1)}{2}\frac{Z^2 n_i e^4}{4\pi\epsilon_0^2}\frac{\ln\Lambda_{s,k}}{p_k^2 v_k}\Delta t\right). \tag{3.47}$$

Equation 3.47 represents an exponential decay of each harmonic independently and at a rate proportional to $l(l+1)/2$. This provides a natural termination to the expansion as higher harmonics are damped more rapidly. Note that the $l = 0$ harmonic is unaffected by electron-ion scattering so mass and energy are naturally conserved.

The electron-ion scattering Coulomb logarithm $\ln\Lambda_s$ is obtained from an approximate model for binary scattering from atoms, including quantum effects [62]:

$$\ln \Lambda_s = \ln \frac{4\epsilon_0 h^2}{Z^{1/3} m_e e^2 \lambda_{dB}}, \tag{3.48}$$

where $h$ is Planck's constant and $\lambda_{dB}$ is the de Broglie wavelength of the fast electron. For 20 keV and 100 keV electrons $\ln \Lambda_s \simeq$ 4.3 and 5.2, respectively.

### 3.4.7 Electron-Electron Drag

Electron-electron collisions are calculated under the assumption that interactions between fast electrons themselves are negligible compared to the interactions between fast electrons and the background electrons. Thus, Eq. 2.17 is reduced to a single term representing drag on fast electrons due to background electrons:

$$\mathcal{C}_{ee} = -\frac{\partial}{\partial \mathbf{p}} \cdot \left( \frac{\langle \mathbf{\Delta p} \rangle}{\Delta t} f \right). \tag{3.49}$$

The effect of drag is to reduce the magnitude of momentum but not its direction so, in a spherical geometry, Eq. 3.49 becomes,

$$\mathcal{C}_{ee} = -\frac{1}{p^2} \frac{\partial}{\partial p} \left( p^2 f \frac{\mathrm{d}p}{\mathrm{d}t} \right). \tag{3.50}$$

The standard expression for the drag on a fast electron in all matter is,

$$\frac{\mathrm{d}p}{\mathrm{d}t} = -\frac{n_e e^4 \ln \Lambda_d}{4\pi \epsilon_0^2 m_e v^2}. \tag{3.51}$$

It is then straightforward to substitute into Eq. 3.50 to obtain,

$$\mathcal{C}_{ee} = \frac{n_e e^4}{4\pi \epsilon_0^2 m_e} \frac{1}{p^2} \frac{\partial}{\partial p} \left[ \ln \Lambda_d f \left( \frac{m^2 c^2 + p^2}{c^2} \right) \right], \tag{3.52}$$

where the relation $v = pc/\sqrt{m^2c^2 + p^2}$ has been used. Equation 3.52 is solved implicitly, but treating the background electron number density $n_e$ and Coulomb logarithm $\ln \Lambda_d$ as time-lagged coefficients. A simple upwind finite difference stencil is used:

$$\frac{f_{l,k}^{m,n+1} - f_{l,k}^{m,n}}{\Delta t} = \frac{n_e^n e^4}{4\pi\epsilon_0^2 m_e c^2}\frac{1}{p_k^2}\left[\frac{\ln\Lambda_{l,k+1}^n f_{l,k+1}^{m,n+1}(m_e^2c^2+p_{k+1}^2) - \ln\Lambda_{l,k}^n f_{l,k}^{m,n+1}(m_e^2c^2+p_k^2)}{p_{k+1}-p_k}\right]. \tag{3.53}$$

The Coulomb logarithm $\ln\Lambda_d$ in Eq. 3.52 is given for a nonionised medium in Ref. 63:

$$\ln\Lambda_d = \frac{1}{2}\left\{\ln\left[\left(\frac{K}{I}\right)^2\frac{\gamma+1}{2}\right] + \frac{1}{\gamma^2} + \frac{1}{8}\left(\frac{\gamma-1}{\gamma}\right)^2 - \left(\frac{2\gamma-1}{\gamma^2}\right)\ln 2 - \delta\right\}, \tag{3.54}$$

where $K$ is the kinetic energy of the fast electron, $\gamma = \sqrt{1-\beta^2}$ is the Lorentz factor with $\beta = v/c$, $I$ is the mean excitation energy of the medium atoms and $\delta$ is a density-effect correction which accounts for the reduction of the stopping power due to the polarisation of the medium. The derivation of Eq. 3.54 considers the atomic electrons to be free and takes into account relativity and spin effects as well as exchange effects resulting from the indistinguishability of the interacting electrons.

Solodov and Betti [64] considered the stopping of electrons in a plasma by combining binary scattering and plasma wave excitation to obtain,

$$\ln\Lambda_d = \frac{1}{2}\left\{\ln\left[\left(\frac{K}{\hbar\omega_{pe}}\right)^2\frac{\gamma+1}{2\gamma^2}\right] + 1 + \frac{1}{8}\left(\frac{\gamma-1}{\gamma}\right)^2 - \left(\frac{2\gamma-1}{\gamma^2}\right)\ln 2\right\}. \tag{3.55}$$

The main difference between Eq. 3.54 and Eq. 3.55 is that the mean excitation energy $I$ stands for the minimum energy transfer in the plasma $\hbar\omega_{pe}$. It can be shown that in the limit of $\beta \to 1$, $\delta \to \ln\left[(\hbar\omega_{pe})^2\gamma^2/I^2\right] - \beta^2$ and Eqs. 3.54 and 3.55 agree. This is because as $\beta \to 1$, Lorentz contraction means the fast electrons interact with the atomic electrons for a period of time that is less than the time taken for the atomic electron to oscillate around the nuclei, so the plasma model applies.

Equation 3.54 was evaluated by Davies [55] to yield,

$$\ln \Lambda_d = \ln \frac{K}{I} + \frac{1}{2} \ln (\gamma + 1) + \frac{0.909}{\gamma^2} - \frac{0.818}{\gamma} - 0.246, \tag{3.56}$$

which differs from Eq. 3.55 in that the limit $\beta \to 1$ is not invoked. Figure 3.2 compares Eqs. 3.56 and 3.55 for fast electron temperatures of 1 eV to 1 MeV. A lower limit of 2 has been imposed in both models in accordance with the findings of Lee and More [16]. The Lee-More model is discussed in more detail in Section 3.5.3. Equations 3.55 and 3.56 agree at lower energies but begin to diverge at highly relativistic energies and differ by $\sim$5% at 1 MeV. This body of work used relatively low temperature fast electron distributions with $T_f \sim$ few 10s of keV to 100 keV. In the latter case, the momentum grid extended to momenta equivalent to $\sim$2 MeV but, as the fast electron distribution is Maxwellian, just 5% of the electrons have energies above 450 keV so the divergence of the models is unimportant. Equation 3.56 is used with $I = \hbar\omega_{pe}$.

### 3.4.8 Fast Electron Injection

Fast electron injection is included by supplementing Eq. 3.6 with the following:

$$\frac{\partial f_l^m}{\partial t} = \mathcal{S}_l^m. \tag{3.57}$$

Here, $\mathcal{S}_l^m$ is a source term representing the change in the harmonics due to fast electron injection. The injected fast electron distribution is beamed along the $p_x$ axis with a $\cos^M \theta$ dependence for even values of $M$. Therefore, $\mathcal{S}_l^m$ is non-zero for even values of $l$ with $m = 0$, and zero otherwise.

The injected electron population can have either a relativistic Maxwellian or Gaussian energy distribution and can be beamed in the $x$-direction. A relativistic Maxwellian distribution is specified as:

$$f_{\mathrm{M}} \propto \left(\cos^M \theta\right) p^2 \exp\left(-\sqrt{p^2 + m_e^2 c^2}/eT_f\right), \tag{3.58}$$

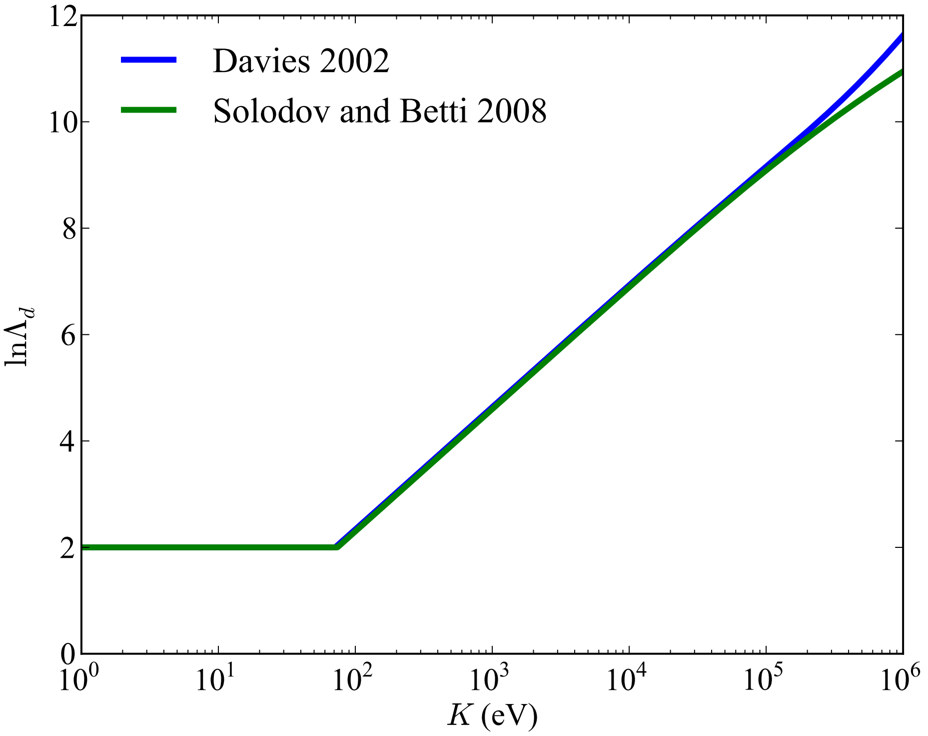

**Figure 3.2: A comparison of the Coulomb logarithms for electron-electron drag as calculated by Davies [55] and Solodov and Betti [64]. The two models agree well at lower fast electron energies but diverge at a few hundred keV with a difference of $\sim$5% at 1 MeV. This body of work used relatively low temperature fast electron distributions with $T_f$ $\sim$few 10s of keV to 100 keV. In the latter case, the momentum grid extended to momenta equivalent to $\sim$2 MeV but, as the fast electron distribution is Maxwellian, just 5% of the electrons have energies above 450 keV so the divergence of the models is unimportant.**

and a Gaussian distribution is specified as:

$$f_{\mathrm{G}} \propto \left(\cos^M \theta\right) p^2 \exp\left(-\left(E(p) - \bar{E}(p)\right)^2 / 2\sigma^2\right), \tag{3.59}$$

where $E(p) = \sqrt{p^2 + m_e^2 c^2} - m_e c^2$, $\bar{E}(p)$ is the mean energy of the Gaussian with a standard deviation of $\sigma = \mathrm{FWHM}/2\sqrt{2\ln 2}$. FWHM is the full-width at half-maximum. The constant of proportionality determines the energy or number density of electrons to be injected.

In either case, Maxwellian or Gaussian, the distribution is beamed into the target with a divergence half-angle $\theta_{\mathrm{h}} \approx 67^o/\sqrt{M}$, which is the result of looking for an approximate solution to $\cos^M \theta_{\mathrm{h}} = 1/2$. If $M$ is large then $\theta_{\mathrm{h}}$ is small. Then, as $\cos\theta_{\mathrm{h}} \approx 1 - \theta_{\mathrm{h}}^2/2$ and $\ln(1+x) \approx x$ one gets $M\theta_{\rm h}^2/2 = \ln 2$, so $\theta_{\rm h} \approx 67^o/\sqrt{M}$.

To inject the distribution $f$, it needs to be decomposed into its spherical harmonics. The $l = 0$, $m = 0$ harmonic is normalised so that $f_0^0 = a_0^0 f$ where the amplitude $a_0^0$ is calculated so that the correct energy or number density of electrons is injected. Higher order harmonics are defined as $f_l^m = a_l^m f$ with amplitudes, $a_l^m$ calculated and rescaled relative to $a_0^0$. Since the distribution is beamed in the direction of $p_x$, only $m = 0$ harmonics are non-zero and, by taking advantage of the orthogonality relation expressed in Eq. 3.11, the amplitudes of these harmonics are calculated as follows:

$$a_l = \left[\frac{\int_0^\pi f P_0 \sin\theta \, {\rm d}\theta}{\int_0^\pi P_0 P_0 \sin\theta \, {\rm d}\theta}\right]^{-1} \left[\frac{\int_0^\pi f P_l \sin\theta \, {\rm d}\theta}{\int_0^\pi P_l P_l \sin\theta \, {\rm d}\theta}\right]. \tag{3.60}$$

In this manner, a fast electron distribution with an arbitrary degree of beaming can be injected, assuming a sufficient number of harmonics are included.

When injecting a fast electron population with a Maxwellian energy distribution, a low energy portion of the distribution can be removed to approximate highly collisional electrons being deposited more readily and leaving only the more energetic part of the distribution. When this is done, care must be taken to avoid creating a ‘shock’ in momentum space and stimulating numerical instabilities. These are avoided by smoothly and exponentially increasing the distribution over the momentum range where the distribution is removed. The scale length of the exponential increase is chosen to be $1/100^{th}$ of the momentum range to be smoothed. This is short enough that the smoothed portion of the distribution is negligible compared to the rest of the distribution.

## 3.5 Fluid Description

The background plasma is modelled as a single fluid using a reduced form of the central-constrained transport scheme for ideal magnetohydrodynamics developed by Ziegler [50]. This MHD scheme is second-order in space and time and combines the semi-discrete central scheme for conservation laws developed by Kurganov et al. [65] and the constrained transport recipe described in Evans and Hawley [66]. The Ziegler scheme is reduced to 1D, neglecting magnetic fields to give an easy-to-code, robust and efficient numerical scheme for the single fluid equations which are solved in conservative form:

$$\frac{\partial \rho}{\partial t} + \frac{\partial}{\partial x}\left[\rho u\right] = 0, \tag{3.61}$$

$$\frac{\partial (\rho u)}{\partial t} + \frac{\partial}{\partial x}\left[\rho u^2 + P\right] = 0, \tag{3.62}$$

and

$$\frac{\partial e}{\partial t} + \frac{\partial}{\partial x}\left[(e + P)u\right] = 0. \tag{3.63}$$

Here, $\rho$ is the mass density, $e$ is the total energy density (internal plus kinetic) and $u$ is the fluid velocity in the $x$-direction. The thermal pressure $P$ is calculated assuming an ideal gas equation of state:

$$P = (\gamma - 1)\left(e - \frac{1}{2}\rho u^2\right), \tag{3.64}$$

where $\gamma$ is the ratio of specific heats. This assumption excludes the high-Z, low temperature region of parameter space.

The terms in the square brackets in Eqs. 3.61 through 3.62 are called flux functions and their values are known at the spatial centres. The Ziegler method requires that they be reconstructed at the spatial cell boundaries in order to calculate the numerical fluxes across the boundaries. The van Leer [67] slope limiter is used. This is the same slope limiter as is used in the PPM advection method. Equations 3.61 through 3.62 are then evolved in time using a second-order Runge-Kutta scheme [61] with the time step restricted by the usual hydrodynamic CFL stability condition:

$$\Delta t \leq \Delta x \max\{(u + c_s)\}, \tag{3.65}$$

where $c_s = \sqrt{\gamma P/\rho}$ is the local sound speed.

An average ion model is adopted so that different materials can be simulated. When the material has multiple species e.g. DT or CH$_n$, electron-ion scattering is performed on a species-by-species basis according to Eq. 3.47 with the electron number density and atomic numbers appropriately determined.

The Ziegler method is extended to be a two-temperature model with separate electron and ion temperatures. This allows for energy coupling between the fast and background electron populations through collisions and ohmic heating, and the inclusion of background electron thermal transport. A two-temperature model also necessitates the inclusion of electron-ion thermal equilibration. After describing the discretization of the hydrodynamic computational domain, the following sections detail how the two-temperature model is implemented with electron-ion thermal equilibration and how electron thermal conduction is included.

### 3.5.1 Discretization

The computational domain is divided up into $nx$ uniform spatial cells of width $\Delta x$ so that it coincides with the spatial grid used in the kinetic description. Thus, cell centres are denoted $x_j$ for $j = 1, \ldots, nx$ and lie half-way between the adjacent cell boundaries defined at $x_{j+1/2}$. The boundaries are defined at $x_{1/2}$ and $x_{nx+1/2}$. Two ghost cells are required on both sides of the domain. Periodic, reflective and outflow boundary conditions have been implemented. A typical simulation will use an outflow condition at $x_{1/2}$ and a reflective condition at $x_{nx+1/2}$. The outflow boundaries are zero-gradient conditions that allow shocks to leave the domain.

### 3.5.2 Two-Temperature Model

In the absence of electron-ion thermal equilibration and electron thermal conduction, the evolution of electron, $\tilde{e}_e$ and ion, $\tilde{e}_i$ internal energy densities is governed by,

$$\frac{\partial \tilde{e}_e}{\partial t} + \frac{\partial}{\partial x}\left(\tilde{e}_e u\right) + P_e \frac{\partial u}{\partial x} = 0 \tag{3.66}$$

and

$$\frac{\partial \tilde{e}_i}{\partial t} + \frac{\partial}{\partial x}\left(\tilde{e}_i u\right) + P_i \frac{\partial u}{\partial x} = 0. \tag{3.67}$$

By defining a new parameter, $r$ to be the fraction of total internal energy density associated with the electrons:

$$r = \frac{\tilde{e}_e}{\tilde{e}_e + \tilde{e}_i} = \frac{\tilde{e}_e}{\tilde{e}}, \tag{3.68}$$

and noting that $\tilde{e}_e = r\tilde{e}$ and $\tilde{e}_i = (1-r)\tilde{e}$, one can combine Eqs. 3.66, 3.67 and 3.68 to arrive at,

$$\frac{\partial r}{\partial t} + u\frac{\partial r}{\partial x} = 0. \tag{3.69}$$

This represents advection of the electron internal energy density fraction at the fluid velocity. Equation 3.69 is incorporated into the Ziegler scheme by taking cell centered values for $u$ and calculating the numerical flux of $r$ as defined in Ref. 50.

### 3.5.3 Electron-Ion Thermal Equilibration

The electron internal energy density fraction, $r$ needs to be updated due to thermal equilibration with the background ion species. The rate of energy transfer from electrons to ions through collisions is [68],

$$Q_e = 3\frac{m_e}{m_i}\frac{n_e e}{\tau_e}\left(T_i - T_e\right), \tag{3.70}$$

where $\tau_e$ is the basic electron-ion collision time [19]:

$$\tau_e = 6\pi\sqrt{2\pi}\frac{\epsilon_0^2 m_e^{1/2}\left(eT_e\right)^{3/2}}{Zn_e e^4 \ln\Lambda_{ei}}. \tag{3.71}$$

Here, $\ln\Lambda_{ei}$ is the Coulomb logarithm for collisions between background electrons and ions. This is calculated according to the Lee-More model in which,

$$\ln\Lambda_{ei} = \frac{1}{2}\ln\left(1 + \frac{b_{\text{max}}^2}{b_{\text{min}}^2}\right). \tag{3.72}$$

Here, $b_{\text{max}}$ and $b_{\text{min}}$ are the upper and lower cutoffs on the impact parameter for Coulomb scattering, respectively. The upper cutoff is set to be the Debye-Hückel screening length, $\lambda_{DH}$, and modified using a simple but accurate approximation to include a degeneracy correction:

$$\frac{1}{\lambda_{DH}^2} = \frac{n_e e^2}{\epsilon_0 e(T_e^2 + T_F^2)^{1/2}} + \frac{Z^2 n_i e^2}{\epsilon_0 e T_i}. \tag{3.73}$$

This model breaks down in dense plasmas where $\lambda_{DH}$ becomes less than the interatomic spacing. In this case $b_{\text{max}}$ is set equal to the interatomic spacing. The lower cutoff is taken as the maximum of the classical distance of closest approach and half of the de Broglie wavelength, each evaluated at the electron thermal velocity. In the degenerate limit the thermal velocity is calculated in terms of the Fermi energy. Lee and More prescribe that, for their model to give good agreement to numerical simulations of the Schrödinger equation, the Coulomb logarithm must have a value greater than or equal to 2.

Equation 3.70 is incorporated into the Runge-Kutta step of the Ziegler scheme as an extra term updating $r$:

$$\frac{\partial r}{\partial t} = \left(\frac{\partial r}{\partial t}\right)_{\text{Ziegler}} + \frac{Q_{ei}}{\tilde{e}}, \tag{3.74}$$

where the first term is given by Eq. 3.69. In the event that $Q_{ei}/\tilde{e}$ would overshoot the equilibrium condition given by $r_{\text{equi}} = Z/(1+Z)$, the Runge-Kutta step is forgone and $r$ is set equal to $r_{\text{equi}}$.

### 3.5.4 Electron Thermal Conduction

Flux limited, Spitzer-Härm electron thermal conductivity [15] is included according to the following prescription. In the absence of electric and magnetic fields, the electron thermal flux resulting from a temperature gradient is given by,

$$q_e = -\kappa \frac{\partial T_e}{\partial x}, \tag{3.75}$$

where $T_e$ is the electron temperature and $\kappa$ is the coefficient of thermal conductivity. The classical Spitzer-Härm coefficient of thermal conductivity is given by,

$$\kappa_c = \frac{3.2 n_e e^2 T_e \tau_e}{m_e}, \tag{3.76}$$

where $\tau_{ei}$ is the electron-ion collision time in Eq. 3.71.

The Spitzer-Härm conductivity is valid for gentle temperature gradients extending over many mean free paths. In laser produced plasmas it is common for this condition to be broken and have temperature gradients with scale lengths comparable to the mean free path. In this situation the classical theory will overestimate the heat flow and can even exceed the free-streaming limit, $q_e^{fs}$. The free-streaming limit is the theoretical heat flow carried by the electrons if they are allowed to stream freely down a temperature gradient at their thermal velocity:

$$q_e^{fs} = n_e e T_e v_{e,th}. \tag{3.77}$$

It is common practice to limit the classical conductivity to some fraction of the free-streaming limit. Extensive study using kinetic simulations [69–77] has shown that no single value is correct for all conditions. Typical values fall in the range 0.03 to 0.1 and, motivated by a study of a steadily ablating planar plasma [73], an approximate value of 0.05 is chosen. Therefore, the flux-limited free-streaming coefficient of thermal conductivity is defined:

$$\kappa_{fs} = 0.05\frac{n_e e T_e v_{e,th}}{\left|\frac{\partial T}{\partial x}\right|}. \tag{3.78}$$

The coefficient of thermal conductivity used in Eq. 3.75 is calculated by taking the harmonic mean of Eqs. 3.76 and 3.78:

$$\kappa^{-1} = \kappa_c^{-1} + \kappa_{fs}^{-1}. \tag{3.79}$$

Now, the rate of change of internal energy density due to thermal conduction is,

$$\frac{\partial \tilde{e}}{\partial t} = -\frac{\partial q_e}{\partial x}, \tag{3.80}$$

and therefore, assuming an ideal gas, the electron temperature evolves according to,

$$\frac{\partial T_e}{\partial t} = \frac{\gamma - 1}{n_e e}\frac{\partial}{\partial x}\left(\kappa\frac{\partial T}{\partial x}\right). \tag{3.81}$$

As this is a diffusion process, the time-step of an explicit differencing scheme will be proportional to $\Delta x^2$. To avoid unduly limiting the time-step, an implicit solution is chosen. It uses centre-differencing to produce a tri-diagonal matrix problem that can be solved efficiently using the Thomas algorithm [61]:

$$\frac{T_j^{n+1} - T_j^n}{\Delta t} = \frac{\gamma - 1}{n_{e,j}^n e}\frac{1}{\Delta x^2}\left[\kappa_{j+1/2}^n\left(T_{j+1}^{n+1} - T_j^{n+1}\right) - \kappa_{j-1/2}^n\left(T_j^{n+1} - T_{j-1}^{n+1}\right)\right]. \tag{3.82}$$

Notice that the electron number density and the coefficient of thermal conductivity are treated as lagged coefficients. This is reasonable because these variables are not expected to change greatly during one time-step which will, in general, be set by the advection of the fast electron population.

Open boundary conditions have been implemented to allow thermal energy to escape the domain, otherwise the co-location of fast electron injection and the hydrodynamic outflow condition can cause the background plasma to heat significantly and generate a thermal wave that eventually swamps the simulation. The crude assumption that the plasma outside the domain is cold i.e. $T_{e,0}^{n+1} = T_{e,nx+1}^{n+1} = 0$, has proved successful. Boundary conditions in which the temperature is constant across the boundary or linearly interpolated across the boundary were also tried and, irrespective of the choice, the same shock wave formation was observed.

Following the thermal conduction step, the electron internal energy density is updated according to the change in temperature and the ideal gas law. The electron internal energy density fraction is also updated accordingly.

## 3.6 Coupling of the Kinetic and Fluid Descriptions

The kinetic and hydrodynamic models are coupled through the generation of an electric field due to the resistive return current (discussed in Section 2.4) and through two energy transfer mechanisms. The model for the electric field will be discussed first, followed by the energy transfer mechanisms.

### 3.6.1 Ohm's Law

As described in Section 2.4, an Ohm's Law model for the response of the background electrons is required to determine the electric field. The simplest model is,

$$\mathbf{E} = -\eta \mathbf{j_f}. \tag{3.83}$$

Including the advection of a magnetic field with the fluid but neglecting the magnetic diffusion term gives,

$$\mathbf{E} = -\eta \mathbf{j_f} + \mathbf{u} \times \mathbf{B}. \tag{3.84}$$

The resistivity is calculated from a capped Spitzer resistivity model such that $\eta^{-1} = \eta_s^{-1} + \eta_0^{-1}$, where $\eta_s$ is the Spitzer resistivity given by,

$$\eta_s = 10^{-4}\frac{Z\ln\Lambda}{T_c^{3/2}}, \tag{3.85}$$

and $\eta_0 = 2\times10^{-6}$ Ωm. This tends to the Spitzer resistivity at high temperatures but is capped at low temperatures to the classical resistivity corresponding to a mean free path equal to the interatomic spacing, a conduction electron number density of $\sim 10^{29}$ m$^{-3}$ and a temperature of a few eV. This accounts for the transient regime that exists early in the simulations when the plasma temperature is relatively low due to the initial conditions.

### 3.6.2 Energy Coupling

Energy is transferred from the fast electron population to the background electrons via two routes. The first is collisional and is through the electron-electron drag term. The drag term acts to drive the two electron populations to some equilibrium energy, thus the fast electrons will decelerate and transfer their energy to the colder background electrons. The amount of energy transferred into the background at each time step is calculated by taking the difference between the energy moment (Eq. 3.17) before and after applying Eq. 3.52. This is followed by a thermalisation step in which, due to applying Eq. 3.52, the fast electrons with energies below the local background temperature are removed from the fast electron population and their total energy is transferred to the background electrons. Their number density is not conserved but, in the hybrid approximation, this is a negligible error.

The second energy coupling route is through Ohmic heating. As discussed in Section 2.4, the fast electron current, $j_f$ is in approximate detailed balance with a background, more resistive return current, $j_b$. Thus the Ohmic energy transfer rate is given by,

$$P_{\text{Ohmic}} = \eta j_f^2, \tag{3.86}$$

where $\eta$ is the capped Spitzer resistivity discussed in Section 3.6.1 and $j_f = \sqrt{j_{f,x}^2 + j_{f,y}^2}$ is the total fast electron current. Ohmic heating occurs between the solutions of the kinetic and hydrodynamic parts of the model, i.e. between solving Eq. 3.1 and Eqs. 3.61 to 3.63.

## 3.7 Summary of the Orders of Accuracy of Finite Difference Schemes

Table 3.1 provides a summary of the orders of accuracy in $\Delta x$, $\Delta p$ and $\Delta t$ of the finite difference schemes used in the hybrid model. Where no order of accuracy is given, the finite difference scheme does not depend on that parameter.

| | Differencing Scheme | $\Delta x$ | $\Delta p$ | $\Delta t$ |
|---|---|---|---|---|
| Kinetic | Advection (Section 3.4.3)[1] | Third | - | Third |
| | Electric Field (Section 3.4.4) | - | Second | Second |
| | Magnetic Field (Section 3.4.5) | - | - | Second |
| | Faraday's Law (Section 3.4.5) | First | - | First |
| | Electron-Ion Scattering (Section 3.4.6)[2] | - | - | - |
| | Electron-Electron Drag (Section 3.4.7) | - | First | First |
| Fluid | Two-Temperature Model (Section 3.5.2) | Second | - | Second |
| | Electron-Ion Thermal Equilibration (Section 3.5.3) | Second | - | Second |
| | Electron Thermal Conduction (Section 3.5.4)[3] | First | - | First |

[1] When the function is smooth, the domain uniformly discretised and in the limit of vanishing time step, PPM advection is fourth order accurate in space and time.

[2] Electron-ion scattering is solved analytically and so does not depend on any of $\Delta x$, $\Delta p$ or $\Delta t$.

[3] When the coefficient of thermal conductivity is spatially uniform, the scheme is second order accurate in space.

**Table 3.1: Summary of the orders of accuracy of the finite difference schemes used in the hybrid model. The column headings $\Delta x$, $\Delta p$ and $\Delta t$ refer to the orders of accuracy of the schemes according to the spatial, momentum and temporal time steps, respectively. The schemes are grouped according to whether they apply to the kinetic description or the fluid description.**

## 3.8 Code Validation

The implementation of the hybrid model has been validated against a number of test cases. This section contains a selection of these test cases, which have been designed to test the major components of the code working alone and in unison.

### 3.8.1 Plasma Oscillations and Landau Damping

The kinetic electron treatment is validated as a 1D Vlasov solver, that is with the collision terms turned off, by confirming that it can accurately reproduce warm plasma oscillations and Landau damping [78].

Plasma oscillations are induced by initialising a Maxwellian kinetic electron population with the temperature $T_f$ and a sinusoidal density profile in the $x$-direction:

$$n_f = \bar{n}_f \left(1 + \beta \sin\left(kx\right)\right), \tag{3.87}$$

where $n_f$ is the kinetic electron number density, $\bar{n}_f$ is the mean kinetic electron number density, $\beta$ is the magnitude of the perturbation, $k = \alpha/\lambda_D$ is the wave vector of the perturbation, $\lambda_D$ is the Debye length and $\alpha$ is a constant. It is assumed that there is a uniform, $Z = 1$, ion population such that the initial restoring electric field is,

$$E_x = \frac{e\bar{n}_f\beta}{\epsilon_0 k}\cos(kx). \tag{3.88}$$

Assuming that $k$ is sufficiently small such that the phase velocity of the oscillation, $v_\phi \gg v_{th}$ where $v_{th} = \sqrt{eT_f/m_e}$ is the kinetic electron thermal velocity, the electrons will oscillate at the warm plasma frequency:

$$\omega_{ph} = \sqrt{\omega_{pc}^2 + 3k^2 v_{th}^2}, \tag{3.89}$$

where $\omega_{pc}^2 = n_f e^2/\epsilon_0 m_e$ is the cold electron plasma frequency, and the current will be governed by,

$$j_x(x) = \frac{n_f e^2}{m_e \omega_{ph}} E_0(x)\sin(\omega_{ph} t). \tag{3.90}$$

In order to capture the oscillations in this test, the Ohm's Law electric field calculation (Eq. 3.83) was replaced with Ampere's Law such that,

| $\alpha$ | Phase error (%) | Amplitude error (%) |
|---|---|---|
| 0.10 | 0.04 | 4.0 |
| 0.15 | 0.09 | 6.0 |
| 0.20 | 0.28 | 6.4 |

**Table 3.2: The phase and amplitude errors in the warm plasma oscillations validation test. The phase error is given as the number of average time steps the solution is out of phase as a percentage of the total number of time steps taken, and the amplitude error is given as the average amplitude error as a percentage of the predicted amplitude.**

$$E_{x,j}^{n+1/2} = E_{x,j}^{n-1/2} - \Delta t \frac{j_{x,j}^{n}}{\epsilon_0}. \tag{3.91}$$

The wavevector of the perturbations is defined as $k = \alpha/\lambda_D$ and the spatial resolution as $\Delta x = 2\pi/knx$, with $nx = 32$. Thus one wavelength of the perturbation is imposed with periodic spatial boundaries. The momentum grid extends to ten times the thermal momentum, $p_{th}$ with $\Delta p = 0.02 p_{th}$. The time step is $\Delta t = 0.9\Delta t_{CFL}$ and $l_{max} = 30$.

The accuracy of model is calculated over ten periods of oscillation for a range of values of $\alpha$ and is given in terms of the phase and amplitude of the oscillations. The phase error is given as the number of average time steps the solution is out of phase as a percentage of the total number of time steps taken, and the amplitude error is given as the average amplitude error as a percentage of the predicted amplitude. Improving the spatial resolution also improved the temporal resolution because the dominant CFL condition is that of advection. Increasing this resolution improves the phase and amplitude errors approximately linearly. Once the momentum distribution is sufficiently resolved to allow for accurate phase matching between the perturbation and the discretised distribution function, there is only a slight improvement in the measures of accuracy. The angular distribution is found to be so well resolved that halving the number of harmonics made no difference to the result.

The results presented in Table 3.2 confirm that warm plasma oscillations can be accurately reproduced. It is expected that the errors should increase with increasing $\alpha$ because Eq. 3.89

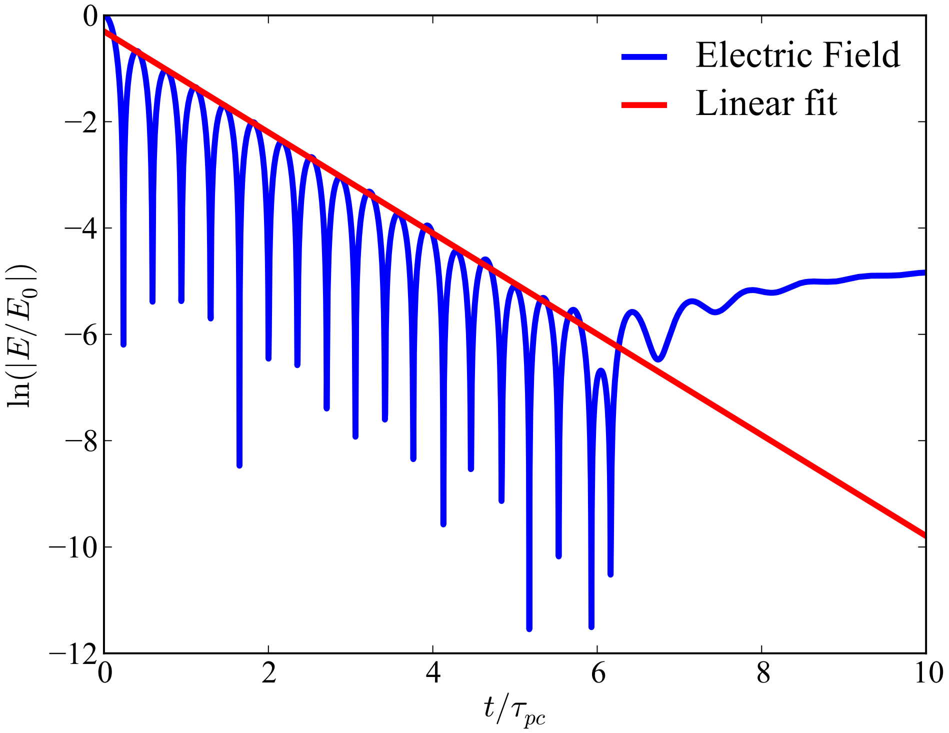

**Figure 3.3: Time evolution of the electric field amplitude under the effect of Landau. The blue line shows the decay of the amplitude of the oscillating electric field and the red line is a linear fit to the peaks of the second to seventh periods. The rate of the decay is calculated to be 0.15108$\omega_{pc}$, which is within 1.5% of the predicted value of 0.15336$\omega_{pc}$, and the frequency is calculated to be 1.54345$\omega_{pc}$, which is within 9% of the predicted value of 1.41566$\omega_{pc}$.**

assumes the thermal correction to be small compared to $\omega_{pc}$. However, for $\alpha = 0.2$ this correction is more than 10%. As $\alpha$ increases, the phase velocity of the oscillation decreases. Electrons in the steep decline of the distribution function then become in-phase with the perturbation and Landau damping becomes important. This is shown in Fig. 3.3, where $\alpha = 0.5$. The frequency of the oscillation is calculated by averaging over the second to seventh periods and is found to be 1.54345$\omega_{pc}$. This is within 9% of the predicted value of 1.41566$\omega_{pc}$. The rate of decay is calculated using a linear fit to the peaks of the second to seventh periods. It is calculated to be 0.15108$\omega_{pc}$, which is within 1.5% of the predicted value of 0.15336$\omega_{pc}$. A critical comparison of Vlasov solvers [79], obtains an error of 1.7% in the decay rate when using the PPM advection method and a momentum resolution that is three times lower than used in the hybrid model test. The need for greater resolution in the hybrid model results from the spherical harmonic expansion and using a lower order differencing scheme for momentum advection. Landau damping is found to occur when $(p_{th}/\Delta p)/l_{\text{max}} \gtrsim 1$.

### 3.8.2 Electron-Ion Scattering

As stated in Section 3.4.6, the expression for angular scattering of electrons from static ions (Eq. 3.47) amounts to an exponential decay of each spherical harmonic at a rate proportional to $l(l+1)/2$. Equation 3.47 is solved analytically in the hybrid model, it is trivial to confirm that angular scattering has been correctly implemented and this has been done.

### 3.8.3 Electron-Electron Drag

To validate the implementation of the electron-electron drag term in Equation 3.52, an approximately monoenergetic electron beam is injected into a uniform density DT plasma and the phase-space trajectory of the electrons is compared with the electron stopping model developed in Ref. 64, hereafter referred to as the Solodov model. As presented in Ref. 64, the Solodov model accounts for electron drag by solving Eq. 3.51 with Eq. 3.55 and accounts for electron scattering by calculating the scattering cross sections for the spatial moments of the electron distribution function represented as spherical harmonics, i.e. the model solves,

$$\frac{\mathrm{d}K}{\mathrm{d}x} = \langle\cos\theta\rangle^{-1}\frac{\mathrm{d}K}{\mathrm{d}s}, \tag{3.92}$$

where $K$ is electron kinetic energy, $s$ is the continuous range of the electron, $x$ is the range in the direction of the initial velocity, $\mathrm{d}K/\mathrm{d}s$ is equivalent to Eq. 3.51 in the classical limit and $\langle\cos\theta\rangle$ is the mean value of the $l = 0$ spherical harmonic. The implementation of this model has been validated against the quoted results in Ref. 64, including Fig. 1 therein, with excellent agreement. To allow for comparison with the electron-electron drag calculation in the hybrid model, the scattering term in the Solodov model is dropped and the Coulomb logarithm is replaced with Eq. 3.56.

In the test, the injected electron beam has a Gaussian energy distribution with a mean energy of 1 MeV, a FWHM of 5 keV and is beamed with $M = 16$ and $l_{max} = 17$. The domain is discretised with $nx = 150$, $\Delta x = 0.25$ $\mu$m, $np = 2200$ and $\Delta p = 0.0005p_{\text{th}}$, and the time step is fixed at 1 fs. The target is uniform with a density of 300 g/cm$^3$ and a temperature of 1 eV. Under these conditions, the Solodov model predicts a range of 24.2 $\mu$m. Figure 3.4 shows the predicted trajectory from the Solodov model overlaid on the phase-space contour plot of the fundamental harmonic from the hybrid model. The hybrid model gives a range of 23 $\mu$m.

There are a number of possible reasons for the difference between the Soldov model and the hybrid model measurements; 1) the Solodov model assumes a perfectly monoenergetic point source of electrons with momenta aligned with the $x$-axis. The hybrid model injects the electrons with energy and angular spreads. Both of these spreads affect the component of the initial electron momenta parallel to the axis and thus will affect the range, 2) there is likely to be some numerical diffusion in the hybrid model that will act to spread out the distribution function, 3) the injected electrons are equally likely to travel to the left as they are to the right. Those electrons travelling to the left will be reflected by the domain boundary and thus will cover a greater distance before leaving the injection region than those that went to the right. This, and the fact that the injection region is 1 $\mu$m wide, affect the final range and contribute to a spread in the range. However, even if this spatial issue is ignored, there is only a 5% error in the range. This error is consistent when 0.5 MeV and 0.25 MeV populations are injected with the same FWHM. The predicted ranges in these cases are 9.9 microns and 3.7 $\mu$m, respectively. The hybrid model yields 9.5 $\mu$m and 3.5 $\mu$m, respectively.

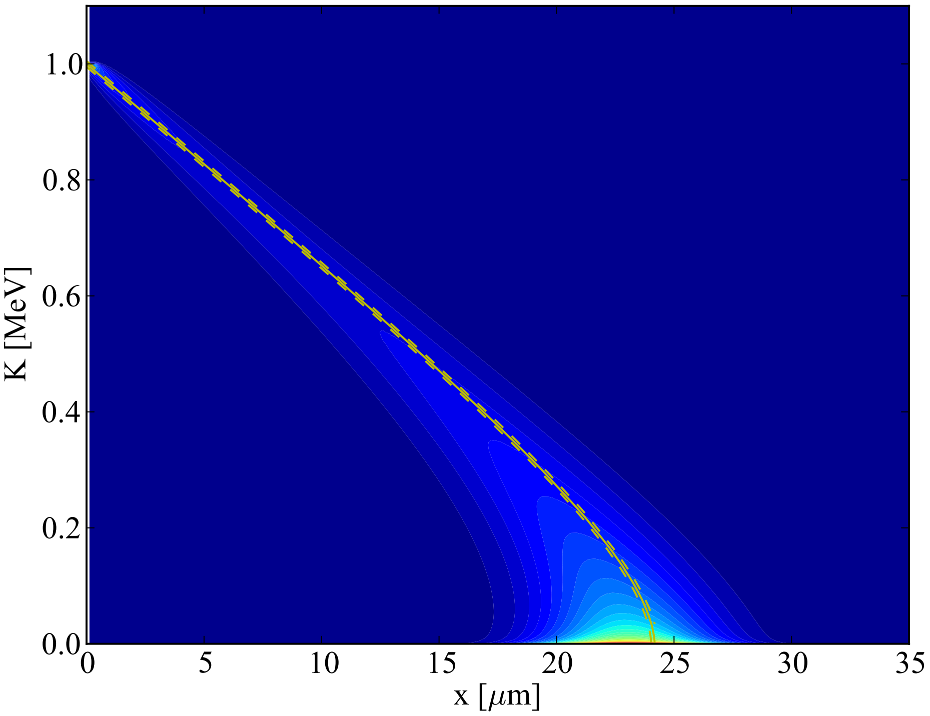

**Figure 3.4: The phase-space trajectory of a 1 MeV electron as calculated using the stopping model developed in Ref. 64 (yellow solid line), but with the scattering term ignored and the Coulomb logarithm calculated using Eq. 3.56, is compared with the phase space plot of the fundamental harmonic of an approximately monoenergetic 1 MeV electron population produced using the hybrid model (coloured contours). The target is uniform with a density of 300 g/cm$^3$ and a temperature of 1 eV. The electron energy distribution used in the hybrid model is gaussian with a mean energy of 1 MeV, a FWHM of 5 keV and is beamed with $M = 16$. The trajectories of electrons with energies equal to the energies at the FHWM of the distribution are represented by yellow dashed lines.**

The work in this thesis is primarily concerned with the shape and spatial extent of the energy deposition profiles produced by fast electron populations propagating through dense targets, so this small difference between the Solodov and hybrid results gives confidence that the forthcoming results are meaningful.

### 3.8.4 Rotation Under an Applied Magnetic Field

As discussed in Section 3.4.5, the application of a constant magnetic field amounts to an algebraic rotation of the spherical harmonics. Assuming that only the magnetic field is active in the model and that $l_{\text{max}} = 1$, Eqs. 3.38 and 3.39 yield,

$$\frac{\partial^2 f_1^0}{\partial t^2} = -\omega_g^2 f_1^0 \quad \text{and} \quad \frac{\partial^2 f_1^1}{\partial t^2} = -\omega_g^2 f_1^1. \tag{3.93}$$

Then, subject to the initial conditions that $f_1^0(t=0) = f_1^0(0)$ and $f_1^1(t=0) = 0$,

$$f_1^0 = f_1^0(0)\cos\left(\omega_g t\right) \quad \text{and} \quad f_1^1 = \frac{f_1^0(0)}{2}\sin\left(\omega_g t\right). \tag{3.94}$$

Thus, $f_1^0$ and $f_1^1$ and $j_x$ and $j_y$ will oscillate at the gyro-frequency $\omega_g = eB/m_e$. This is tested using the following abstract case. Suppose that,

$$f_0^0(0) = \exp(-a(p-\bar{p})^2) \quad f_1^0(0) = -\frac{1}{b}\exp(-a(p-\bar{p})^2). \tag{3.95}$$

Then, using the equation for $j_x$ in Eq. 3.18 and assuming, for simplicity, that $p = mv$, the amplitude of the oscillating currents, $j_x$ and $j_y$ are given by,

$$j = \frac{4\pi e}{3m_e b}\int_0^\infty p^3 \exp(-a(p-\bar{p})^2)\mathrm{d}p. \tag{3.96}$$

Finally, assuming that $a$ and $\bar{p}$ are sufficiently large that the lower limit of $\bar{p}$ can be replaced with $-\infty$ gives,

$$j = \frac{8\pi e}{3m_e b}\left[\frac{3}{4}\bar{p}\sqrt{\frac{\pi}{a^3}} + \frac{1}{2}\bar{p}^3\sqrt{\frac{\pi}{a}}\right]. \tag{3.97}$$

The errors in the amplitude and phase of the measured oscillating currents have been compared with these predictions. Ten gyro-periods, $\tau_g = 2\pi/\omega_g$ were simulated using time steps of $\tau_g/20$, $\tau_g/100$ and $\tau_g/500$. Improving the resolution, from the coarsest to the finest, reduced the phase error from 0.4% to <0.001% of the time step for $j_x$ and $j_y$. The error in the amplitude of the oscillation of $j_x$ and $j_y$ reduced from $\sim$1% to 0.005%, over the same range.

As discussed in Section 3.4.5, the magnetic field term is calculated implicitly so that the gyro-frequency does not need to be fully resolved. By repeating this test case, the scheme was found to be stable for time steps that exceed the gyro-period by a factor of a few. In each test, the amplitudes of the currents were found to always be within the predicted magnitude.

### 3.8.5 Sod Shock Tube

The implementation of the hydrodynamic module of the model is validated against the well known Sod shock tube problem [80] as depicted in Fig 3.5. In this test, only the hydrodynamic part of the model was used. The initial conditions consist of a diaphragm at $x = 2$, separating two regions of different densities and pressures, where the units are arbitrary. To its left, the density and pressure are both equal to 1, and to its right the density is equal to 0.125 and the pressure is equal to 0.1. An ideal gas with $\gamma = 1.4$ is assumed. The domain is discretised using 500 spatial cells and the time step is fixed at $10^{-4}$. At $t = 0$, the diaphragm is removed and the system evolves. Figure 3.5 compares the analytic solution and hybrid model solution at $t = 0.4$. In general, there is excellent agreement between the solutions. The minor differences that do exist can be most easily seen in Fig 3.5a and include a slight undershoot at the bottom of the rarefaction wave and at the bottom of the contact discontinuity. The transition of the contact discontinuity occupies nine to ten cells, while the transition for the shock occupies three to four cells. Ideally, these transitions should occur between two neighbouring cells. However, this is unlikely to be achieved in a finite difference scheme due to numerical diffusion resulting from the finite difference stencil and the finite size of the grid-spacing. In his seminal paper, Sod [80] compares how well several finite difference methods cope with the Sod shock tube problem. At the same spatial resolution, the hybrid model gives a better representation of the analytic solution over

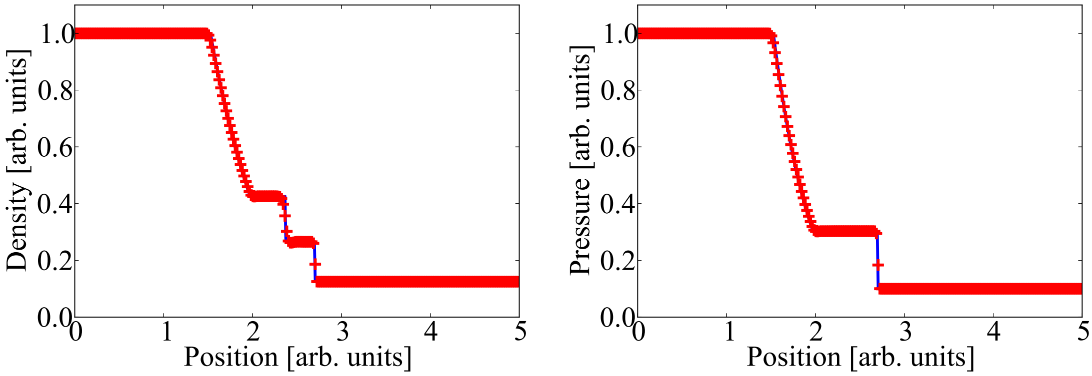

**(a) Density** **(b) Pressure**

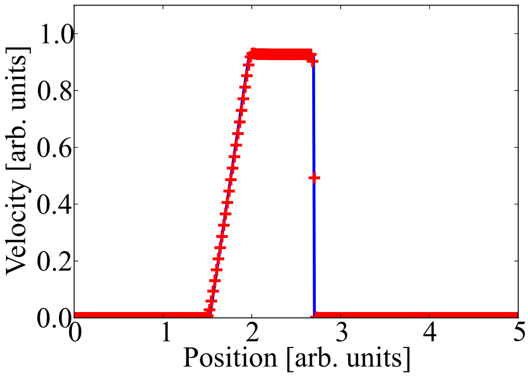

**(c) Velocity**

**Figure 3.5: The numerical solution (red dots) to the classic Sod shock tube problem [80] is compared with the analytic solution (blue line) at time $t = 0.4$, in arbitrary units. The fluid is initialised with a diaphragm at $x = 2$, separating two regions of different densities and pressures. To its left, the density and pressure are both equal to 1, and to its right the density is equal to 0.125 and the pressure is equal to 0.1. An ideal gas with $\gamma = 1.4$ is assumed. At time $t = 0$, the diaphragm is removed and the system is allowed to evolve.**

the whole of the profiles when compared with the most successful method considered in Ref. 80.

Ziegler [50] uses the magnetohydrodynamic shock tube problem Brio and Wu [81] as a test case. A direct comparison cannot be made with this test but one can make a visual inspection of how well the shock fronts are captured, how closely the smoothly varying regions are matched, and the nature of the small overshoots at the bottom of the rarefaction wave and the contact discontinuity. Such an inspection shows that the implementation of Ziegler's method in the hybrid model is comparable to the implementation in Ziegler [50].

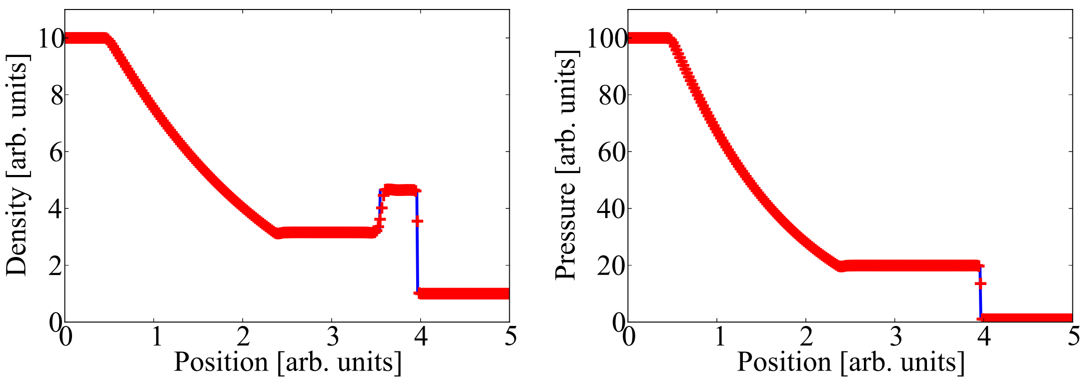

**(a) Density**

**(b) Pressure**

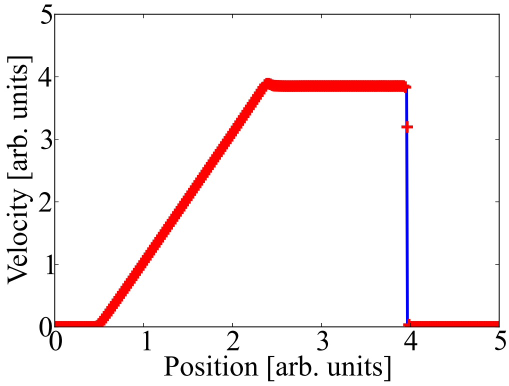

**(c) Velocity**

**Figure 3.6: The numerical solution (red dots) to a more challenging shock tube problem than the Sod shock tube problem is compared with the analytic solution (blue line) at time $t = 0.4$, in arbitrary units. The fluid is initialised with a diaphragm at $x = 2$, separating a region with a density of 10 and pressure of 100 to its left and a region with a density and pressure of 1 to its right. An ideal gas with $\gamma = 1.4$ is assumed.**

Figure 3.6 shows a similar comparison but for a more challenging scenario. As before, 500 spatial cells are used and the time step is fixed at $10^{-4}$. However, in this case, the density and pressure to the left of the membrane are 10 and 100, respectively, while to the right they are both 1. This produces stronger discontinuities across the shock interface and a narrow peak behind the shock. It is clear from Fig. 3.6 that the model has coped well with this problem. As was seen in Fig. 3.5, there is a minor undershoot at the foot of the rarefaction wave, the shock transition occupies three to four cells and the contact discontinuity occupies nine to ten cells.

The time step was varied by a factor of ten without any noticeable effect on the result. Doubling the spatial resolution improves the sharpness of the discontinuities but the number of cells occupied by the shock transition and the contact discontinuity remains the same.

### 3.8.6 Thermal Conduction Rate

The implementation of thermal conduction (Eq. 3.82) is tested by comparing the decay of a small amplitude sinusoidal temperature perturbation in a stationary, uniform density plasma against the analytic solution. Electron-ion equilibration is turned off.

The temperature perturbation is given by,

$$T_e = T_{e,0}\left[1 + \alpha \sin\left(\frac{n\pi x}{L}\right)\right], \tag{3.98}$$

where $T_{e,0}$ is the initial mean temperature, $\alpha$ is of the order of a percent to ensure classical transport theory holds, $n$ is an integer and $L$ is the domain size.

Using Eq. 3.81, one finds that the amplitude of the perturbation decays according to,

$$\alpha = \alpha_0 \mathrm{e}^{-t/\tau_D}, \tag{3.99}$$

where $\tau_D = D^{-1}\left(\frac{n\pi}{L}\right)^{-2}$ and $D = (\gamma - 1)\kappa/n_e e$ is the coefficient of diffusion of the electron temperature and $\alpha_0$ is the initial amplitude. It has been assumed that $\kappa$ is a constant across the domain and is calculated using the mean temperature $T_{e,0}$. In the test case $T_{e,0} =$ 500 eV and $\alpha =$ 0.01. Since the diffusion coefficient is proportional to $T_e^{5/2}$, this gives a mean to peak variation in $\kappa$ of $\sim$2.5%. The Coulomb logarithm is constant at 2, $L =$ 200 $\mu$m, $nx =$ 800 and the time step is fixed at 0.5 ps.

Figure 3.7a compares the decay of the initial amplitude as calculated using the hybrid model and using Eq. 3.99. There is excellent agreement, which is further highlighted in Fig. 3.7b, where the measured change in the amplitude from its initial value is given as a percentage of the predicted change. In this way, Fig. 3.7b shows the departure of the numerical result from the analytic

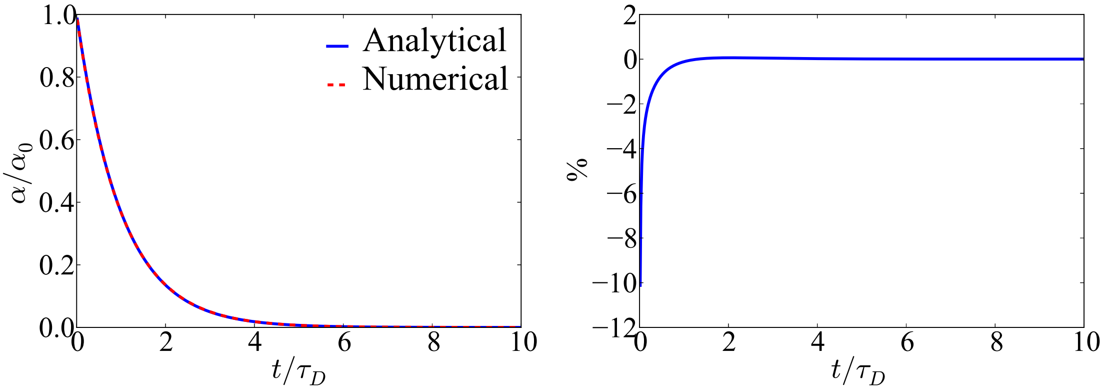

**(a)** **(b)**

**Figure 3.7: The thermal conduction routine is tested by comparing the decay of the amplitude of an electron temperature perturbation in a an otherwise uniform plasma. In Fig. 3.7a the time evolution of the decaying amplitude as calculated by the hybrid model (blue solid line) is compared with the analytic solution give in Eq. 3.99 (red dashed line). The amplitudes are normalised to the initial amplitude of the perturbation, $\alpha_0$. Figure 3.7b shows the measured change in the amplitude from its initial value, $(\alpha - \alpha_0)$ as a percentage of the predicted change.**

solution.

In this test, the time step is two orders of magnitude smaller than the diffusion time. This is two to three orders of magnitude larger than the fast electron advection time step in a typical simulation and is more than three orders of magnitude larger than the electron-ion collision time. This shows that the relatively crude implicit solution is sufficiently accurate.

## 3.9 Summary

A 1D planar hybrid model has been developed to model the generation of fast electron driven shock waves in dense target plasmas. The model combines a kinetic description of fast electron transport with a single-fluid, two-temperature hydrodynamic background plasma. These two descriptions are coupled through an Ohm's law description of the electric field and through energy transfer mechanisms. Where it is appropriate, a detailed account of the numerical schemes that have been used to solve the governing equations has been presented and, where well established numerical schemes have been used, the appropriate literature has been referenced. The model has been extensively validated against known problems and a selection of these tests has been presented. In all cases, the hybrid model has coped well. As will be seen in later chapters, the hybrid model has also proven itself capable of closely reproducing the results in more recent publications.

# Chapter 4

# A Précis of Fast Electron Generation in the Shock Ignition Regime

## 4.1 Introduction

Below the laser irradiance, $I_L \lambda_L^2 \sim 10^{14}$ W$\mu$m$^2$/cm$^2$, the growth of parametric instabilities such as stimulated Raman scattering (SRS) [11, 82], stimulated Brillouin scattering (SBS) [11] and two-plasmon decay (TPD) [83, 84] is slow and a large fraction of the laser energy is absorbed via inverse Bremsstrahlung [11]. Above this threshold, laser-plasma absorption becomes increasingly dominated by the parametric instabilities as the efficiency of inverse Bremsstrahlung wanes. These can significantly reduce the absorption efficiency by reflecting laser light out of the plasma [85], and they can lead to the production of suprathermal electron populations [11].

Early work on the conventional central hotspot ignition scheme used $CO_2$ lasers. Their long wavelengths (10.6 $\mu$m) and the required intensities ($\sim$few$\times$ $10^{14}$ W/cm$^2$) mean that copious numbers of hot electrons were produced. These are detrimental to the conventional central hotspot scheme because they are capable of penetrating deep into the assembling fuel, thereby pre-heating it and preventing sufficient compression from taking place [26]. The experimental observation of poor compression led to laser technology other than $CO_2$ being favoured. Emphasis has since been placed on Nd:glass lasers as these have a much shorter fundamental wavelength of 1.054 $\mu$m, which is usually frequency tripled to 351 nm, and the laser irradiance is reduced. Unfortunately, this reduced laser irradiance lies below that which is expected to be used in the ignitor pulse in shock ignition and, as a result, the regime of laser-plasma interaction relevant to the ignitor pulse has been little explored for many years.

In the shock ignition scheme (Section 2.5) the fuel is assembled using lower intensities than in the conventional central hotspot scheme, but then an intense spike in the intensity is required towards the end of the compression phase to drive a final ignitor shock into the target. At approximately $8 \times 10^{15}$ W/cm$^2$ and a wavelength of 351 nm, the irradiance of the ignitor pulse is well above the threshold for parametric instabilities to dominate the laser-plasma interaction. The question over the effect of these instabilities and the generation of hot electrons on the scheme was noted even in the earliest work on shock ignition [10, 31, 39].

Hot electrons may not be as detrimental to shock ignition as they have been to central hotspot ignition for a number of reasons [10, 31, 39]. The first is that the fuel will have undergone significant amounts of compression when the fast electrons are generated. The dense shell is expected to have an areal density of $\sim$10 mg/cm$^2$, which corresponds to the range of $\sim$100 keV electrons. Thus, it may be the case that moderately hot electrons will deposit their energy in the outer regions of the dense shell, contribute to the ablation pressure and help to drive the ignitor shock. An initial 1D numerical study of the effect of moderately hot 100 keV electrons on National Ignition Facility shock ignition targets found that their presence widened the ignition window as long as their range is less than the thickness of the dense shell [86]. The hot electrons may also smooth out inhomogeneities in the laser irradiation. It may then be the case that fewer, higher intensity lasers could be used to generate the ignitor shock or indeed longer wavelength lasers.

This thesis is primarily concerned with the role that hot electrons may play in strong shock wave generation and as such, a direct study of the parametric instabilities themselves lies outside of its scope. However, this chapter provides a précis of recent numerical simulations and experimental results that have been undertaken to investigate the generation of parametric instabilities in the context of shock ignition. This is done to orientate the reader and to motivate the choice of electron populations used in studies of electron driven shock wave generation presented in later chapters. The dynamics of, and competition between the various instabilities are complicated and will not be described here. For detailed studies see Refs. 87–91. Here, focus will be put on the global effect of the instabilities on the laser absorption efficiency and the characteristics of the fast electron populations that are produced.

## 4.2 Brief Overview of Parametric Instabilities

Stimulated Brillouin scattering (SBS) [11] is the decay of an incident electromagnetic wave into a scattered electromagnetic wave and an ion acoustic wave. The ion acoustic wave has a low frequency compared to the electromagnetic wave so SBS can develop anywhere in the plasma, up to the critical density and almost all of the incident energy can be transferred to the scattered wave. In this way, SBS can be responsible for greatly degrading the efficiency of laser absorption.

Stimulated Raman scattering (SRS) [11, 82] is the decay of an incident electromagnetic wave into a scattered electromagnetic wave and an electron plasma wave. The scattered electromagnetic wave must have a frequency greater than or equal to the electron plasma frequency. Thus, SRS can only develop up to one-quarter of the critical density. Part of the incident energy is carried out of the plasma by the scattered wave and part of the energy is absorbed into the electron plasma wave which in turn can generate suprathermal electrons through wave-breaking or damping [92].

A related instability is two-plasmon-decay (TPD) [83, 84]. This is the decay of an incident electromagnetic wave into two electron plasma waves near the quarter-critical density and it can also generate suprathermal electrons [93].

## 4.3 Experimental Evidence and Numerical Predictions for Fast Electron Generation in the Shock Ignition Regime

The effect of parametric instabilities becomes dominant above $I_L\lambda_L^2 \sim 10^{14}$ W$\mu$m$^2$/cm$^2$. Below this threshold, collisional absorption dominates. As the laser intensity increases, the plasma temperature increases, the electron collision frequency decreases and collisionless processes become dominant over collisional processes [11, 21]. The effect of transitioning from the collisional to the collisionless regime on laser absorption and fast electron generation has been considered using large-scale 1D spherical PIC simulations [87–89]. Laser-plasma interactions were simulated under conditions relevant to shock ignition with intensities of $1-24 \times 10^{15}$ W/cm$^2$. The realism of the initial plasma conditions used in the simulations has improved throughout this body of work as they have been motivated by assembled target profiles taken from hydrodynamic simulations of shock ignition experiments [94–96] that were performed at the OMEGA Laser Facility [97] using spherical deuterium gas filled plastic targets. However, the general conclusions are consistent throughout.

The PIC simulations reported a total laser energy absorption efficiency of $65-70\%$, almost irrespective of the intensity of the laser. This conclusion was not completely transparent from the articles but was confirmed by analysing the postscript data obtained from PDF versions of the articles. In particular, the author integrated the reflectivity data presented in Figure 2(a) of Ref. 89. Although the total absorption efficiency does not vary with intensity, the partition of absorption efficiency between collisional and collisionless processes does change with intensity.

At the lowest intensity of $1 \times 10^{15}$ W/cm$^2$, collisional processes dominate and 60% of the absorbed energy goes into increasing the temperature of the thermal electrons from an initial value of 2 keV to 2.5 keV. A further 20% of the absorbed energy (13% of the laser energy) goes into creating $10-30$ keV electrons, of which just 5% is due to the collisionless SRS process and 15% is attributed to heating by inverse Bremsstrahlung. The low SRS backscatter rate and absence of hot electrons are both consistent with results measured at the OMEGA Laser Facility [95, 96] but the total reflectivity ($\sim$10% in experiment) is somewhat higher in the simulations.

As the laser intensity increases, the collisionless processes increasingly dominate over the collisional processes with the fraction of the absorbed energy being absorbed into electrons via collisionless processes increasing from 5% at $1 \times 10^{15}$ W/cm$^2$ to 70% at $2.4 \times 10^{15}$ W/cm$^2$ and 93% at $8 \times 10^{15}$ W/cm$^2$. Three populations of electrons can be distinguished above an intensity of $2.4 \times 10^{15}$ W/cm$^2$. At intensities of a few $10^{15}$ W/cm$^2$, a population with a temperature of $7-8$ keV is dominant. Over about $5 \times 10^{15}$ W/cm$^2$, a population with a temperature of 28 keV becomes dominant and forms a directional beam into the target. Finally, at a few $10^{16}$ W/cm$^2$, a small population with a temperature of 100 keV appears when the density profile starts to flatten. This flattening is not seen in 2D simulations [90, 91] so the generation of this 100 keV population needs to be investigated. Furthermore it is not reported in experiment [96]. The temperatures of the electrons produced do not significantly depend on intensity but the numbers of hot electrons scale linearly with intensity.

The prominence at higher intensities of an electron population with a temperature of 30 keV carrying $50-55$% of the laser energy is consistent with the observations in OMEGA experiments [95, 96], as is the total reflectivity measurement (36% in experiment and $\sim$35% in simulations). However, the experimentally measured rate of SRS backscatter of 24% is more modest than in the

PIC simulations.

Shock ignition studies have also been performed using planar targets at the Prague Asterix Laser Facility (PALS) [98], at the Laboratoire d'Utilisation des Lasers Intenses (LULI) [99] and at the OMEGA Laser Facility [100]. These three experimental campaigns followed the same general approach but differ on the details. They each irradiated a planar target at a relatively low intensity in order to create a pre-plasma, and followed this with a spike in the intensity in order to drive a shock wave through the target and to possibly stimulate parametric instabilities. Taken collectively, these planar experiments and the PIC simulations do broadly agree on a mean fast electron energy of a few tens of keV. For example, a conversion efficiency of 2% to fast electrons with a temperature of 70 keV was achieved in the OMEGA experiment when using a peak spike intensity of $1.4 \times 10^{15}$ W/cm$^2$. The PALS experiment used a peak spike intensity of $1 \times 10^{16}$ W/cm$^2$ and measured a low conversion efficiency of just 0.1% to hot electrons with a mean energy of 50 keV. The LULI experiment could only potentially detect electrons with energies above 60 keV and this signal was always below the noise level. Using a spike intensity of up to $1 \times 10^{15}$ W/cm$^2$, a low conversion efficiency of 0.1% to fast electrons with energies above 60 keV is estimated.

It is expected that the pre-plasma produced in shock ignition will have a long scale length of a few hundred microns and will have a temperature of a few keV. These are difficult conditions to achieve and it is unlikely that these planar target experiments truly accessed the shock ignition regime. For example, while the spike pulse used in the PALS experiment best matches the spike envisaged for shock ignition, the compression laser did not contain enough energy to heat the pre-plasma above 175 eV, and the pre-plasma scale length was just a few tens of microns. The low conversion efficiency to hot electrons and the relatively low measured backscattering rates of $6-15\%$ also indicate that a regime dominated by collisionless absorption was not accessed. In fact, the experimental results compare more favourably with the collisional regime presented in Ref. 88, but even then the numerical results predict higher backscattering rates.

Alternatively, it may be the case that the 1D simulations overestimate the role of parametric instabilities and hot electron generation in the shock ignition regime. For example, the primary reason the 1D simulations showed such efficient laser absorption was because SBS was strongly suppressed by cavitation. The 1D geometry cannot capture processes such as TPD and cavity expansion. Some 2D PIC simulations [90, 91] have been performed to understand their importance and how they interrelate. Although the dynamics between the various processes are complicated, the broad conclusions of these 2D simulations are in agreement with the 1D simulations [87–89]; SBS and TPD are only active for an initial transient time, after which the laser absorption is dominated by SRS below the quarter-critical density and a hot electron population with a temperature of $30-50$ keV is produced. These observations agree with experiments [93, 94, 96].

## 4.4 Summary

The shock ignition ignitor pulse lies in a little explored regime of laser-plasma interaction. The intensity of the ignitor pulse is well above the threshold for the stimulation of parametric instabilities and the pre-plasma is expected to be hot and have a long scale length compared to conventional central hotspot ignition. It is not immediately clear how the combination of these two points will affect the laser absorption efficiency or the stimulation of parametric instabilities and the subsequent generation of suprathermal electron populations. These issues have begun to receive significant attention and this chapter has provided a synopsis of the numerical and experimental studies that have been undertaken, with a particular focus on the questions over fast electron generation; namely the conversion efficiency and their mean energy.

It would appear to be challenging to truly access the shock ignition regime using the current laser facilities. However, smaller scale experiments can be used to address specific issues. After comparison with 1D and 2D PIC simulations, it seems that a particular success has been the characterisation of the mean energy of the fast electrons generated during the ignitor spike. This is likely to be around $30-50$ keV. There is a greater discrepancy between the numerical simulations and the experiments with regards to the plasma reflectivity and the conversion efficiency into fast electrons. Simulations predict a fairly constant reflectivity of $30-35\%$ over the range of $1-10 \times 10^{15}$ W/cm$^2$, whereas experiments show a varying reflectivity of $10-35\%$ over the same range. A low reflectivity is beneficial to the efficiency of any inertial confinement scheme. Correspondingly, the conversion efficiency of laser energy to hot electrons is consistently higher in the simulations than in the experiments. A low conversion efficiency would reduce the potential issue of pre-heat but if fast electrons are found to be beneficial it may prove desirable to deliberately stimulate their production by, for example reducing the use of beam smoothing techniques, increasing the laser intensity or increasing the laser wavelength.

# Chapter 5

# The Effect of Extended Energy Distributions on Shock Peak Pressure

The work detailed in this chapter has been published in Physics of Plasmas: T. E. Fox, A. P. L. Robinson, J. Pasley, *"Strong shock generation by fast electron energy deposition",* Phys. Plasmas, **20**, 122707 (2013).

## 5.1 Introduction

Chapter 4 reviewed the growing body of evidence that suggests that the production of moderately hot electron populations should be expected during the ignitor spike of shock ignition. The exact nature of this population is not fully understood but, with experimental and numerical support, it appears reasonable to assume that it will be dominated by a 30 keV Maxwellian distribution. Electrons with energies of $20-100$ keV have ranges of approximately $1-15$ mg/cm$^2$ [64], which is comparable to the areal density of the assembling fuel at the time of the ignitor pulse. The possibility then exists to use fast electrons to help drive strong shocks by having them deposit their energy in the outer regions of the dense shell.

The first analytic and numerical studies [43, 44] of hot electron driven shock wave formation in the context of shock ignition assumed monoenergetic populations of hot electrons with temperatures of 30 keV and 100 keV. These populations were continuously injected with intensities of 1 PW/cm$^2$ and 10 PW/cm$^2$, respectively, into a 1D planar, DT, step-like target with a density of 10 g/cm$^3$ and a temperature of 1 eV. It was found that strong shocks could be driven with up to 10% of the driver energy going into the shock wave with a pressure amplitude of several hundred Mbars or more.

It will be demonstrated that compared with monoenergetic energy distributions, Maxwellian distributions are expected to produce very different energy deposition profiles in uniform targets. It is not immediately clear what effect this change in the energy distribution will have on the ability of the hot electron population to drive strong shocks or the peak pressure that can be achieved. In this chapter, this is investigated using electron populations with energy distributions that produce heating profiles in uniform plasmas that are well behaved with a single peak and can be well described by a spatial scale length. Initial first-order analytic arguments suggest that there should be little or no effect on the peak pressure. This is confirmed with numerical calculations which show that equivalent peak pressures and greater driver-shock power efficiency can be achieved using Maxwellian beams compared to monoenergetic beams. The measured peak pressures agree well with the analytic scalings however, the time taken to reach it increases with increasing scale length. Furthermore, if the target is not sufficiently long compared to the scale length of the heating profile, the shock wave will not fully develop. This has implications for shock ignition where the targets are of a finite size and ignition requires careful timing of the shock waves. This places a restriction on the allowable fast electron temperature for a given target density.

## 5.2 Theory

It follows directly from Eq. 3.51 that the stopping distance, $\lambda_f$ of a fast electron depends only on its energy, $K$ and the background electron density $n_e$:

$$\lambda_f \simeq \frac{4\pi\phi\epsilon_0^2 K^2}{n_e e^4 \ln\Lambda}\ \mathrm{m}, \tag{5.1}$$

where non-relativistic electrons have been assumed, $\phi$ is a numerical factor introduced to account for electron-ion scattering and $\ln\Lambda$ is the Coulomb logarithm. The energy distribution of a fast electron population therefore determines the shape of the heating profile produced in a uniform plasma.

Figure 5.1 shows the qualitative differences between the energy deposition profiles created by 30 keV monoenergetic and Maxwellian electron beams incident on a stationary, planar, DT target at 10 g/cm$^3$ and 1eV, with a 0.1 g/cm$^3$ pre-plasma at 1eV. The dots are the results obtained by using the Solodov model, developed in Ref. 64 and introduced in Section 3.8.3, to perform a weighted integral over the energy deposition profiles of individual electrons with a range of initial kinetic energies. The scattering term is included and the Coulomb logarithm is calculated using Eq. 3.56. The green dots are for a 30 keV Maxwellian beam while the blue dots are for a 30 keV monoenergetic beam. The green and blue solid lines are the deposition profiles obtained using the hybrid model without hydrodynamic motion. The profiles show that a monoenergetic beam will heat a narrow layer close to the surface of the target. On the other hand, the Maxwellian beam will produce a much broader heating profile. Further to the reasons for the difference between the Solodov model and the hybrid model that have been discussed in Section 3.8.3, the electric field is active in these hybrid simulations. This will act to slow the electrons and slightly enhance energy deposition.

In reality, the target will not be stationary but will expand in response to the heating profile.

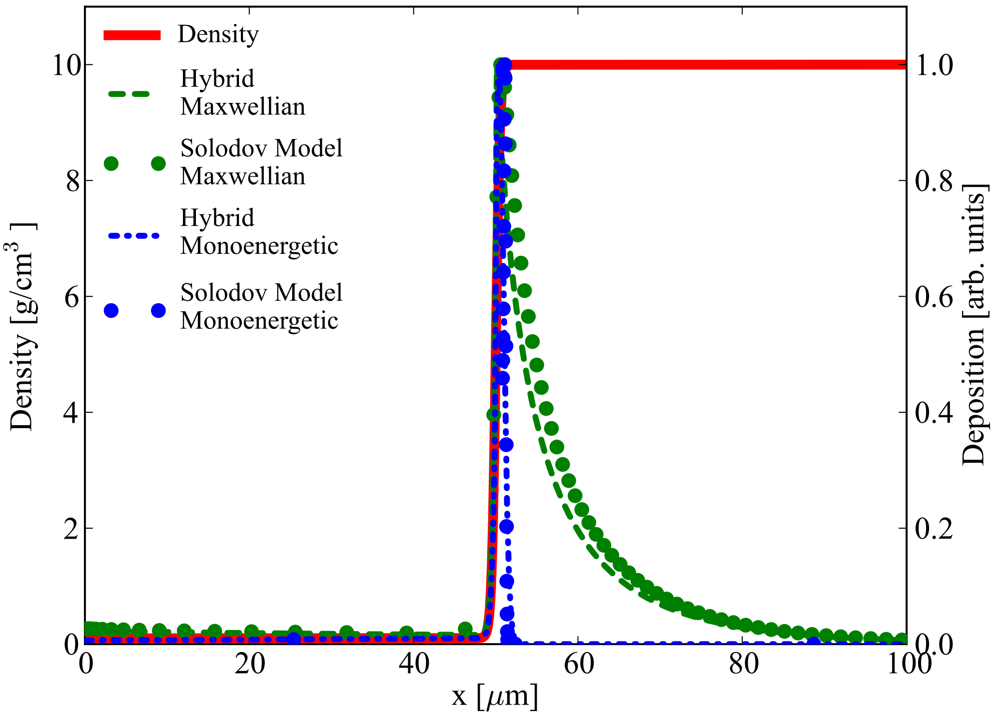

**Figure 5.1: Comparing the deposition profiles created by 30 keV Maxwellian (green) and monoenergetic (blue) electron beams in a 10 g/cm$^3$ uniform density target with a 0.1 g/cm$^3$ pre-plasma (red). The solid green and blue lines are the deposition profiles produced using the hybrid code without hydrodynamic motion. The dots are the deposition profiles produced using the Solodov model developed in Ref. 64 but with the Coulomb logarithm calculated using Eq. 3.56. It is clear from these results that Maxwellian electron populations produce more extended deposition profiles, compared to monoenergetic electron populations.**

The plasma will rarefy to the left and, if the heating is sufficiently intense, a shock wave will be driven to the right. This hydrodynamic expansion causes the pressure in the heated region to drop. The time available to produce the peak pressure is therefore given by the time taken for the rarefaction wave to cross the heated region at the sound speed, $t \simeq \mathcal{L}/c_s$. Here, it is assumed that the heating profile produced by the fast electron population is well behaved, with a single maximum and can be well described by a spatial scale length $\mathcal{L}$.

Assuming an ideal gas, the temperature in the non-expanding, heated region will increase linearly in time:

$$T = \frac{2}{3}\frac{Im_i}{(Z+1)\rho e\mathcal{L}}t\ \text{eV}. \tag{5.2}$$

Here, $I$ is the incident electron beam intensity in W/m$^2$, $t$ is the pulse length in seconds, $Z$ is the atomic number of the target ions, $m_i$ is the average ion mass in kg, $\rho$ is the mass density in kg/m$^3$, $\mathcal{L}$ is in metres and $e$ is the electronic charge in Coulombs. The sound speed then evolves according to,

$$c_s = \sqrt{\frac{5}{3}\frac{eT}{m_i}} \simeq \sqrt{\frac{It}{(Z+1)\rho\mathcal{L}}}\ \text{m/s}. \tag{5.3}$$

Thus, $t = \mathcal{L}/c_s = \mathcal{L}\,(2\rho/I)^{1/3}$ for $Z = 1$ and the maximum pressure becomes independent of $\mathcal{L}$:

$$P_{\text{max}} \simeq 195 I_{\text{PW}}^{2/3}\rho_{\text{gcc}}^{1/3}\ \text{Mbar}. \tag{5.4}$$

Here, $I_{PW}$ is the electron beam intensity in PW/cm$^2$ and $\rho_{\text{gcc}}$ is in g/cm$^3$. This scaling has been arrived at previously using a steady state ablation model of a laser irradiated solid [101] and the self-similar solution of the isothermal rarefaction wave of a constant mass [43, 102], but with minor differences in the numerical prefactor.

The spatial extent of the heating profile, characterised by $\mathcal{L}$, is the one link between the energy distribution and the shape of the pressure profile it creates and it does not feature in Eq. 5.4. Keeping in mind the criteria placed on the distribution, the achievable peak pressure should therefore be a weak function or independent of the exact nature of the distribution, i.e. Maxwellian and monoenergetic beams of the same intensity and pulse length should produce equal peak pressures.

The scaling law in Eq. 5.4 will now be confirmed via numerical simulations. This investigation begins with the case of shock wave generation using monoenergetic electron populations to reproduce the results of Ref. 43 and to create baseline results to compare with the case of shock wave generation using Maxwellian electron populations. First, an overview of the simulation setup is presented. Only the intensity, mean energy and energy distribution of the hot electron populations

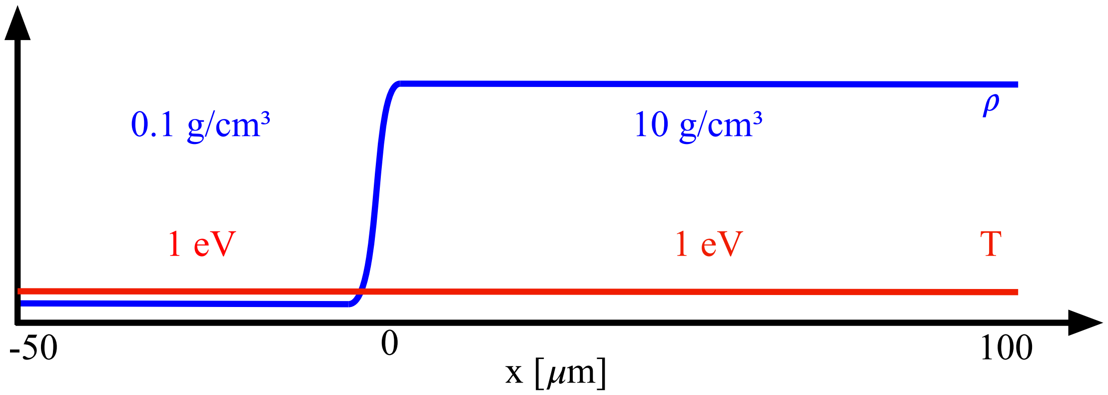

**Figure 5.2: Schematic of the background plasma initial conditions. The stationary, DT target is 100 $\mu$m long with a density of 10 g/cm$^3$ and a temperature of 1 eV. This is preceded by a 50 $\mu$m DT plasma at 0.1 g/cm$^3$ and 1 eV. The transition in density is smoothed using a tanh function to avoid numerical instabilities. The fast electron populations are injected from the left hand side.**

is changed between simulations.

## 5.3 Description of the Simulation Design

The simulation design was chosen by taking into account the parameters expected for shock ignition and also to allow for direct comparison with the findings of Ref. 43. A schematic of the chosen simulation design is shown in Fig. 5.2. It shows a 100 $\mu$m uniform density target at 10 g/cm$^3$ and 1 eV, with a step-like profile preceded by a 50 $\mu$m low density pre-plasma at 0.1 g/cm$^3$ and 1 eV. The step profile is smoothed using a tanh function with a scale length of 2 spatial cells to avoid numerical instabilities. This is reasonable as one would not have perfect step profiles in reality. The plasma is modelled as a fully ionised average DT ion with a mass of 2.5m$_p$ and $Z = 1$.

The laser-plasma interaction processes that generate the fast electron populations are not included in a self-consistent way. Instead, it is assumed that these processes result in a source of fast electrons in the pre-plasma some appreciable distance from the target. For the simulations, this amounts to a continuous injection of fast electrons over the first micron of pre-plasma at the left-hand boundary. The possible effects of pre-plasma evolution on the rate or location of the fast electron source is not included. The fast electron population encounters a reflective boundary at the left hand side of the domain, while those electrons that are energetic enough to traverse the length of the domain can leave through an open boundary.

Monoenergetic distributions are approximated by Gaussian distributions with appropriate mean energies and a full-width-half-maximum (FWHM) of $\sim 7\%$ of the mean energy. Maxwellian distributions have appropriate thermal temperatures and have the lower $20-25\%$ of energy in the Maxwellian removed prior to injection to remove the highly collisional lowest energy electrons. This gives a lower on-target intensity than quoted. All injected distributions are 'beamed' with $M = 16$.

The hydrodynamic model has an outflow boundary at the left-hand side to allow the ablating plasma to escape and a reflective boundary at the right-hand side. When flux limited electron thermal conduction is included a flux limiter of 0.05 is used, along with open boundary conditions. Unless otherwise stated, the presented results are from simulations including thermal conduction.

Convergence testing and the simulation time guided the choice of simulation parameters. In all simulations, the fast electron population is represented using eighteen spherical harmonics. Higher numbers of harmonics produce only minor changes in the fast electron transport. The spatial domain is discretized using 600 spatial cells and $\Delta x = 0.25$ $\mu$m. This sufficiently resolves the energy deposition profiles produced by the fast electron populations used in this study. Finer resolution produces smoother energy deposition profiles but has a negligible effect ($\sim 1\%$) on the shock wave generation or the peak pressure achieved. When injecting a monoenergetic electron beam, the momentum domain is discretized using 150 momentum cells and $\Delta p = 0.008 p_{\text{th}}$, where $p_{\text{th}}$ is the momentum corresponding to the fast electron mean energy. When injecting a Maxwellian electron beam, 75 cells are used with $\Delta p = 0.1 p_{\text{th}}$. Finer momentum resolution in either case has a negligible effect on the fast electron transport and changes the measured peak pressure by ∼0.5%. The time step is determined by the most stringent of the Courant conditions in the model. Varying the time step from 0.5 to 0.9 of the Courant condition only affects the peak pressure measurement by ∼0.1%. A time step of 0.9 of the Courant condition is used throughout.

The hybrid model does not include radiation transport. The potential role of radiation transport was assessed *a posteriori* by considering the optical depth of the plasmas under the conditions created during the simulations presented in this chapter. This will be discussed in more detail in Section 5.6

## 5.4 The Effect of Introducing an Energy Extended Distribution

A baseline simulation was created by reproducing Case 1 in Ref. 43 where a 30 keV monoenergetic beam was injected continuously with an intensity of 1 PW/cm$^2$. In the baseline simulation, the monoenergetic beam is approximated by a Gaussian with a mean energy of 30 keV and a FWHM of 2 keV. Figure 5.3 shows the resulting plasma pressure and density profiles. The restricted range of mean-free-paths rapidly produces a tight pressure profile with a peak of 350 Mbars after 26 ps. This peak pressure is close to the 360 Mbars predicted by Eq. 5.4 and, bearing in mind that the actual intensity in this simulation is reduced, this agrees well with the 400 Mbars measured in Ref. 43. The measured time taken to achieve the peak pressure is in similarly good agreement with Ref. 43, where it took ∼20 ps.

Once the peak pressure has been reached, the plasma ablates, a forward going shock wave quickly develops and the pressure drops. The ablating material restricts the amount of incoming electron energy by enhancing deposition in the pre-plasma. This is shown in Fig. 5.4, where the power density deposition profiles are overlaid on the density profiles. It shows that, at 100 ps, there is greater deposition in the pre-plasma compared to at 200 ps. At later times the initial

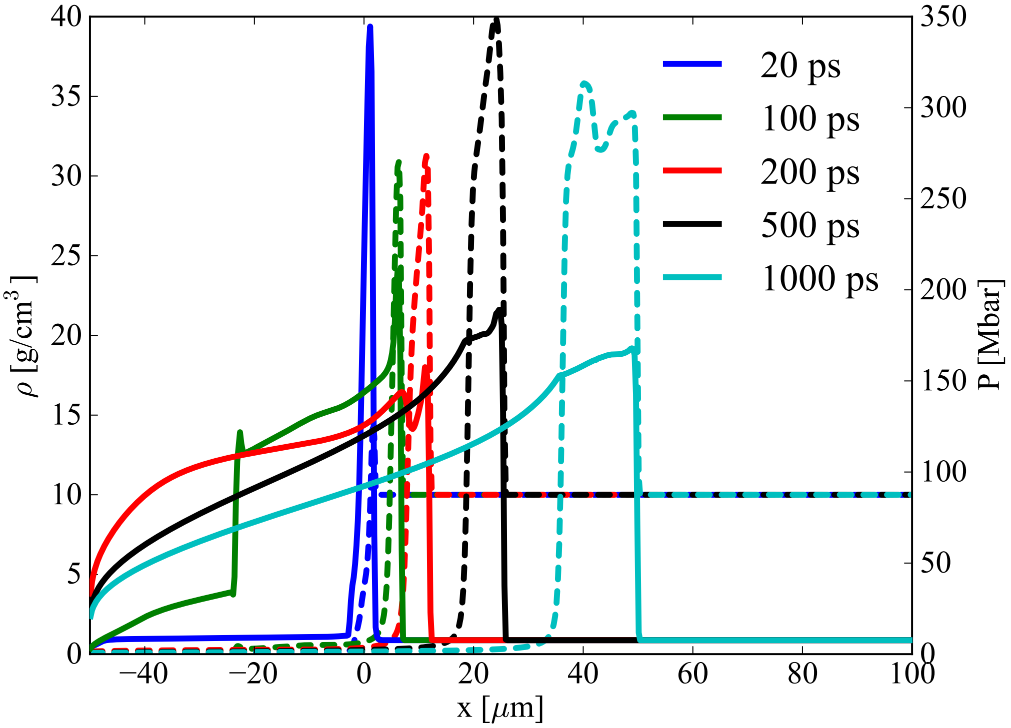

**Figure 5.3: Time evolution of pressure (solid) and density (dashed) profiles of the plasma subject to a monoenergetic electron beam with a temperature of 30 keV and an intensity of 1 PW/cm$^2$.**

outflowing wave of plasma has escaped the simulation domain. The reduced density in the pre-plasma at this later time allows greater deposition at the rear of the decaying shock, enhancing its pressure and density as shown at 500 ps. The electron deposition front and the shock front are no longer co-located as they once were. Instead, the electron deposition front tracks along the rear of the peak and the pressure across the shock drops. The effect of the outgoing plasma is likely to be diminished by expansion in a spherical geometry. After 1000 ps, the pressure has dropped to 170 Mbars and has the triangular shape characteristic of a blast wave. The shock wave is propagating at $D_{\text{sh}}$ ~48 $\mu$m/ns giving a shock power, $p_{\text{sh}} = P_{\text{sh}} D_{\text{sh}}$, of about 80 TW/cm$^2$ and a driver efficiency of $\sim$8%. This is in line with the findings in Ref. 43, where a maximum efficiency of $\sim$10% is predicted and an efficiency of 7% was measured.

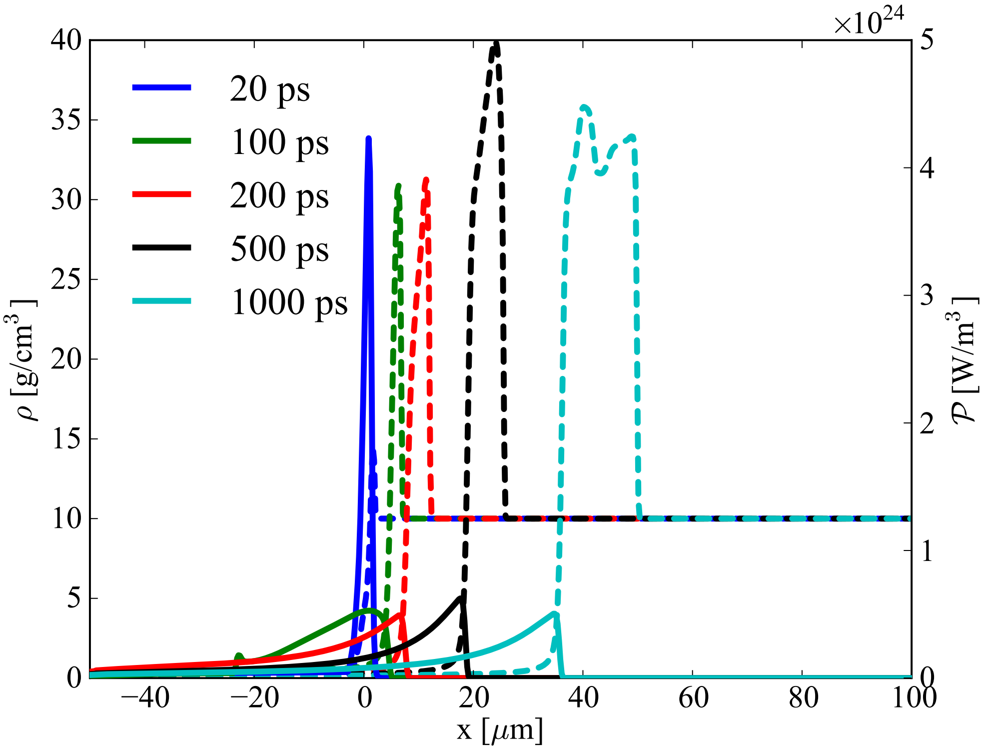

**Figure 5.4: Time evolution of power density deposition (solid) and density (dashed) profiles of the plasma subject to a monoenergetic electron beam with a temperature of 30 keV and an intensity of 1 PW/cm$^2$.**

The correspondence between the results presented here and those presented in Ref. 43 is encouraging. The CHIC model used in Ref. 43 is arguably more detailed as, compared to the present hybrid model, it includes detailed radiation transport with tabulated ionisation and opacity data, non-local thermal transport and additional coupling mechanisms between the kinetic and hydrodynamic modules. However, the agreement between the two models suggests that, despite their notionally significant differences, the present hybrid model does capture the dominant physics in the regime of interest and its relative simplicity draws attention to these key processes. Thus, the present hybrid model can be used with some confidence in this regime.

The effect of an extended energy distribution is now considered. Figures 5.5 and 5.6 are equivalent to Figures 5.3 and 5.4, respectively, but for a 30 keV Maxwellian beam. They show

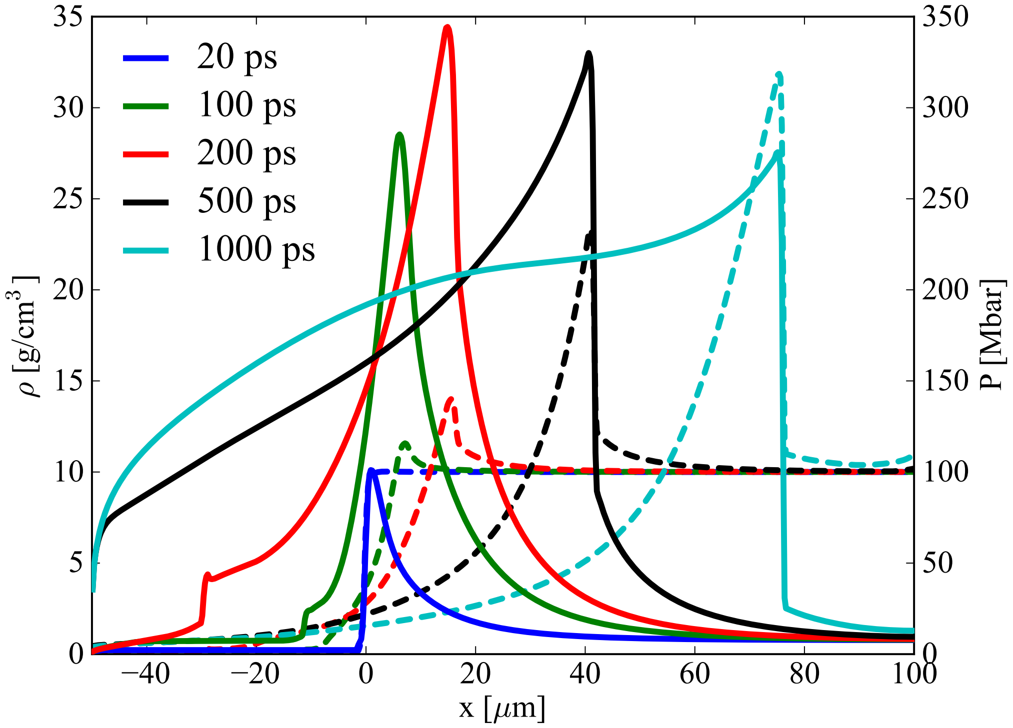

**Figure 5.5: Time evolution of pressure (solid) and density (dashed) profiles of the plasma subject to a Maxwellian electron beam with a thermal temperature of 30 keV and an intensity of 1 PW/cm$^2$.**

that the greater range of mean-free-paths in the distribution produces a much broader heating profile. The same peak pressure of 350 Mbars is achieved but not until after the much later time of 280 ps. During this time, the density profiles show the formation of a shock wave in the plasma but with a much more extended profile at the rear of the shock front. The deposition front continues to track the shock front for the duration of the simulation (see Fig. 5.6) but with an increasing proportion of the injected energy being deposited in the exhaust fluid that is moving towards the injection region, so the shock pressure decays. At 1000 ps, the pressure is 275 Mbars and the shock speed is $\sim$68 $\mu$m/ns, giving a shock power of about 190 TW/cm$^2$ and a driver efficiency of $\sim$19%. The increased efficiency is due to the continued energy deposition in the shock front by the hotter electrons in the Maxwellian distribution. Removing this continued deposition by turning off

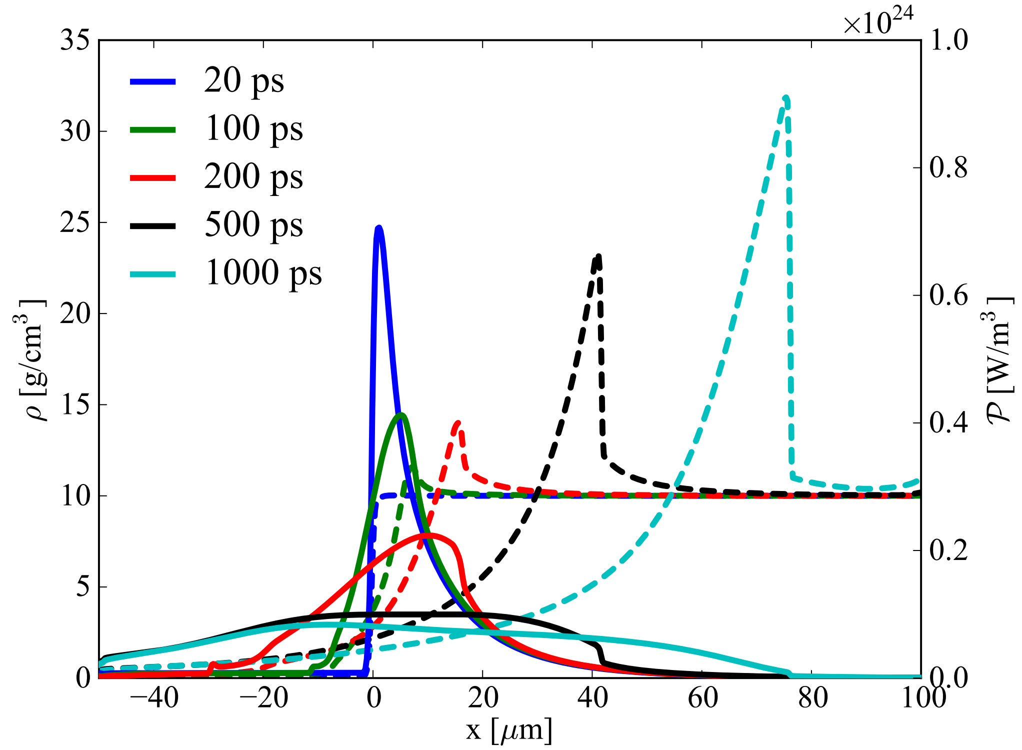

**Figure 5.6: Time evolution of power density deposition (solid) and density (dashed) profiles of the plasma subject to a Maxwellian electron beam with a thermal temperature of 30 keV and an intensity of 1 PW/cm$^2$.**

fast electron injection after 280 ps gives a more rapidly decaying pressure profile. After 1000 ps, the peak pressure is 160 Mbars and the shock speed is ∼60 $\mu$m/ns giving a shock power of about 96 TW/cm$^2$ and a driver efficiency of ∼10%.

For completeness, Figs. 5.7a and 5.7b show the time evolution of the background electron and ion temperatures for the cases of heating by 30 keV monoenergetic and Maxwellian electron beams, respectively. In general, the two temperatures do not differ significantly due to rapid thermal equilibration under the conditions that have been studied. The monoenergetic beam is more collisional than the Maxwellian beam and so produces a hotter low-density pre-plasma, although the temperature of the shock wave is ∼10 eV in both cases. The location of the shock wave in the monoenergetic case corresponds to the ‘shelf’ at the leading edge of the temperature

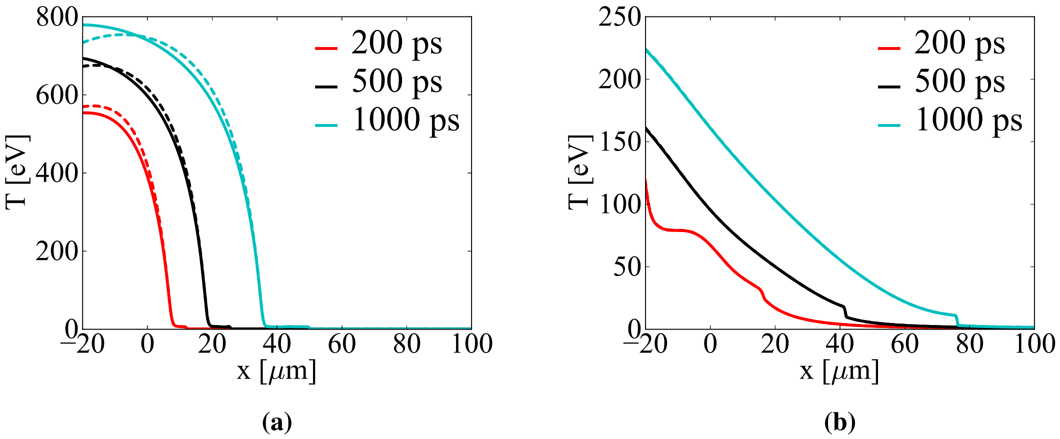

**Figure 5.7: Time evolution of the background electron (solid) and ion (dashed) temperatures. Figure 5.7a corresponds to the case of heating by a monoenergetic electron beam with a temperature of 30 keV and an intensity of 1 PW/cm$^2$. Figure 5.7b corresponds to the case of heating by a Maxwellian electron beam with a thermal temperature of 30 keV and an intensity of 1 PW/cm$^2$. The electron and ion temperatures are indistinguishable in Fig. 5.7b.**

profiles. The range of mean free paths in the Maxwellian population produces broader temperature profiles and the longer mean free paths of electrons in the tail of the distribution increase the temperature ahead of the shock front, the location of which is indicated by a step in the temperature profiles.

## 5.5 Maximum Pressure and its Temporal Dependence

The study is now extended to verify the scaling law between peak pressure and intensity given in Eq. 5.4 and its independence of the spatial extent of the heating profile. Figure 5.8 shows the prediction of Eq. 5.4 assuming a constant density of 10 g/cm$^3$ (red solid line) and marked by diamonds are the peak pressures achieved using 20 keV (pink), 30 keV (blue), 40 keV (black) and 50 keV (cyan) Maxwellian beams and using a 30 keV monoenergetic beam (green). Results of 30 keV Maxwellian and monoenergetic beams without thermal conduction are represented by blue and green stars, respectively.

Overall, the simulation results compare well with Eq. 5.4 suggesting that the simple model presented in Section 5.2 captures the essential physics. The 30 keV Maxwellian and monoener-

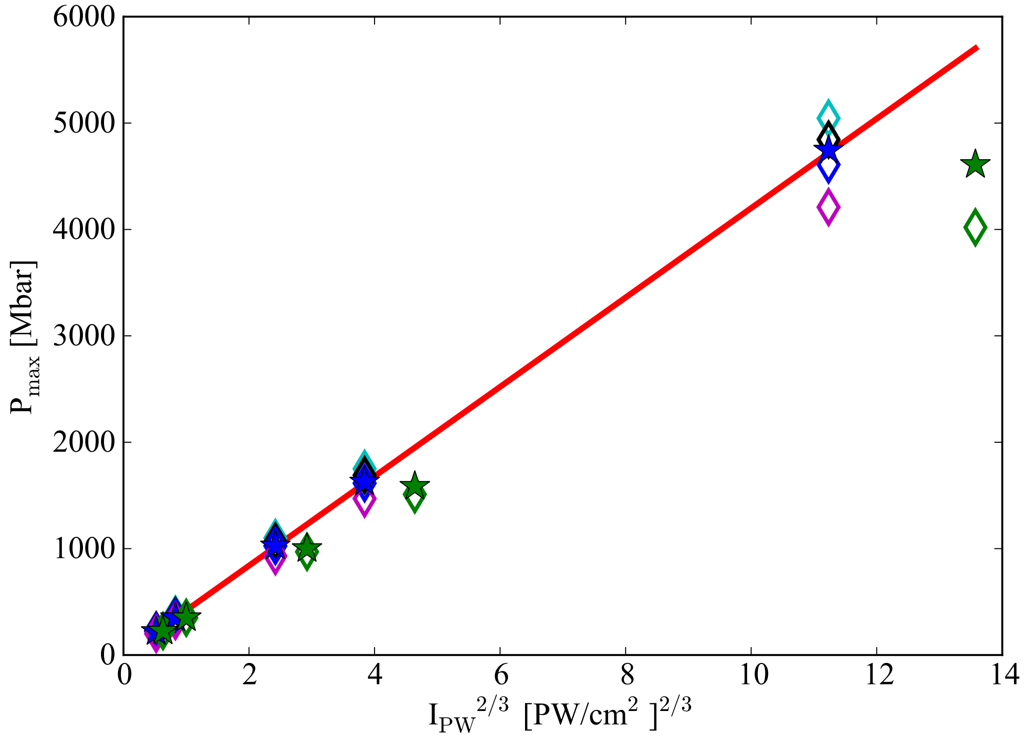

**Figure 5.8: Comparison of peak pressures achieved using Maxwellian and monoenergetic beams (with and without thermal conduction) with the prediction of Eq. 5.4 for a constant density of 10 g/cm$^3$. Marked by diamonds are the peak pressures achieved using 20 keV (pink), 30 keV (blue), 40 keV (black) and 50 keV (cyan) Maxwellian beams and using a 30 keV monoenergetic beam (green) with thermal conduction. Marked by stars are the peak pressures achieved using 30 keV Maxwellian (blue) and monoenergetic (green) beams without thermal conduction. The prediction of Eq. 5.4 is given by the solid red line.**

getic beam results without thermal conduction should best match Eq. 5.4. The Maxwellian results show excellent agreement but the monoenergetic results are consistently lower than expected. This difference is easily explained by the fact that a monoenergetic beam at 30 keV is more collisional than a Maxwellian with a thermal temperature of 30 keV. As a result, it is found that 30% of the energy in the monoenergetic simulations was lost to the pre-plasma, which reduces the on-target intensity. If this is taken into account, excellent agreement with Eq. 5.4 can be recovered.

Increasing the temperature of a Maxwellian increases the spatial extent of the heating profile it produces. Thus, by comparing the peak pressures achieved using Maxwellians of different temperatures, the independence of Eq. 5.4 from the degree of this energy spread can be tested. It is clear from Fig. 5.8 that there is a spread in peak pressure at a given intensity with colder beams giving slightly lower pressures and hotter beams giving slightly higher pressures. This difference can also be explained by reduced on-target intensity for colder populations as losses to the pre-plasma increase with decreasing temperature. These results show that the peak pressure is indeed only a weak function of the spatial extent of the heating profile.

The role of thermal conduction may only be judged in relative terms from these simulations. One might expect thermal conduction to enhance the shock pressure by carrying energy down the negative temperature gradient produced at the target-pre-plasma interface. However, comparing the results for 30 keV Maxwellian (blue) and monoenergetic (green) beams with thermal conduction (diamonds) and without (stars), it is clear that including thermal conduction has reduced the peak pressure. This is because the domain equates to a zero-temperature sink (see Section 3.5.4). This boundary condition is non-physical and it allows an artificially large amount of heat to be conducted out of the system. The difference in peak pressure is more noticeable at higher intensities where hotter and steeper temperature profiles are produced, but even then this error is $\lesssim$10%. Since even this small error negates any pressure enhancement one might expect from thermal conduction, thermal conduction can be quantified as a correction to Eq. 5.4 on the order of a few percent at most.

The validity of the hybrid approximation is assessed using the ratio of the number density of fast electrons to the number density of background electrons. In the majority of the simulations presented in Fig. 5.8, this ratio is comfortably below the 1% level and the hybrid approximation is valid. For example, when heating using a 30 keV monoenergetic beam at an intensity of 1 PW/cm$^2$ the ratio reaches its maximum value of 0.3% in the injection region. The case of heating using a 30 keV monoenergetic beam with an intensity of 50 PW/cm$^2$ (the right most green data points

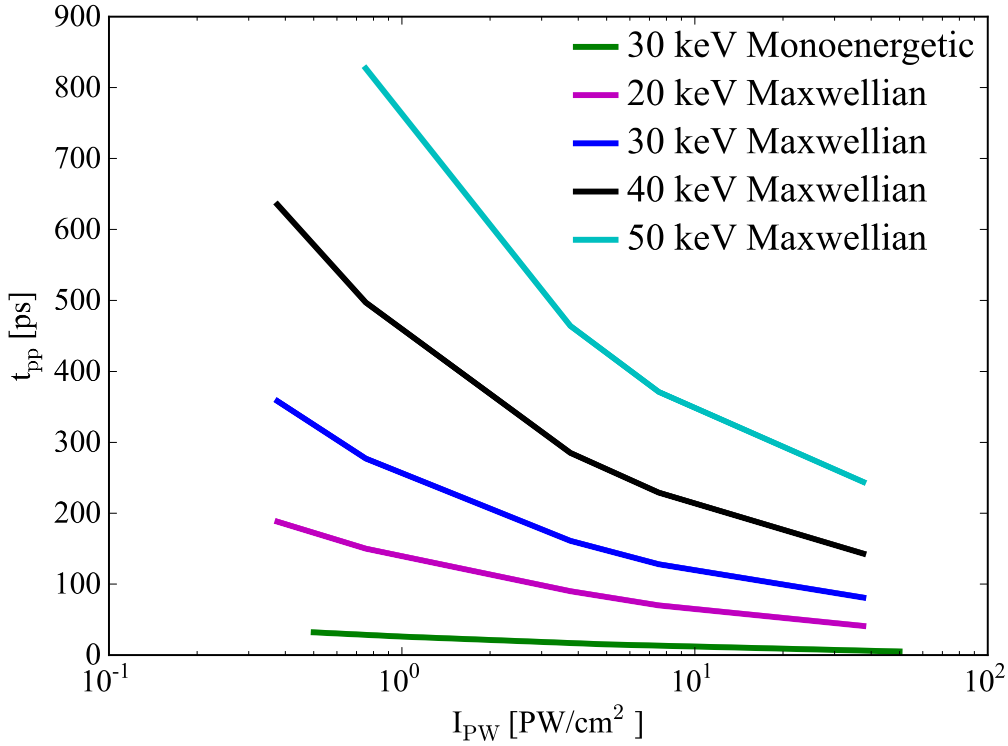

**Figure 5.9: Comparison of time taken to reach peak pressure using 20 keV (pink), 30 keV (blue), 40 keV (black) and 50 keV (cyan) Maxwellian beams and using a 30 keV monoenergetic beam (green) of various intensities.**

in Fig. 5.8) puts the most pressure on the validity of the hybrid approximation. In this case the ratio does briefly reach the 10% level in the injection region during an initial transient period of a few tens of picoseconds but then drops to the level of a few percent. The validity of the hybrid approximation becomes questionable at ratios around 10% but, since this is a transient maximum that is spatially localised to the injection region, the conclusions that have been drawn are expected to hold. Thus, overall the hybrid approximation is deemed to be valid in this suite of simulations.

Figure 5.9 compares the time taken to achieve peak pressure, $t_{pp}$, as a function of intensity using a 30 keV monoenergetic beam and a suite of Maxwellian beams of different temperatures. The time taken to achieve peak pressure increases with increasing fast electron temperature and decreasing intensity, taking $\sim$100$-$800 ps in the ranges 20$-$50 keV and 1$-$10 PW/cm$^2$. The

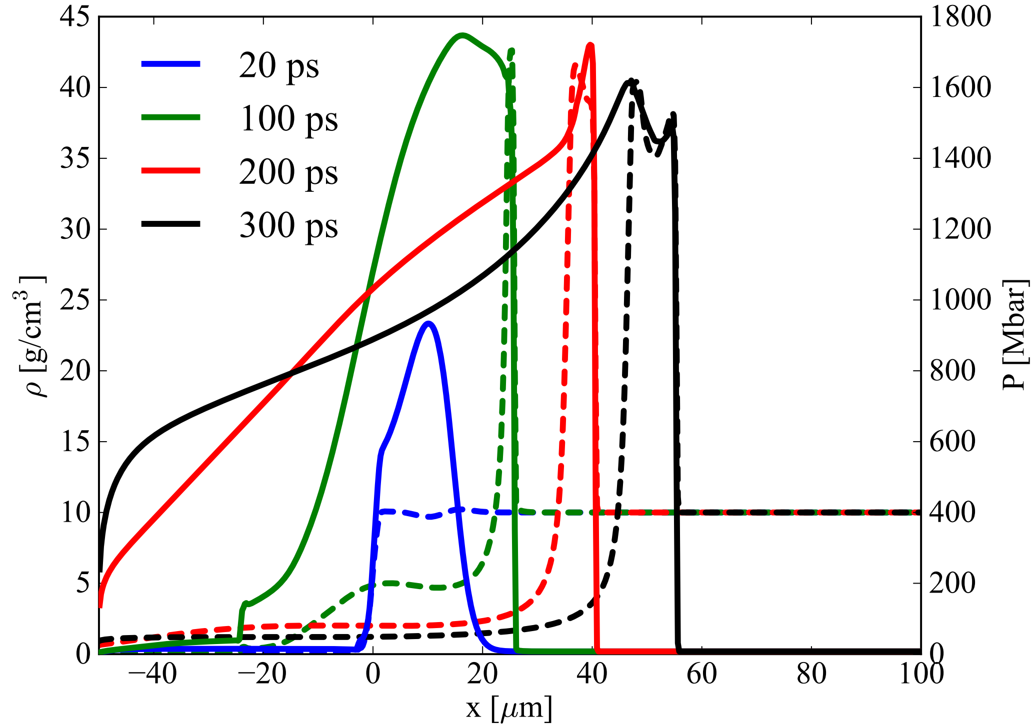

**Figure 5.10: Time evolution of pressure (solid) and density (dashed) profiles of the plasma subject to a monoenergetic electron beam with a temperature of 100 keV and an intensity of 10 PW/cm$^2$.**

time taken is also significantly longer using Maxwellian rather than monoenergetic beams. For example, a 30 keV Maxwellian beam takes approximately ten times longer than a 30 keV monoenergetic beam. The spatial extent of the heating profile produced and the distance travelled by the shock wave as it grows to its peak pressure increase with fast electron temperature. The shock wave travels ∼70 $\mu$m for a temperature of 50 keV. Thus, while the peak pressure is independent of the spatial extent of the heating profile, the areal density of the target plasma must be sufficient to encompass it, and allow the shock wave to develop. This is exemplified by Figs. 5.10 and 5.11. Figure 5.10 shows the pressure and density profiles produced by a 100 keV monoenergetic beam approximated by a Gaussian with a FWHM of 7 keV at an intensity of 10 PW/cm$^2$. The pressure profile is still tight, albeit broader than in Fig. 5.3 because of the greater range in mean-

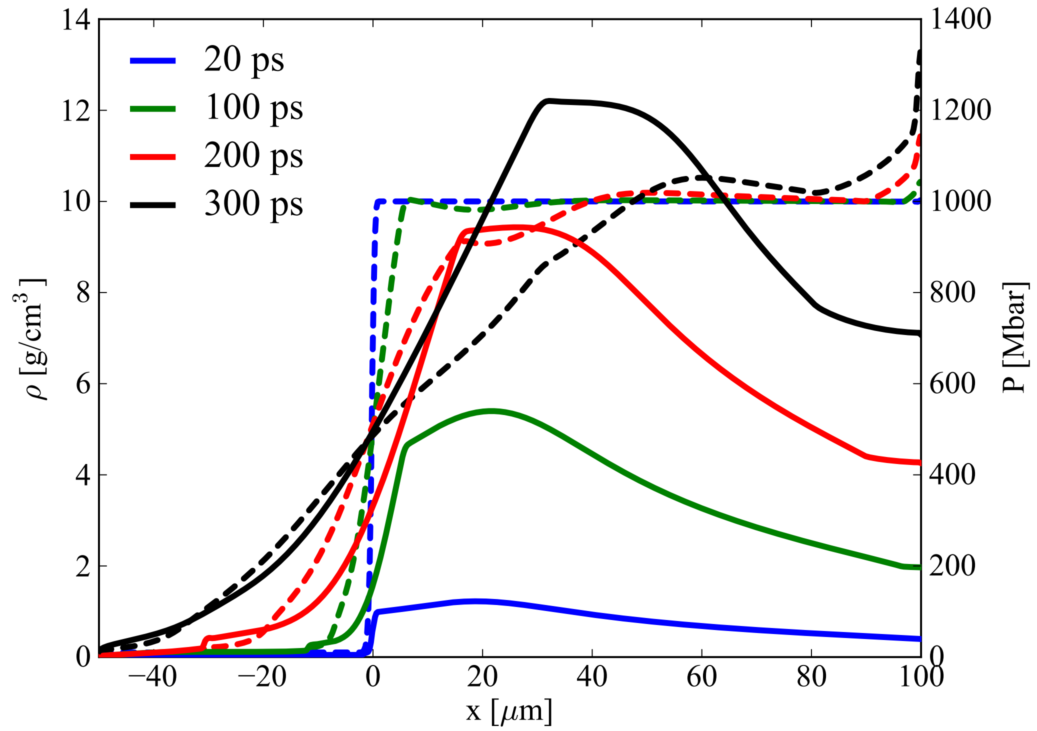

**Figure 5.11: Time evolution of power density deposition (solid) and density (dashed) profiles of the plasma subject to a Maxwellian electron beam with a thermal temperature of 100 keV with an intensity of 10 PW/cm$^2$.**

free-paths in the distribution. A peak pressure of 1920 Mbars is reached after 66 ps, which is close to the 1950 Mbar predicted by Eq. 5.4 and a rapidly developing forward going shock wave can be seen in the density profiles. Figure 5.11 shows the equivalent profiles for a 10 PW/cm$^2$, 100 keV Maxwellian beam. The greater range of electrons in this hotter distribution produces near-uniform heating of the whole plasma compared to Fig. 5.5, which creates only a gentle pressure gradient and fails to develop a shock wave in the simulated length of plasma.

## 5.6 The Potential Role of Radiation Transport

The role of radiation transport, had it been included in the model, is assessed by comparing the power density of deposition by fast electron transport with the theoretical power density emission via Bremsstrahlung radiation, and by considering the optical depth of the plasma.

The power density radiated by a Hydrogen plasma via Bremsstrahlung radiation is given by [68],

$$\mathcal{P}_{\text{Br}} = 1.69 \times 10^{-32} Z^2 n_i n_e T_e^{1/2} \quad \text{W/cm}^3, \tag{5.5}$$

where the background plasma ion number density, $n_i$ and electron number density, $n_e$ are in units of per cubic centimetre, the background electron temperature, $T_e$ is in units of eV and $Z$ is the charge state of the background plasma ions. The optical depth of Bremsstrahlung radiation is given by [68],

$$\tau = 5.0 \times 10^{-38} n_e n_i Z^2 \bar{g} L T_b^{-7/2}, \tag{5.6}$$

where $\bar{g}$ is an average Gaunt factor, $T_b$ is the background plasma temperature and $L$ is the physical path length (taken to be 100 $\mu$m as this is the length of the plasma in these simulations). The transmittance of the plasma is given by [68],

$$T = \exp(-\tau). \tag{5.7}$$

The spatial distributions of the power density deposited by the fast electron population $P_{\text{Dep}}$, the theoretical power density that would be emitted via Bremsstrahlung radiation, $P_{\text{Br}}$, and the transmittance, $T$, of the plasma are calculated for all of the simulations presented in this chapter. Representative examples are given in Fig. 5.12 for the simulations presented in Figs. 5.3 to 5.6. The left hand column corresponds to irradiation by a 1 PW/cm$^2$ 30 keV monoenergetic beam (considered in Fig. 5.3) and the right hand column corresponds to a 1 PW/cm$^2$ 30 keV Maxwellian beam (considered in Fig. 5.5). The rows correspond to early (20 ps), mid (500 ps) and late (1000 ps) times in the simulations.

Of primary concern is the energy balance between $P_{\text{Dep}}$ and $P_{\text{Br}}$ in the shock wave as this

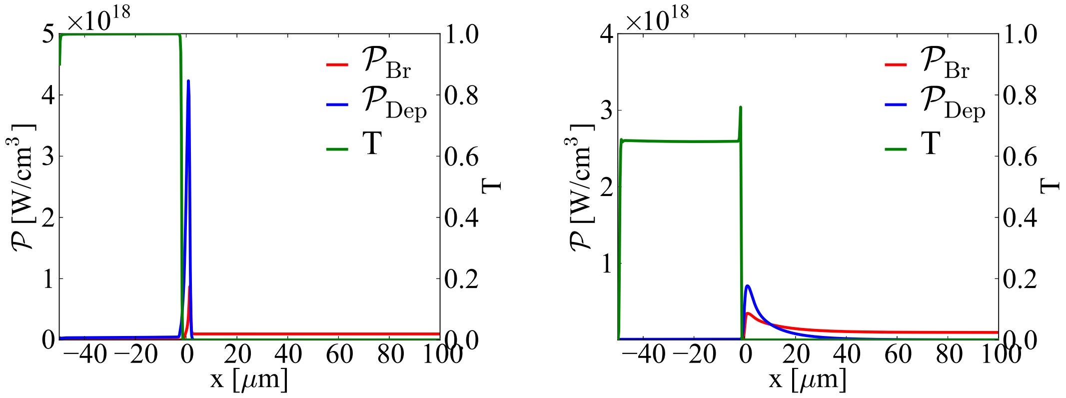

**(a) Monoenergetic - 20 ps**

**(d) Maxwellian - 20 ps**

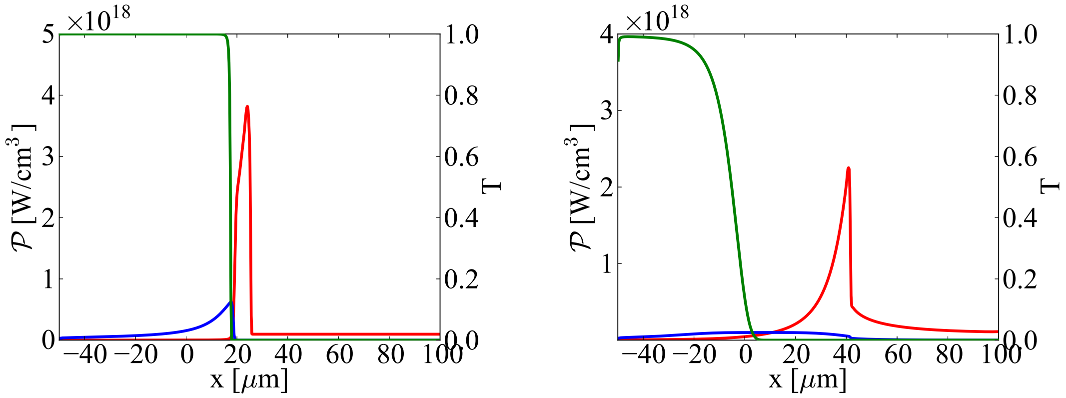

**(b) Monoenergetic - 500 ps**

**(e) Maxwellian - 500 ps**

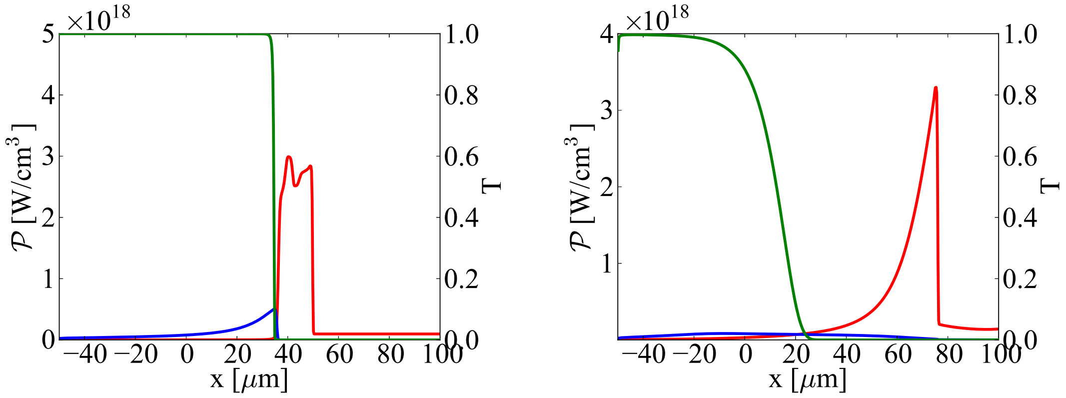

**(c) Monoenergetic - 1000 ps**

**(f) Maxwellian - 1000 ps**

**Figure 5.12: A comparison of the power density deposited by fast electrons (blue), the potential power density emission via Bremsstrahlung radiation (red) had it been included in the model, and the plasma transmittance (green). The left hand column corresponds to irradiation by a 1 PW/cm$^2$ 30 keV monoenergetic beam (considered in Fig. 5.3) and the right hand column corresponds to a 1 PW/cm$^2$ 30 keV Maxwellian beam (considered in Fig. 5.5). The rows correspond to early (20 ps), mid (500 ps) and late (1000 ps) times in the simulations. The high density and relatively low temperature of the shock wave mean that it has an extremely long optical path, and consequently a very low transmittance. Thus, radiation transport is not expected to significantly affect the shock wave structure.**

will directly affect its peak pressure. In all of the cases shown in Fig. 5.12, $P_{\mathrm{Br}}$ is comparable to $P_{\mathrm{Dep}}$ or far exceeds it. However, the high density and relatively low temperature of the shock wave mean that the shock wave has an extremely long optical path, and consequently a very low transmittance. Thus it is argued that had Bremsstrahlung radiation been included it would not have radiated a significant amount of energy from the shock wave and so would not greatly affect the peak pressure that is achieved. As described previously, the simulations with monoenergetic electron populations agree well with the results presented in Ref. 43, where radiation transport was included. This also suggests that radiation transport does not play a significant role in these systems.

In reality, the shock wave will not be propagating through a purely hydrogen plasma as there is likely to be some remaining ablator material (see Section 2.5). The effects of this have not been fully considered but, provided that the ablator comprises only low-$Z$ material, the conclusions that have been drawn are not expected to be affected. In direct drive schemes, the ablator is typically a low-$Z$ material such as plastic.

## 5.7 Summary

It has been shown that having a fast electron population with an extended energy distribution does not diminish the conclusions reached in Ref. 43, where monoenergetic beams were considered. It is found that the peak pressure is independent of the exact nature of the energy distribution and the heating profile it produces, if the heating profile is well behaved, has a single peak, and has a spatial extent that can be well described by a spatial scale length. Peak pressures of a few hundred Mbars to over 1 Gbar are achieved using fast electron intensities of $1-10$ PW/cm$^2$ in a uniform DT plasma at 10 g/cm$^3$.

Maxwellian populations give a greater driver-shock power efficiency compared to a monoenergetic beam of the same characteristic temperature ($\sim$19% and $\sim$8% for 30 keV Maxwellian and monoenergetic beams, respectively). The increased efficiency is due to the hotter electrons in the Maxwellian beams having sufficiently long mean-free-paths to continue to deposit energy in the shock front long after the electrons at the thermal energy have become decoupled from it.

It has also been observed that the time taken to achieve the peak pressure is significantly increased by using extended energy distributions, and it increases with increasing fast electron temperature and decreasing intensity, taking 100−800 ps in the ranges 20−50 keV and 1−10 PW/cm$^2$. The distance the shock wave traverses during this time increases with fast electron temperature and is $\sim$70 $\mu$m for a temperature of 50 keV. If the target is sufficiently long, a strong shock can be driven with a peak pressure that compares well against analytic theory. On the other hand, as the distance travelled by the shock wave becomes comparable to the target size the shock is not able to fully develop. Thus, if one wishes to exploit fast electrons in an ignition scheme one must consider, relative to the fast electron temperature, the spatial and temporal scales required for the shock wave to fully develop; both of which already have requirements placed on them by the ignition scheme. The time taken for the shock wave to develop is investigated further in Chapter 6, where a scaling relation for the characteristic time scale of the early explosive phase of shock wave formation is obtained and tested using the hybrid model.

The current study is limited to 1D. This necessarily precludes any transverse beam-plasma instabilities that would be present in a 2D or 3D system and which may influence energy deposition and shock generation (see Section 3.4 of Ref. 103). Furthermore, shock ignition relies on a spherically symmetric convergence of the shock waves to enhance their strength. This geometric effect is missing from this planar investigation. The interplay between the increase in the time to peak pressure due to extended energy distributions and the enhancement of the shock due to convergence should be studied but is beyond the capabilities of the hybrid model.

# Chapter 6

# On the Characteristic Time Scale of Explosive Shock Wave Generation

As of May 2014, the work detailed in this chapter has been submitted to Physics of Plasmas: T. E. Fox, A. P. L. Robinson, H. Schmitz, J. Pasley, *"Characterising the Acceleration Phase of Blast Wave Formation",* submitted to Physics of Plasmas.

## 6.1 Introduction

In Chapter 5, it was found that if one wishes to use fast electron populations to drive strong shock waves, one needs to consider the time it takes for the shock wave to develop. The structure of a strong shock wave formed by an intense explosion in a fluid has a self-similar solution [104, 105] that has been applied to diverse scenarios including chemical and nuclear explosions [106], supernova evolution [107] and expanding laser-plasmas [108]. The well known scaling relation for the position of the shock at late times can be derived using dimensional analysis without reference to the self-similar solution. From this relation it is clear that both the scaling relation and the self-similar solution describe only the phase of evolution in which the shock is gradually decelerating.

The early explosive phase is not described by the Sedov-Taylor solution.

A characteristic time for the evolution of a blast wave solution from a finite region of internal energy has been identified via dimensional analysis [17, 109]. By the nature of dimensional analysis, this characteristic time can offer several interpretations but will always have the same dependence on physical parameters. Herein it is proposed that, rather than simply being a characteristic time, it may be interpreted as the definitive time taken for an initial, localised source of internal energy to drive a blast wave containing its maximum amount of kinetic energy. Such a measure can be of some utility if one is interested in the timescale of the initial acceleration phase of blast wave formation. For example, in some aspects of laser fusion and laser-driven hydrodynamics one may be more interested in the early acceleration phase rather than the Sedov-Taylor phase that sets in much later.

In this chapter, a study is made of the formation of Sedov-Taylor-like blast waves due to a localised high pressure region in an otherwise uniform, cold fluid. A scaling relation for the time taken for a forming blast wave to contain its maximum kinetic energy is presented and the resultant blast wave is compared with the Sedov-Taylor self-similar solution. This scaling relation is confirmed using the hydrodynamic part of the hybrid model and an attempt has been made to apply it to fast electron driven shock wave formation. This investigation and the difficulties encountered when using fast electron populations have revealed the key parameters that need to be considered if one wishes to use fast electrons to drive shock wave formation.

## 6.2 Theory

A spatially localised heated region within an otherwise uniform cold fluid will expand and drive hydrodynamic waves into the surrounding fluid. When the pressure difference between the hot and cold regions is significant, shock waves will be generated. The thermal energy of the heated region is converted into kinetic energy as the shock wave develops. The Sedov-Taylor self-similar solution describes the evolution of an established blast wave and predicts the final energy partition between thermal and kinetic energy, but does not describe the formation of the blast wave when the fluid is being accelerated by the initial thermal pressure. This can be seen from the Sedov-Taylor relation for the position of the shock front:

$$R_s \propto \left(\frac{E}{\rho}\right)^{1/5} t^{2/5}, \tag{6.1}$$

where $E$ is the thermal energy in the initial hotspot, and $\rho$ is the ambient density. This can be physically interpreted by differentiating Eq. 6.1 to obtain, $\dot{R}_s \propto t^{-3/5}$, i.e. the shock front velocity is falling with time. According to the Rankine-Hugoniot relations, this means that the shock is accelerating the fluid less and less.

The self-similar structure of the blast wave shown in Fig. 6.1 can also be considered. The distance between the origin and the shock front is parameterised by the dimensionless parameter $\xi = r/R_s$ where $r$ is radial coordinate. The solution is calculated in a spherical geometry for $\gamma = 5/3$ and by looking for a self-similar solution of the form:

$$G(\xi) = \frac{\rho}{\rho_0}, \tag{6.2a}$$

$$U(\xi) = \frac{1}{A}\frac{ut}{r}, \tag{6.2b}$$

and

$$Z(\xi) = \frac{1}{B}\frac{c_s^2 t^2}{r^2}, \tag{6.2c}$$

where $\rho_0$ and $\rho$ are the pre- and post-shock densities, respectively, $u$ is the post-shock fluid velocity, $t$ is time and $A$ and $B$ are dimensionless constants chosen to simplify the solutions. Of particular interest is the red curve as this represents the fluid velocity. It shows that the fluid velocity nearly linearly decreases from the shock front to the origin. Thus, the picture that one has

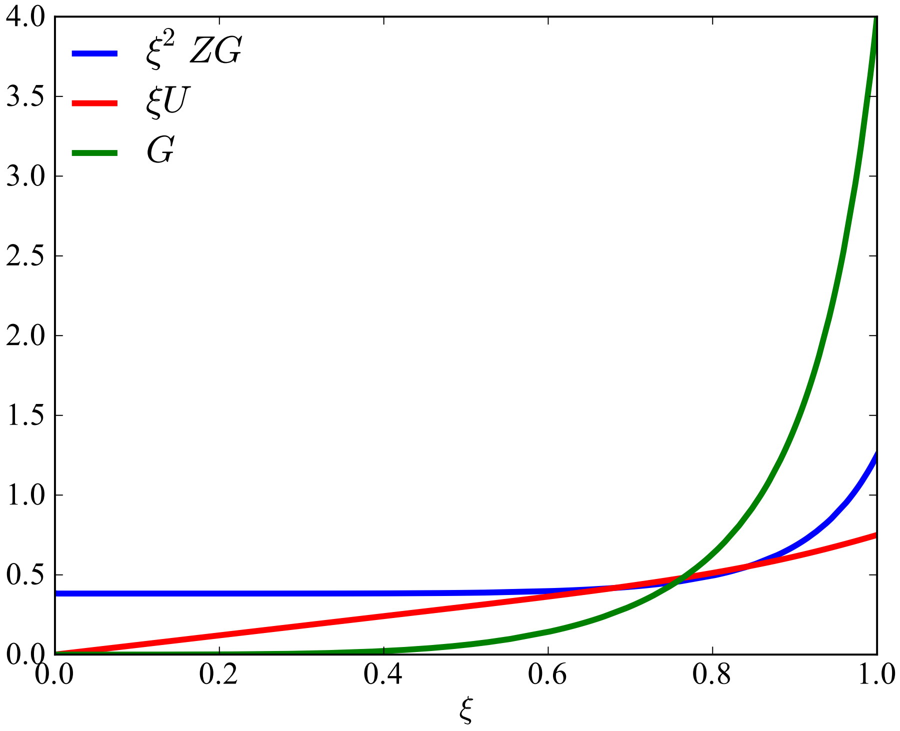

**Figure 6.1: The self-similar structure of a Sedov-Taylor blast wave in a spherical geometry with $\gamma = 5/3$. The spatial size of the blast wave is parameterised by the dimensionless parameter $\xi = r/R_s$ where $r$ is radial coordinate and $R_s$ is the position of the shock front. The curves represent the thermal pressure (blue), velocity (red) and density (green) profiles within the shock. Of particular interest is the fact that the fluid velocity decreases almost linearly from the shock front to the origin because then a decelerating shock front means that all of the fluid behind the shock front is also decelerating.**

is one of a slowing shock front with the fluid directly behind the shock front slowing and, by extension, so is all of the material back to the origin. Thus, the Sedov-Taylor blast wave solution is that of a decelerating system and can only describe the behaviour at late time. It does not describe the initial explosive or acceleration phase.

Now let us consider applying dimensional analysis to the acceleration phase. Let the duration of this acceleration phase be $t_{\mathrm{KE}}$, that is, the time taken for the maximum possible conversion from thermal to kinetic energy to be achieved. This is considered to depend on the characteristic spatial size $R_h$ of the heated region, the initial internal energy $E_h$ contained within the region and the ambient density of the cold fluid $\rho_0$. Using these parameters one can construct a dimensionless parameter $\eta$. Then the time taken for the forming blast wave to contain its maximum kinetic energy obeys the scaling relation:

$$t_{\mathrm{KE}} = \eta\sqrt{\frac{\rho_0}{E_h}}R_h^{5/2}. \tag{6.3}$$

Equation 6.3 is necessarily of the same form as the Sedov-Taylor scaling relation but its application, or physical interpretation, is fundamentally different. This scaling relation is validated in Section. 6.3 using a 1D planar hydrodynamic model. In a planar geometry it is meaningful to replace the initial thermal energy $E_h$ with the areal thermal energy $\mathcal{E}_h$. The scaling relation is then:

$$t_{\mathrm{KE}} = \xi\sqrt{\frac{\rho_0}{\mathcal{E}_h}}R_h^{3/2}, \tag{6.4}$$

where $\xi$ is the dimensionless parameter in the planar case.

## 6.3 Hydrodynamic Modelling

The scaling relation in Eq. 6.4 is confirmed using the hydrodynamic part of the hybrid model. The simulations are initialised with a uniform fluid density $\rho_0$, containing a Gaussian shaped heated layer at its centre. The characteristic width of the heated layer is $R_h$ and is equal to its full-width-at-half-maximum (FWHM). This width of fluid contains the initial areal thermal energy $\mathcal{E}_h$. Shock wave formation in a cold plasma is approximated by setting the ratio of the maximum and minimum initial areal energy to be at least $\sim 10^{13}$ in all simulations. An ideal gas is assumed with $\gamma = 5/3$, unless otherwise stated.

Convergence testing led to the choice of simulation parameters. A spatial resolution of $R_h^{\mathrm{min}}/\Delta x = 25$ was used in all simulations, where $R_h^{\mathrm{min}}$ is the minimum characteristic width of the heated layer used in the investigation. Doubling the resolution changed the measured $t_{\mathrm{KE}}$

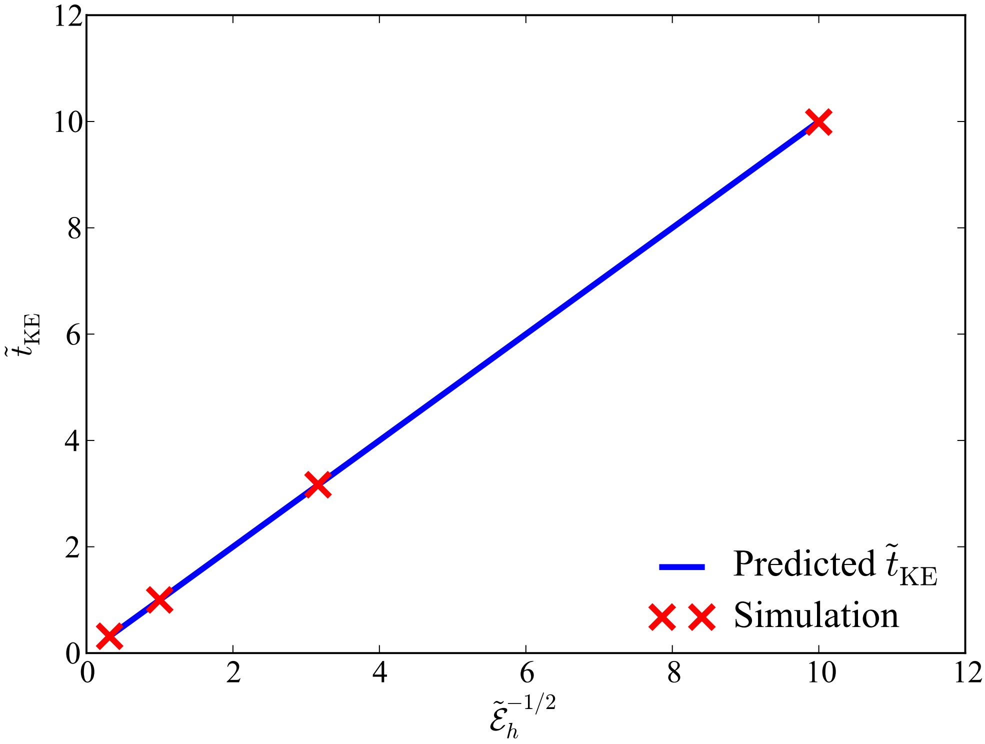

**Figure 6.2: The scaling of $\tilde{t}_{\mathrm{KE}}$ with $\tilde{\mathcal{E}}_h$, as predicted by Eq. 6.4 is confirmed by varying $\tilde{\mathcal{E}}_h$ while keeping $\tilde{\rho}_0$ and $\tilde{R}_h$ constant. The simulation results (red crosses) show excellent agreement with predicted scaling of Eq. 6.4 (blue solid).**

by $\sim$1%, and the maximum areal kinetic energy measured by $\sim$0.3%. As long as the time step satisfied the usual hydrodynamic stability condition, the measured values did not vary with temporal resolution.

Figures 6.2 to 6.4 show the measured times taken for the shock wave to develop its maximum amount of areal kinetic energy for a parameter scan of initial conditions. Their excellent agreement with Eq. 6.4 shows that the acceleration phase of blast wave evolution is well characterised. In these figures, $\tilde{t}_{\mathrm{KE}}$, $\tilde{\mathcal{E}}_h$, $\tilde{\rho}_0$ and $\tilde{R}_h$ are dimensionless quantities defined as the ratio of their dimensional equivalents relative to a reference simulation that exists in each parameter scan. The scaling of $\tilde{t}_{\mathrm{KE}}$ with $\tilde{\mathcal{E}}_h$, $\tilde{\rho}_0$ and $\tilde{R}_h$ is confirmed by holding two of the parameters constant while varying the third. In these units, the predicted curves for $\tilde{t}_{\mathrm{KE}}$ are plotted with $\xi = 1$. The arithmetic mean

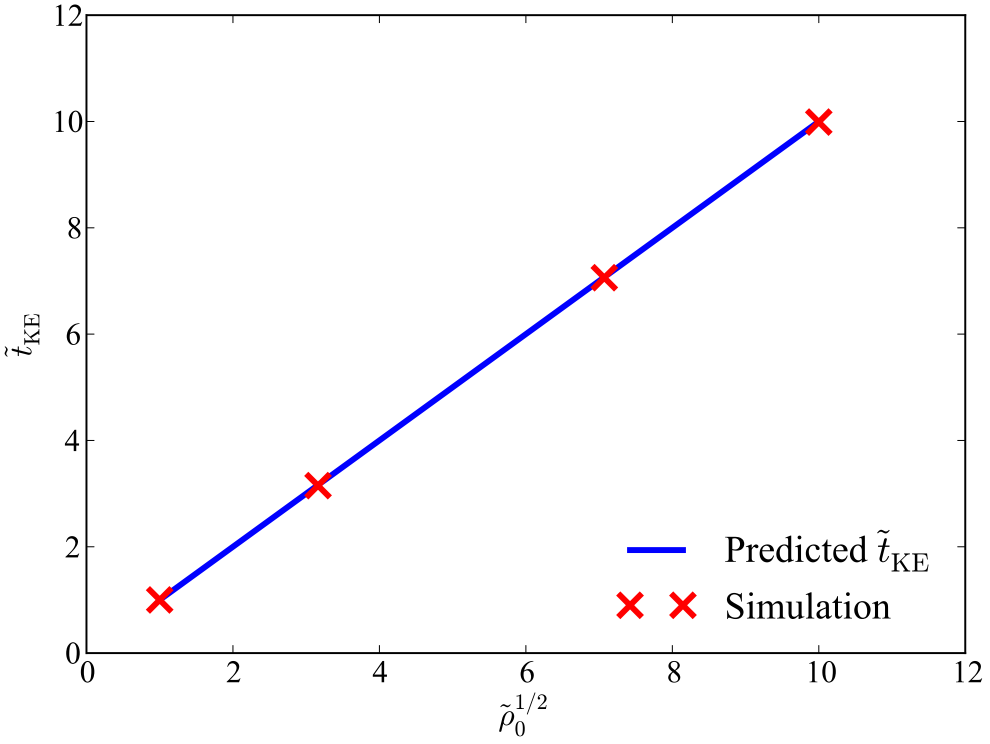

**Figure 6.3: The scaling of $\tilde{t}_{\mathrm{KE}}$ with $\tilde{\rho}_0$, as predicted by Eq. 6.4 is confirmed by varying $\tilde{\rho}_0$ while keeping $\tilde{\mathcal{E}}_h$ and $\tilde{R}_h$ constant. The simulation results (red crosses) show excellent agreement with predicted scaling of Eq. 6.4 (blue solid).**

of the measured scaling parameters is $\bar{\xi} = 0.998$ with a $\sim$2.5% spread between the maximum and minimum measured values of $\xi$.

The history of the conversion of initial areal internal energy $\mathcal{E}_h$ into areal kinetic energy $\mathcal{K}$ is shown in Fig. 6.5. There are two distinct phases in the rate of conversion: a rapid early conversion phase followed by a much more gradual late conversion phase. Looking at Fig. 6.5, one would be inclined to say that the acceleration phase ends at $\sim 0.2 t_{\mathrm{KE}}$. However, the acceleration phase strictly ends at $t_{\mathrm{KE}}$, but this time lies well into the late conversion phase. The difference is that, although 98% of the total conversion has occurred by $0.17 t_{\mathrm{KE}}$, the remaining 2% of the total conversion takes considerably longer. The scaling relations in Eq. 6.4 still hold if one takes the measurement after 95%, 98% and 99% of the total conversion, corresponding to times of $0.09 t_{\mathrm{KE}}$,

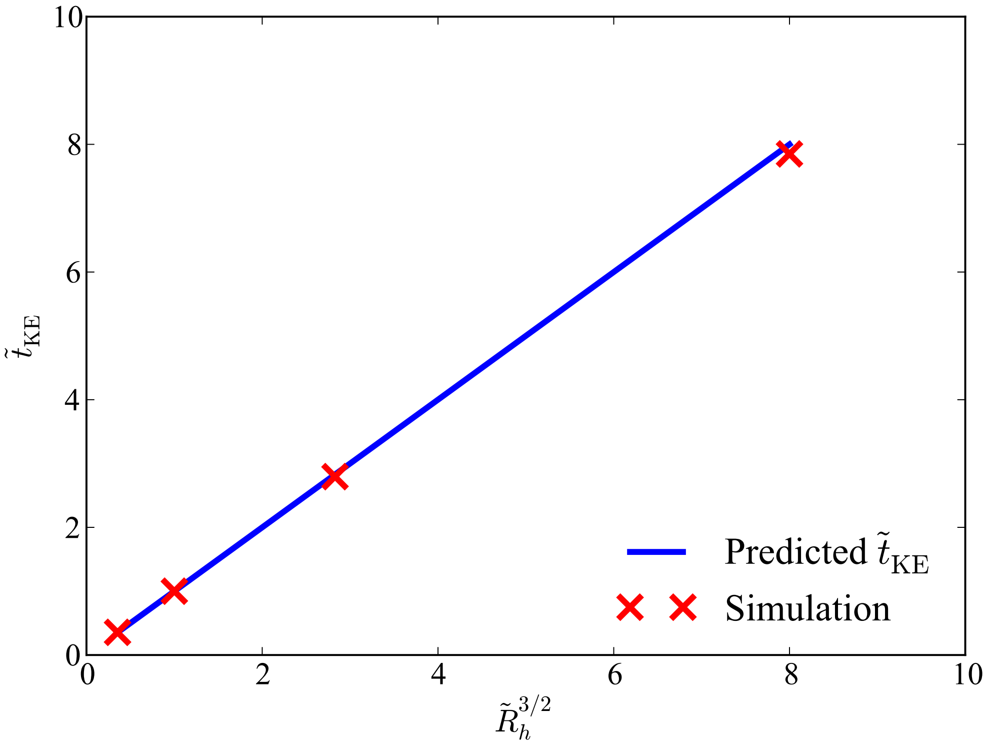

**Figure 6.4: The scaling of $\tilde{t}_{\mathrm{KE}}$ with $\tilde{R}_h$, as predicted by Eq. 6.4 is confirmed by varying $\tilde{R}_h$ while keeping $\tilde{\rho}_0$ and $\tilde{\mathcal{E}}_h$ constant. The simulation results (red crosses) show excellent agreement with predicted scaling of Eq. 6.4 (blue solid).**

$0.17 t_{\mathrm{KE}}$, $0.54 t_{\mathrm{KE}}$, respectively, but with different values of $\xi$.

Figure 6.5 shows that the energy partition within the blast wave is 30% areal kinetic energy and therefore 70% areal thermal energy. This can be compared to the Sedov-Taylor self-similar solution for blast waves in a 1D planar geometry, which predicts a partition of 23% areal kinetic energy and 77% areal thermal energy. These values are obtained by integrating the curves in Fig. 6.6, which is equivalent to Fig. 6.1 but in a planar geometry. The total energy in the blast wave is given by,

$$E \propto \int_0^1 G(\xi) \left( \frac{1}{\gamma(\gamma-1)} Z(\xi) + \frac{1}{2} U(\xi)^2 \right) \xi^2 \mathrm{d}\xi \tag{6.5}$$

where the first term in the integral is thermal energy term and the second is the kinetic energy term.

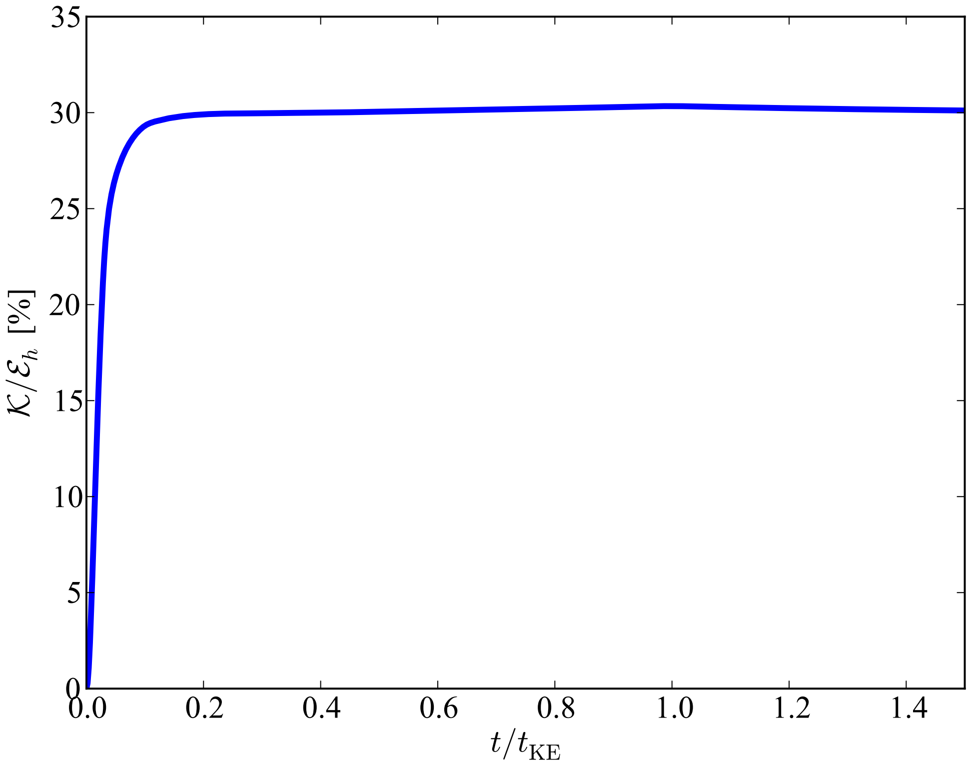

**Figure 6.5: Evolution of the energy partition within the blast wave during its formation. The fraction of initial areal internal energy converted to areal kinetic energy is plotted as a function of time taken to achieve maximum conversion.**

The constant of proportionality contains constant factors related to the geometry. The difference between the simulations and the theory, as well as the late conversion phase evolution seen in Fig. 6.5, are due to the simulated blast wave not being exactly self-similar. This non-adherence to self-similarity is expected due to the initial conditions and has been observed in studies of supernova remnants [109–112]. These studies report on the observance of reverse shocks and transient waves travelling back and forth along the blast wave profile as they reflect off each other at the origin and off the blast wave front. Eventually these will dissipate, allowing the blast wave to assume a self-similar form, however this can take a significant amount of time [109, 113]. Such transient waves exist for the duration of our simulations and, according to the equipartition theorem, should push the system closer to an equal partition of energy between thermal and kinetic

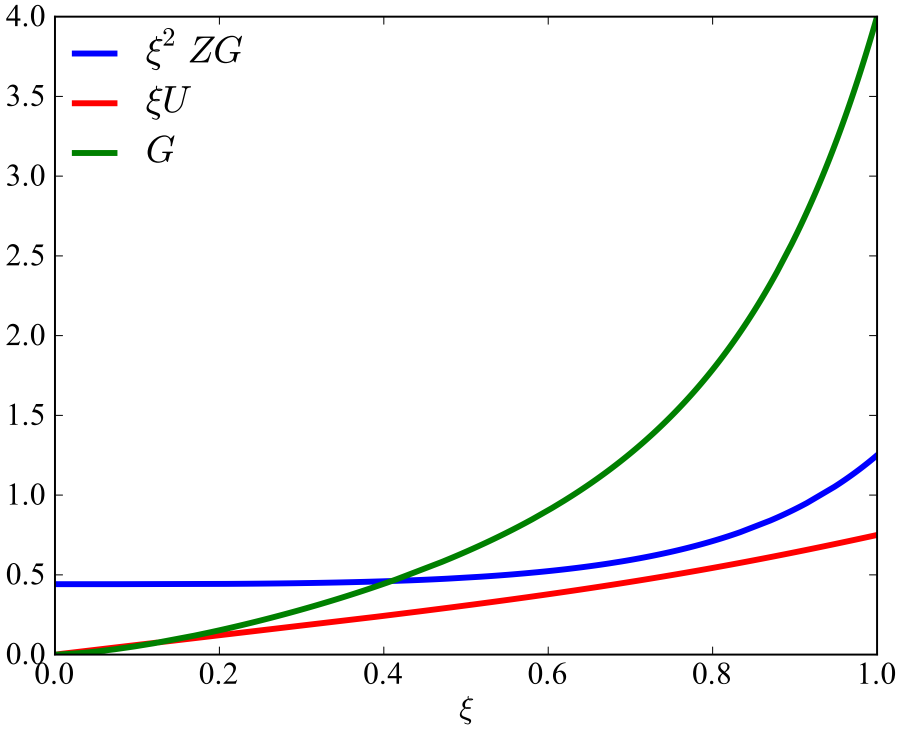

**Figure 6.6: The self-similar structure of a Sedov-Taylor blast wave in a planar geometry with $\gamma = 5/3$. The spatial size of the blast wave is parameterised by the dimensionless parameter $\xi = r/R_s$ where $r$ is radial coordinate and $R_s$ is the position of the shock front. The curves represent the thermal pressure (blue), velocity (red) and density (green) profiles within the shock.**

energy, as observed. The spatial resolution was doubled but the same features are present, and increasing the resolution did not noticeably alter the kinetic energy conversion history. Changing the adiabatic constant to $\gamma = 7/5$ yields a 76% to 24% partition between thermal and kinetic energy, respectively, which is also in relatively good agreement with the self-similar solution which predicts a partition 82% and 18% between thermal and kinetic energy, respectively.

## 6.4 Application to Fast Electron Driven Shock Wave Formation

It has been demonstrated that the time taken for a localised heated region within an otherwise uniform cold fluid to generate a shock containing its maximum kinetic energy is dependent on the size of the heated region, i.e. $t_{\mathrm{KE}} \propto R_h^{3/2}$. A qualitatively similar conclusion was drawn in Chapter 5 which, in part, concerns the time taken for fast electron driven shock waves to fully develop when the fast electrons are continuously injected. This time was defined as the time taken for the shock wave to reach the peak pressure. It was concluded that the scale length of the deposition profile greatly affects this time. In this section, the applicability of the scaling relation, $t_{\mathrm{KE}} \propto R_h^{3/2}$ to the case of a heated region created in a uniform target using a relatively short period of hot electron injection is investigated. The width of the heated region is changed by varying the hot electron temperature.

The simulations are initialised as shown in Fig. 5.2 but with a 10 $\mu$m pre-plasma. The full Maxwellian distribution of hot electrons is injected for a period of 10 ps. Afterwards, the system evolves hydrodynamically in response to the generated pressure profile. Measurements of $R_h$ and $\mathcal{E}_h$ are taken at the time of peak pressure, which is invariably at 10 ps because the fast electrons rapidly thermalise. The width of the heated region, $R_h$ is defined as the FWHM of the pressure profile at the time of peak pressure. For Eq. 6.4 to apply, this assumes that the plasma has not moved by this time and that the total energy density in the $R_h$ region is dominated by internal energy density. This is found to be true with only 2% of the total energy in the $R_h$ region being directed kinetic energy when the coldest electron populations are used. This reduces to just 0.1% for the hottest populations.

Figure 6.7 shows the measured values of $R_h$ and $t_{\mathrm{KE}}$ from simulations using fast electron temperatures of $10-40$ keV in increments of 5 keV. Equation 6.4 predicts that $R_h \propto t_{\mathrm{KE}}^{2/3}$ so a linear fit to the simulation data has also been plotted to make it clear that the results follow a curve

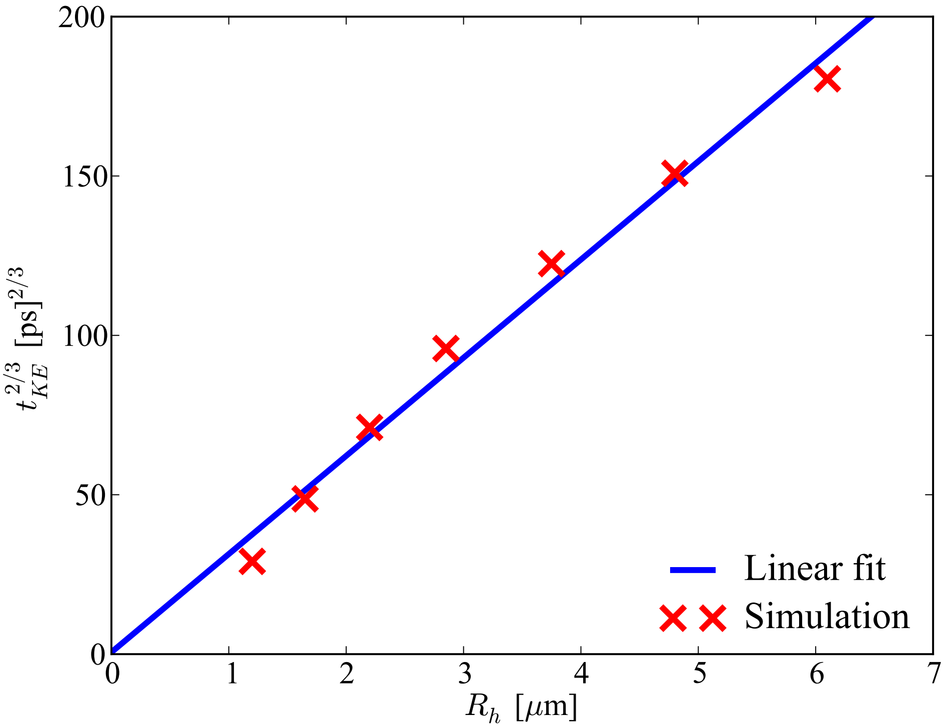

**Figure 6.7: Equation 6.4 predicts that $R_h \propto t_{\mathrm{KE}}^{2/3}$. However, the results from a series of hybrid simulations (red crosses), in which a short period of fast electron energy deposition was used to drive shock wave formation, do not follow this scaling relation. The width of the heated region was calculated as the FWHM of the pressure profile at the time of peak pressure. A linear fit to the data points (blue line) is plotted to emphasise the point that a linear scaling is not followed.**

rather than a straight line. Improving the spatial resolution by a factor of five does not alter this trend. At the best resolution, the smallest measured $R_h$ is resolved by 25 points. This is adequate to resolve the sharp peak in the deposition profile one expects to be produced at the surface of the step-like target and to give smoothly varying profiles elsewhere. Furthermore, the resolution is sufficient to resolve the range of 10 keV electrons with $\sim$10 points, and increasing numbers of points with increasing temperature. Thus, one can be confident that a reasonable account is made of the deposition profiles produced by the fast electron populations used in this study.

The deviation of the numerical results from a linear relationship can be explained by a combi-

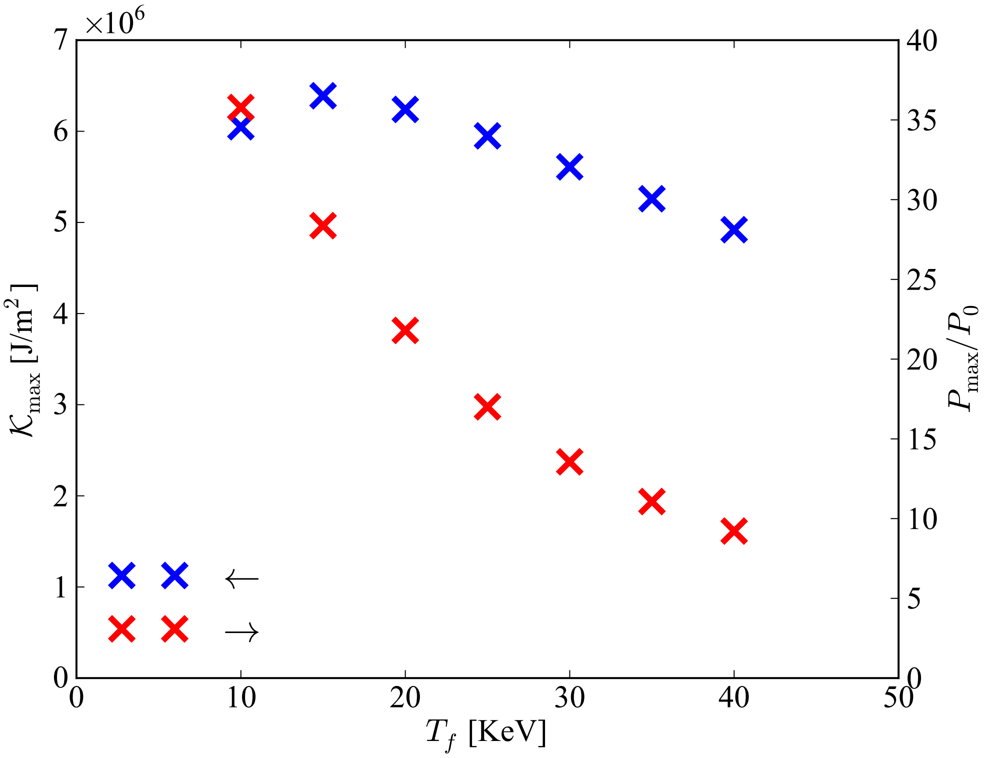

**Figure 6.8: The maximum areal kinetic energy (blue) and the ratio of the peak pressure to the initial pressure in the dense plasma (red) both show a general decrease with fast electron temperature. The drop in the pressure ratio is particularly important because a lower pressure ratio will drive weaker shocks which, in turn, will affect the maximum areal kinetic energy that will be developed and the time taken for it to be reached.**

nation of systematic differences between the simulations. First, it is extremely difficult to control all of the parameters in Eq. 6.4 between simulations when creating the heated region using fast electrons. This is because $R_h$ and $\mathcal{E}_h$ both depend on the fast electron distribution function. This results in a general trend of increasing $\mathcal{E}_h$ with increasing $T_f$ and a 13% variation between the maximum and minimum values of $\mathcal{E}_h$.

The crux of the second point is shown in Fig. 6.8 where the ratio of the peak pressure to the initial pressure in the dense plasma $P_{\text{max}}/P_0$ is plotted for each of the simulations. It shows that this ratio falls significantly between using fast electron temperatures of 10 and 40 keV. Furthermore, the ratio has dropped to less than ten in the 40 keV case. This reduced pressure ratio will result in weaker shock generation which will take less time to develop towards a lower peak areal kinetic energy than expected. Hence the simulation results fall away from a linear relationship in Fig. 6.7. Figure 6.8 shows that there is a 30% decrease in the peak areal kinetic energy when using a 40 keV Maxwellian distribution as opposed to a 15 keV Maxwellian distribution.

## 6.5 Summary

The propagation of blast waves and their relaxation to the Sedov-Taylor self-similar solution has received a lot of attention over the decades [107–112, 114]. However, the time scale of the acceleration phase, preceding the Sedov-Taylor phase, has not been explicitly characterised. An understanding of the time taken for a shock wave to develop is of interest when it may be an appreciable fraction of the system time scale. Such a situation exists in inertial confinement fusion where controlled generation of shock waves is of fundamental importance.

A study has been made of the case of blast wave formation resulting from an intense explosion in a uniform medium, and it has been shown that the time taken for the blast wave to contain its maximum kinetic energy is governed by a simple scaling law. The evolution of the kinetic energy conversion consists of two distinct phases. Most of the kinetic energy is generated during the short, early conversion phase which sees the formation of a blast wave modulated by transient waves that take the solution away from self-similarity. The late conversion phase shows a much more gradual evolution in the partition of energy as the system begins to settle into the self-similar solution.

The conclusions of Chapter 5 and Eq. 6.4 in the present chapter both indicate that the time taken for a shock wave to fully develop is dependent on the length scale of the heated region. Unfortunately, it has proven to be difficult to apply the scaling relation to the scenario of heated regions created in uniform targets by fast electron energy deposition. There are interdependencies between the fast electron temperature, $T_f$, the width of the heated region, $R_h$ and the areal internal energy in the heated region, $\mathcal{E}_h$, which make it difficult to control several parameters simultaneously. Most telling, however, was the drop in the pressure ratio $P_{\text{max}}/P_0$ and the corresponding drop in peak areal kinetic energy as the fast electron temperature was increased. This effect needs to be carefully considered when designing shock ignition schemes.

This 1D single-fluid, hydrodynamic study is limited in terms of the physics included but does give an insight into the basic scalings that are invoked during blast wave formation.

# Chapter 7

# The Effect of Density Profile on Shock Wave Formation

## 7.1 Introduction

So far, only step-like density profiles have been considered when attempting to drive strong shock waves using fast electrons. However, it is unreasonable to expect that the density profile of the assembling fuel will be step-like at the time of the ignitor pulse because, by then, the fuel will have been subjected to laser irradiation for a time on the order of ten nanoseconds [21]. Instead, as one looks radially inwards, one can reasonably expect an exponentially increasing pre-plasma density profile with a scale length of a few hundred microns [88, 89]. The density then rises more rapidly into the dense shell. Intuitively one expects this difference in the density profile to affect fast electron energy deposition and subsequent shock wave formation.

In this chapter, the expected density profile is approximated with a comparatively short scale length exponential increase towards a uniform high density region. This exponential target and a comparable step-like target are subjected to fast electron heating for varying lengths of time.

In each case, the target is free to evolve in response to this heating and measurements are made of the maximum forward-going areal kinetic energy that develops and the time taken to reach that maximum value. Target profiles with alternatives to the exponential density ramp are also considered to give additional insight into the way in which changing the density profile modifies the process of shock formation.

## 7.2 Description of the Simulation Design

The range of density profiles that are considered are shown in Fig. 7.1. The profile shown in Fig. 7.1a will be referred to as the step-like target and it is identical to the targets considered in previous chapters but with the low density pre-plasma shortened to 10 $\mu$m in length. The step-like rise to a density of 10 g/cm$^3$ is smoothed out using a tanh function with a scale length of 2 spatial cells to avoid numerical instabilities. The remainder of the 125 $\mu$m domain is at 10 g/cm$^3$. The first 25 $\mu$m of the high density region in this step-like target is then modified to produce the linear (Fig. 7.1b), exponential (Fig. 7.1c) and Gaussian (Fig. 7.1d) targets. Finally, Fig. 7.1e shows a different situation in which the density continuously and linearly increases with distance (the continuously linear target).

Compared to the step-like target, an areal density of 25 mg/cm$^2$ is affected by the shaping of the leading edge in the targets depicted in Figs. 7.1b to 7.1d. This is many times the 1 mg/cm$^2$ range of 20 keV electrons and so will clearly show the effect of profile shaping on the deposition profile. The continuously increasing linear profile has sufficient areal density to contain the fast electron population in the same sized domain as is used in the other cases. Superimposed on the density profiles in Fig. 7.1 are the deposition profiles calculated using the hybrid model and the Solodov model for a 20 keV Maxwellian beam of fast electrons. The Solodov model calculations use the Coulomb logarithm in Eq. 3.56, and scattering is included.

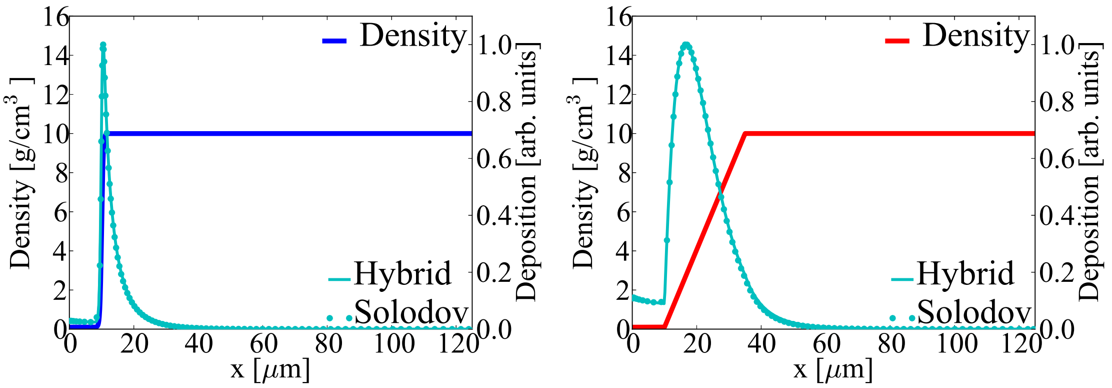

**(a) Step-like** **(b) Linear**

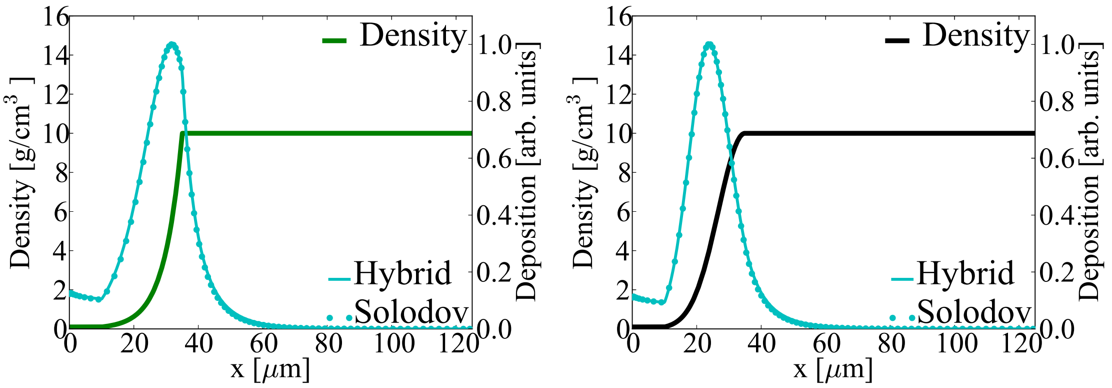

**(c) Exponential** **(d) Gaussian**

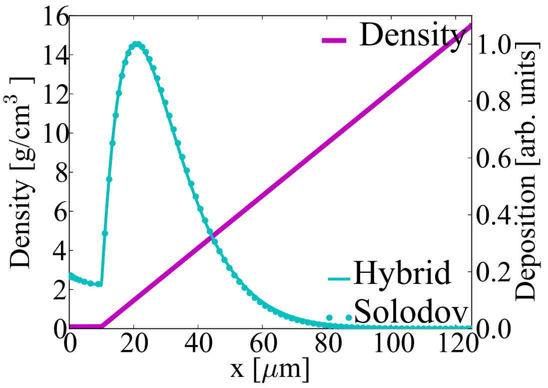

**(e) Continuously linear**

**Figure 7.1: An illustration of the effect the density profile has on the energy deposition profile produced by a 20 keV Maxwellian population of fast electrons injected into a stationary plasma. There is excellent agreement between the deposition profiles produced by the hybrid model (solid cyan line) and the Solodov model (cyan dots).**

Intuitively, one expects shock wave generation to be affected by the differences in the density and energy deposition profiles between the targets shown in Fig. 7.1. To investigate this, a series of simulations will be presented in which a 20 keV Maxwellian population of fast electrons is injected with an intensity of 1 PW/cm$^2$ into each target for heating times of $t_{\text{H}} = 10$, 25, 50, 100, 200 and 400 ps. The target is free to evolve in response to this heating and measurements are made, in each case, of the maximum forward-going areal kinetic energy, $\mathcal{K}_{\text{max}}$, that develops and the time taken to reach that maximum value, $t_{\text{KE}}$.

As in Chapter 5, the background plasma is initialised with a uniform temperature of 1 eV and it is modelled as a fully ionised average DT ion with a mass of 2.5m$_p$ and $Z = 1$. Thermal conduction is included with a flux limiter of 0.05. The fast electrons have a reflective left-hand boundary and an open right-hand boundary, while the reverse is true for the background plasma. The simulation domain has a spatial resolution of $\Delta x = 0.25$ $\mu$m and is 125 $\mu$m long. The momentum resolution is $\Delta p = 0.1 p_{th}$ and the momentum grid extends to 7.5$p_{th}$. Doubling the spatial resolution both reduces the time taken to reach the maximum kinetic energy, and increases the maximum kinetic energy by $\sim$1%. Doubling the momentum resolution reduces the time taken by $\sim$4% and decreases the maximum kinetic energy by $\sim$0.3%. The time step is set to 0.9 of the most stringent CFL condition, which is initially set by advection of the fast electrons. Once the injection of fast electrons has ended, and the fast electrons have thermalised with the background, the time step is set by the hydrodynamic time scale. The fast electron population is represented by 18 harmonics and is beamed with $M = 16$, as this was found to be sufficient in Section 5.3. It is injected over the first micron next to the left hand domain boundary.

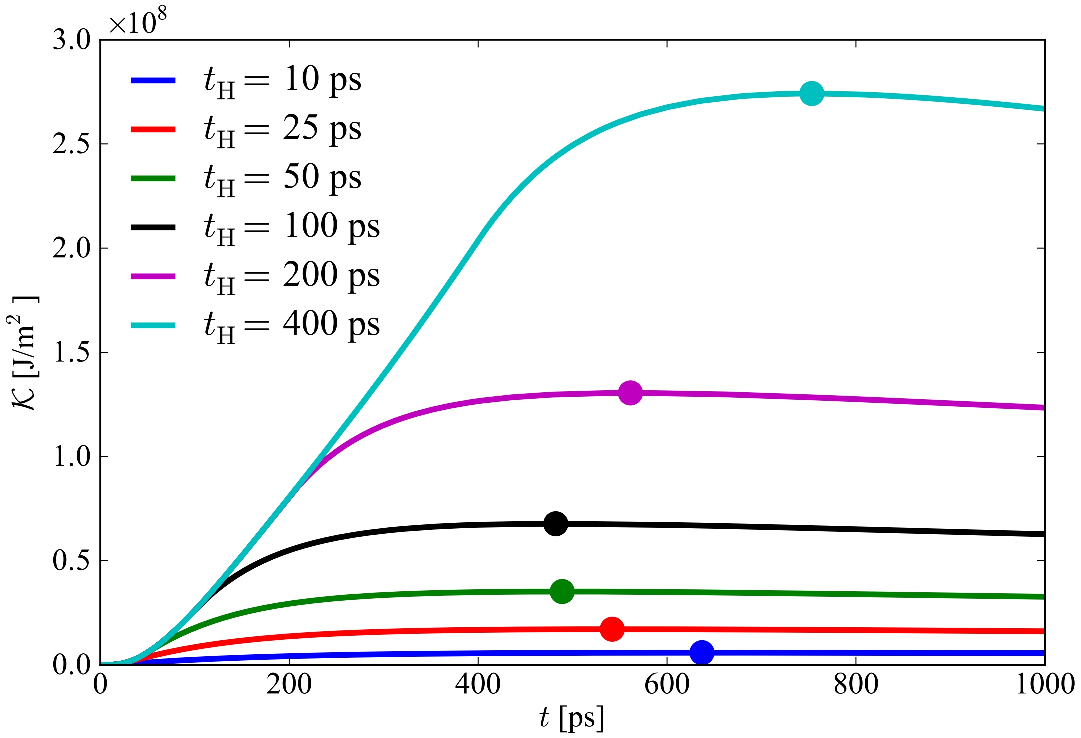

**Figure 7.2: Time evolution of the total forward-going areal kinetic energy generated by heating the step-like target shown in Fig. 7.1a with a 20 keV Maxwellian population of hot electrons with an intensity of 1 PW/cm$^2$, for $t_{\mathrm{H}} = 10$, 25, 50, 100, 200 and 400 ps. The time at which the maximum areal kinetic energy is reached in each case is indicated by a dot.**

## 7.3 The Effect of Shaping the Density Profile

In the first instance, the step-like target is subjected to fast electron heating for $t_{\mathrm{H}} = 10$, 25, 50, 100, 200 and 400 ps. In response to this heating, the plasma expands backwards and a shock wave is driven forward. For each of the heatings times, the time evolution of the total forward-going areal kinetic energy, $\mathcal{K}$ is shown in Fig. 7.2. The time $t_{\mathrm{KE}}$, at which the maximum areal kinetic energy $\mathcal{K}_{\mathrm{max}}$ is reached is also indicated. As one might expect, injecting more energy into the system by increasing $t_{\mathrm{H}}$ results in a higher value of $\mathcal{K}_{\mathrm{max}}$. On the other hand, $t_{\mathrm{KE}}$ does not change monotonically with increasing $t_{\mathrm{H}}$. It first decreases as $t_{\mathrm{H}}$ is increased from 10 ps to 100 ps, but then increases as $t_{\mathrm{H}}$ is increased to 400 ps. It is this behaviour that forms the primary focus of this chapter.

The simulations using the step-like target are repeated with the other target profiles shown in Fig. 7.1, and measurements of $t_{\mathrm{KE}}$ and $\mathcal{K}_{\mathrm{max}}$ are made. Figure 7.3 includes a series of plots which present the measurements of $\mathcal{K}_{\mathrm{max}}$ versus $t_{\mathrm{KE}}$ made for all of the targets after successively longer heating times. The data is presented in this manner to emphasise the path taken by each target through this parameter space. An enlargement of Fig. 7.3f is shown in Fig. 7.4. It is clear from this figure that the time taken to reach the maximum areal kinetic energy depends on the target shaping, and this is most noticeable for shorter heating times. This point will be addressed shortly. First the general trends that appear, irrespective of the target profile, are examined.

As observed in Fig. 7.2, initially increasing the heating time increases $\mathcal{K}_{\mathrm{max}}$ and decreases $t_{\mathrm{KE}}$. This can be explained by noting that if the heating time is shorter than the hydrodynamic response time of the plasma, then the plasma will respond approximately as though it has been instantaneously heated by the total energy being deposited. This is comparable to the scenario of blast wave formation discussed in Chapter 6, where it was found that $t_{\mathrm{KE}}$ decreases with increasing $\mathcal{E}_h$. The current situation differs from that studied in Chapter 6 because it does not have a constant density profile, but the principle is the same. Thus, since the amount of deposited energy increases with $t_{\mathrm{H}}$, if the target is responding as though instantaneously heated one would expect the observed trend of decreasing $t_{\mathrm{KE}}$ with increasing $t_{\mathrm{H}}$. This supposition is first confirmed by looking at the density profiles at the end of the heating phase. For example, Fig. 7.5 shows the density profiles from the step-like and linear cases at the end of the heating time for heating times of 10, 50 and 400 ps. It is obvious that after 10 ps of heating neither profile has evolved greatly from the initial conditions and it is calculated that less than 0.1% of the total background energy density is kinetic energy. This confirms that the heating time is less than the hydrodynamic response time.

Having confirmed that the shorter heating times used in this study are less than the hydrodynamic response time, attention is now turned to confirming that the targets are responding as

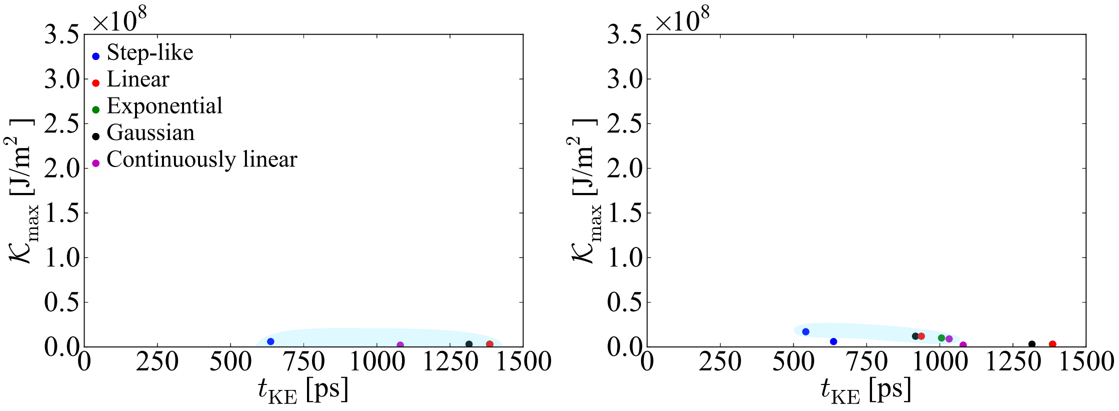

**(a) $t_{\mathrm{H}} = 10$ ps** **(b) $t_{\mathrm{H}} = 25$ ps**

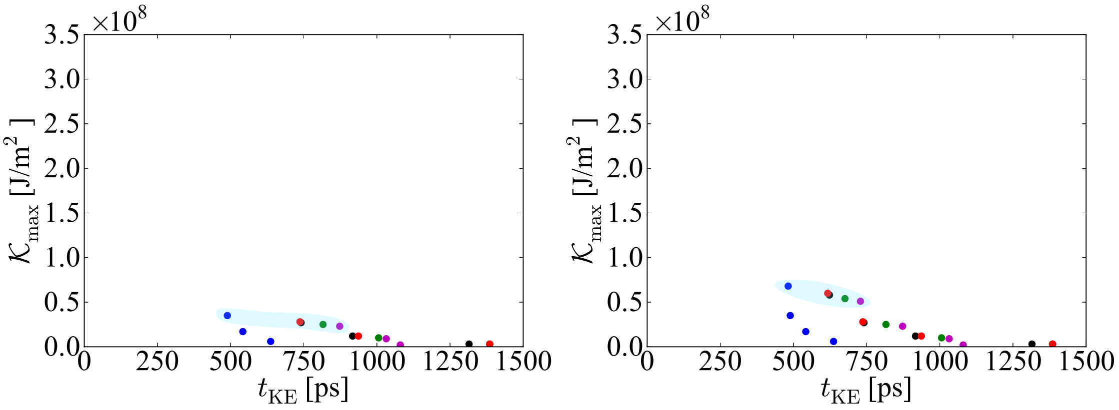

**(c) $t_{\mathrm{H}} = 50$ ps** **(d) $t_{\mathrm{H}} = 100$ ps**

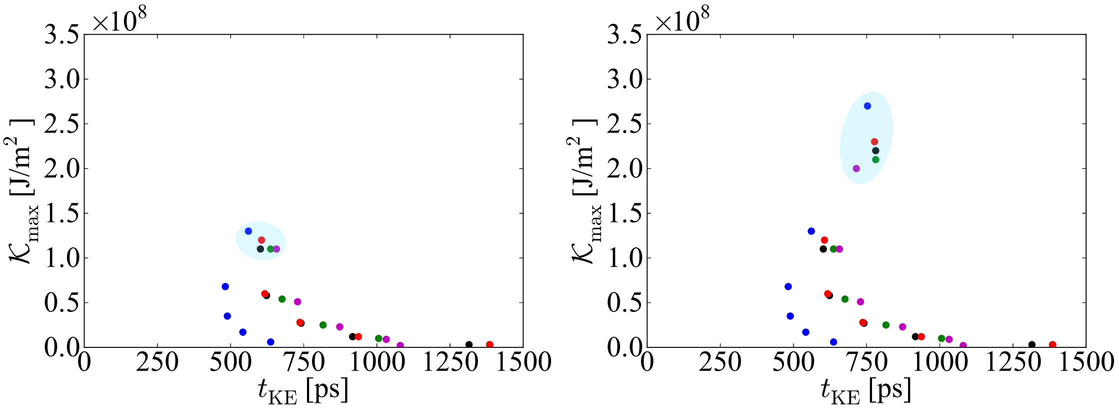

**(e) $t_{\mathrm{H}} = 200$ ps** **(f) $t_{\mathrm{H}} = 400$ ps**

**Figure 7.3: A series of plots of $\mathcal{K}_{\max}$ versus $t_{\mathrm{KE}}$ measured for each target and for different heating times. Each successive plot includes an additional data set (highlighted by a cyan bubble) presenting the results for all of the targets but corresponding to a longer heating time. For example, the group highlighted in Fig. 7.3a represents the measurements made for each of the targets after they have been heated for 10 ps, whereas the group highlighted in Fig. 7.3f represents the measurements made for each of the targets after they have been heated for 400 ps. Note that in Fig. 7.3a the results for the linear (red) and exponential (green) targets coincide.**

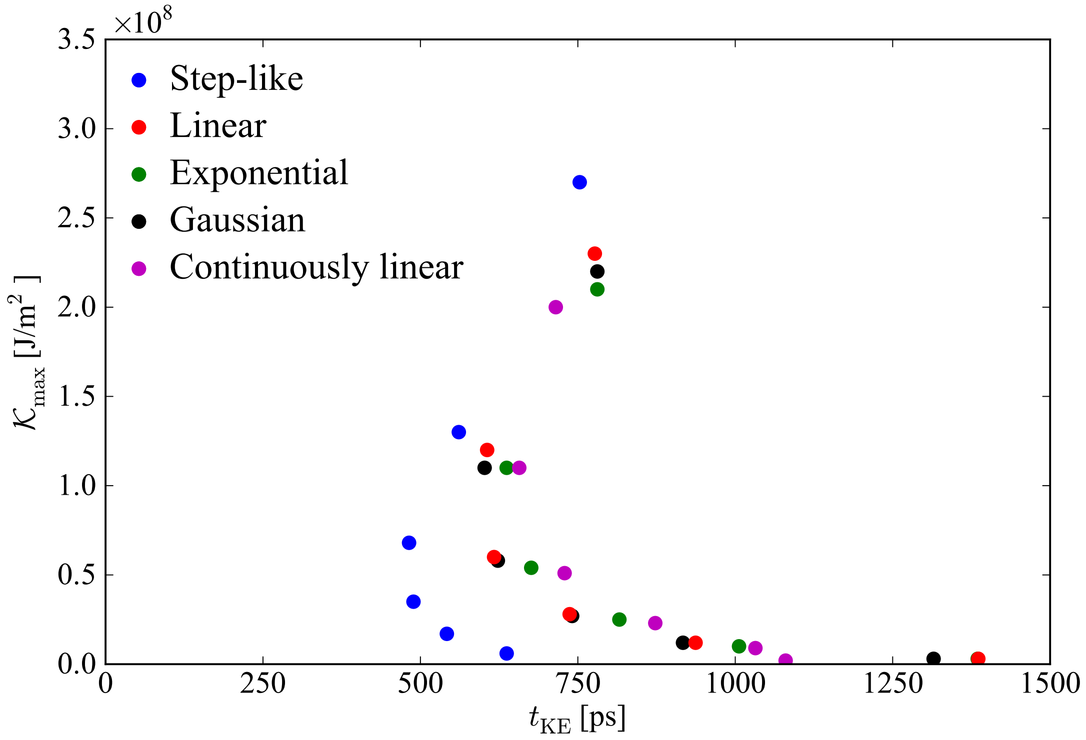

**Figure 7.4: Presented as a set of colour-coded dots are, the maximum areal kinetic energy, $\mathcal{K}_{\mathrm{max}}$, generated and the corresponding time taken to achieve it, $t_{\mathrm{KE}}$ in a suite of simulations in which the target profiles shown in Fig. 7.1 are heated by a 1 PW/cm$^2$, 20 keV Maxwellian population of fast electrons for various heating times. The colours correspond to the target colours in Fig. 7.1. Starting with the lowest dot in each set, the heating times are 10, 25, 50, 100, 200 and 400 ps.**

though instantaneously heated. This is done by initialising stationary targets with the deposition profiles shown in Fig. 7.1, but normalised to contain the total amount of energy that would have been injected during each of the heating times. The simulations then proceed purely hydrodynamically and measurements of $\mathcal{K}_{\mathrm{max}}$ and $t_{\mathrm{KE}}$ are made. Figure 7.6 is a reproduction of Fig. 7.4 but includes the curves that the data points for the step-like and linear targets would follow had the targets responded as though instantaneously heated in this manner. It is seen that at short heating times the data points do indeed correspond well to these curves. The same exercise was performed for all of the targets and similarly good agreement was found but these curves have not been plotted to maintain clarity in the figure.

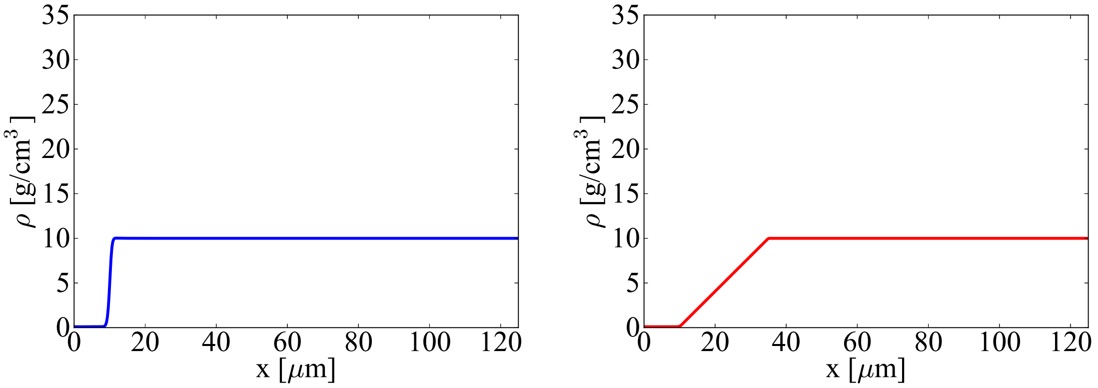

**(a) Step-like - 10 ps** **(d) Linear - 10 ps**

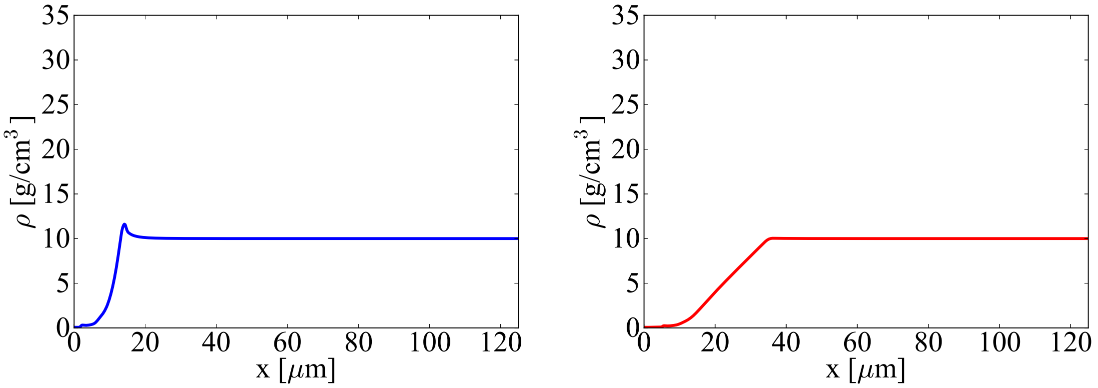

**(b) Step-like - 50 ps** **(e) Linear - 50 ps**

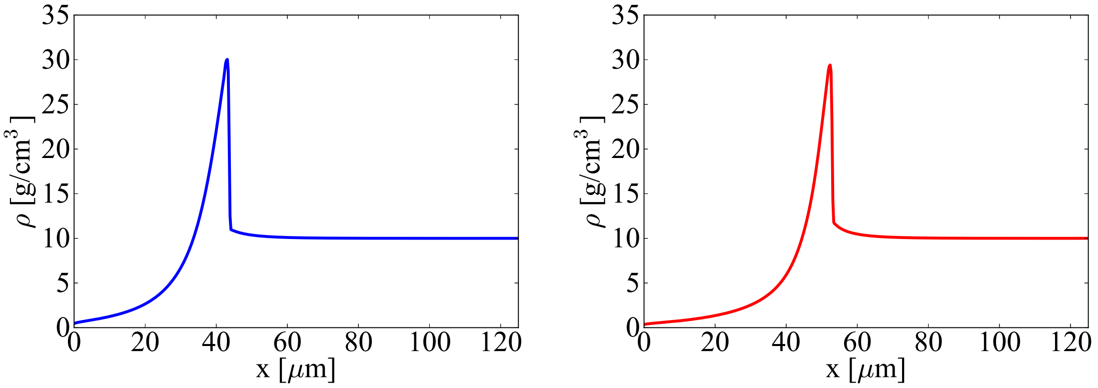

**(c) Step-like - 400 ps** **(f) Linear - 400 ps**

**Figure 7.5: Density profiles for the step-like (blue) and linear (red) targets at the end of the heating time for heating times of 10, 50 and 400 ps. The targets do not respond significantly on the timescale of short heating times so their density profiles resemble the initial conditions. On the other hand, fully established blast wave structures are observed by the end of the heating when it is long.**

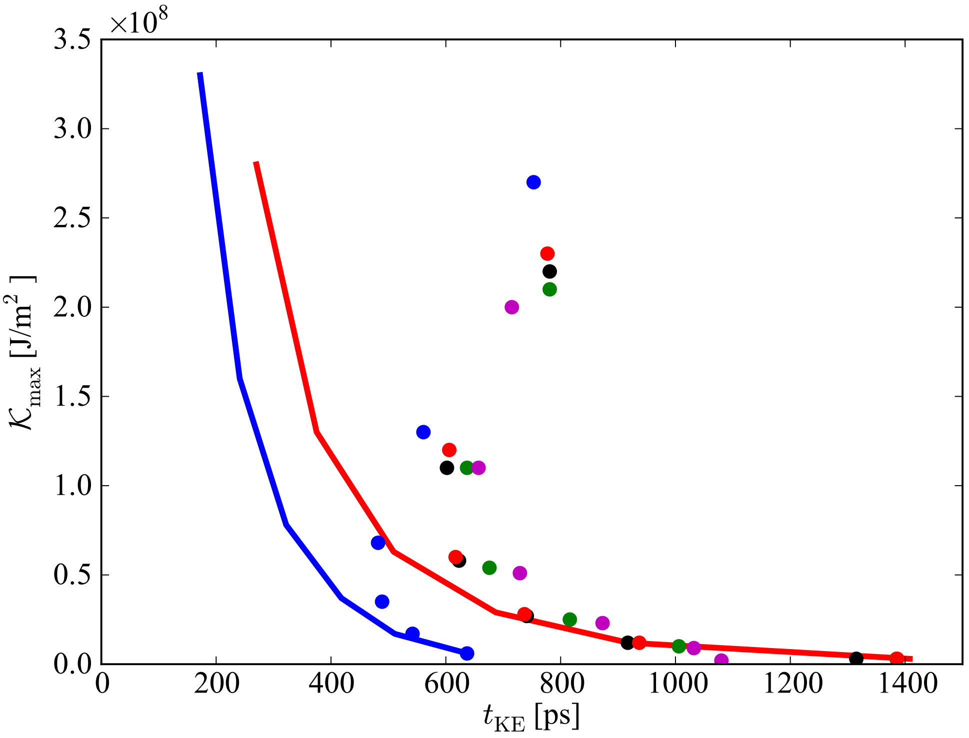

**Figure 7.6: A reproduction of Fig. 7.4 but including solid curves representing the paths that would be taken by the step-like (blue) and linear (red) targets responding as though instantaneously heated.**

As the heating time continues to increase, so too does the maximum areal kinetic energy and the time taken to reach the maximum decreases, but the rate of decrease slows and the dots begin to diverge from the curves. Eventually there comes a point for each target where this trend is reversed and $t_{\mathrm{KE}}$ begins to increase with $t_{\mathrm{H}}$. The cause for this change in the trend can be understood by returning to Fig. 7.5. It is clear that, for longer heating times, the targets are responding in a significant way during the heating time and, at the end of 400 ps of heating, both the step-like and linear targets already display fully established blast wave structures. This means that for longer heating times, an increasing fraction of the injected energy is being deposited in established shock waves. This ‘refuelling’ of the shock wave is the cause for the increase in $t_{\mathrm{KE}}$ as it takes longer to convert the extra thermal energy being delivered.

Two hydrodynamic regimes of fast electron driven shock wave formation can be identified.

When the heating time is less than the hydrodynamic response time, the plasma responds approximately as though it was instantaneously heated - the explosive regime. When the heating exceeds the hydrodynamic response time, ‘refuelling’ of an established shock wave occurs and this drives the shock to greater strength - the driven regime. To illustrate this point, a comparison of the temporal evolution of the simulations using the linear target with heating times of 10 ps and 400 ps is shown in Figure 7.7. Figures 7.7a to 7.7c show that the fast electrons deposit all of their energy into an essentially stationary target that has not evolved significantly from its initial conditions. Subsequently, the thermal pressure drops as thermal energy is converted to directed kinetic energy, and a shock wave develops. It reaches its maximum kinetic energy after 1400 ps and, around the same time, the shock reaches a maximum compression factor of $\sim$1.7. By comparison, Figs. 7.7d to 7.7f show that a well established shock has formed before the end of the heating time of 400 ps and that, over this time, energy is being deposited throughout the shock wave structure. This drives a stronger shock wave that reaches a maximum compression factor of $\sim$3.5 and a peak pressure that is approximately ten times higher than is reached in the $t_{\mathrm{H}} = 10$ ps case. The two regimes of shock wave evolution are approximately highlighted in Fig. 7.8.

It appears from Fig. 7.8 that a more rapid transition from the explosive regime to the driven regime is favourable for efficient conversion of the injected energy to forward-going areal kinetic energy. That is, the shorter the heating time required to make the transition, the more efficient the conversion. The step-like target makes the transition for the shortest heating time and shows the greatest conversion efficiency whereas the continuously linear target needs a significantly longer heating time to transition and shows the lowest conversion efficiency for the same heating time. However, the difference between the results is not vast. For a heating time of 400 ps, which is on par with the expected length of the ignitor pulse in shock ignition, the continuously linear target produces 35% less areal kinetic energy than the step-like target. It is unlikely that the target will

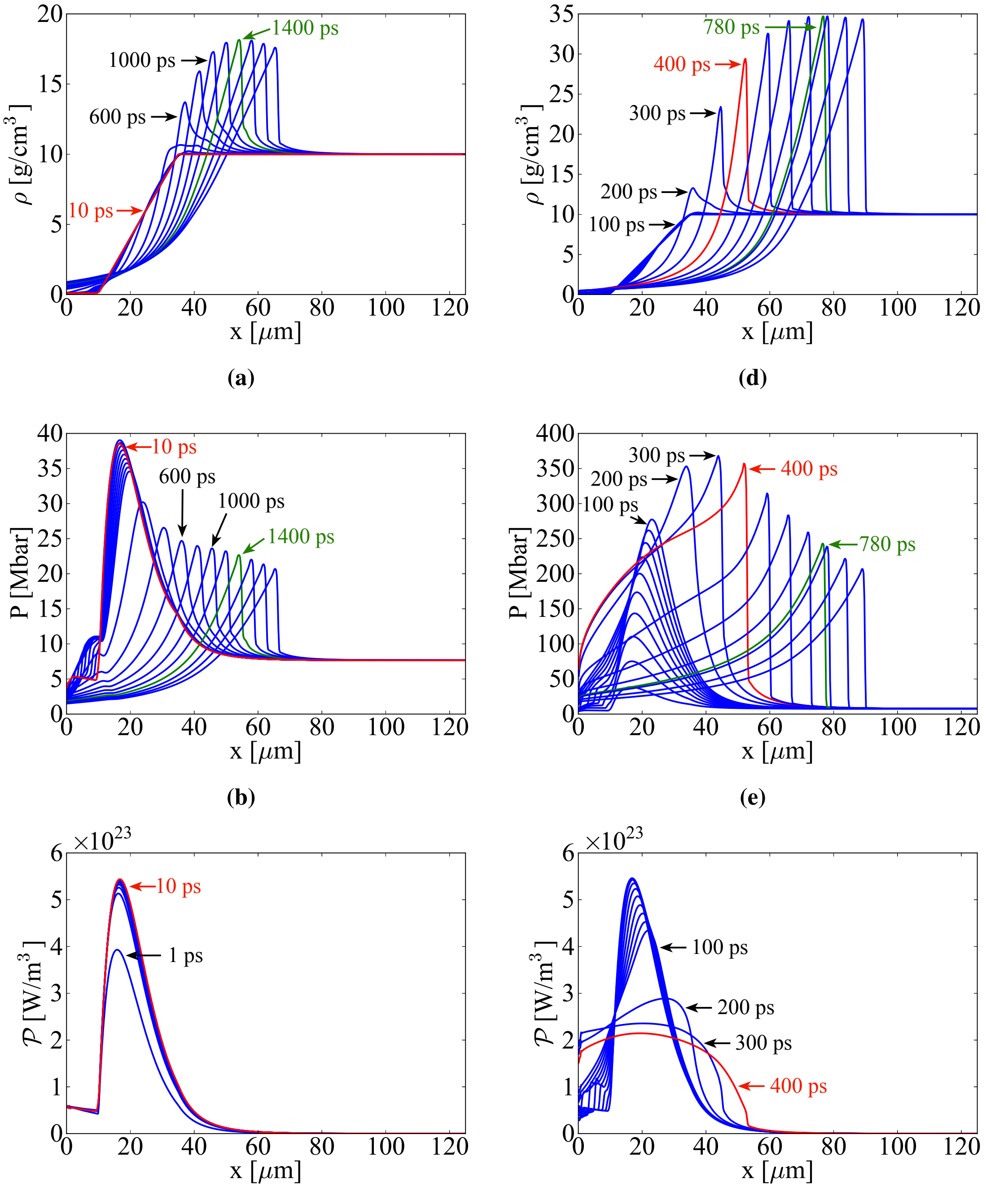

**(a)** **(d)**

**(b)** **(e)**

**(c)** **(f)**

**Figure 7.7: Figures 7.7a to 7.7c show the evolution of the target density and pressure, and the power density deposition profiles when the linear target is heated for 10 ps. Figures 7.7d to 7.7f show the same but for a heating time of 400 ps. In each case, the profiles corresponding to $t_{\mathrm{H}}$ are shown and labeled in red while the profiles corresponding to the time of $\mathcal{K}_{\mathrm{max}}$ are shown and labeled in green. Other profiles are labeled to indicate the rate of evolution. The fast electron population rapidly thermalises so energy deposition ceases soon after $t_{\mathrm{H}}$.**

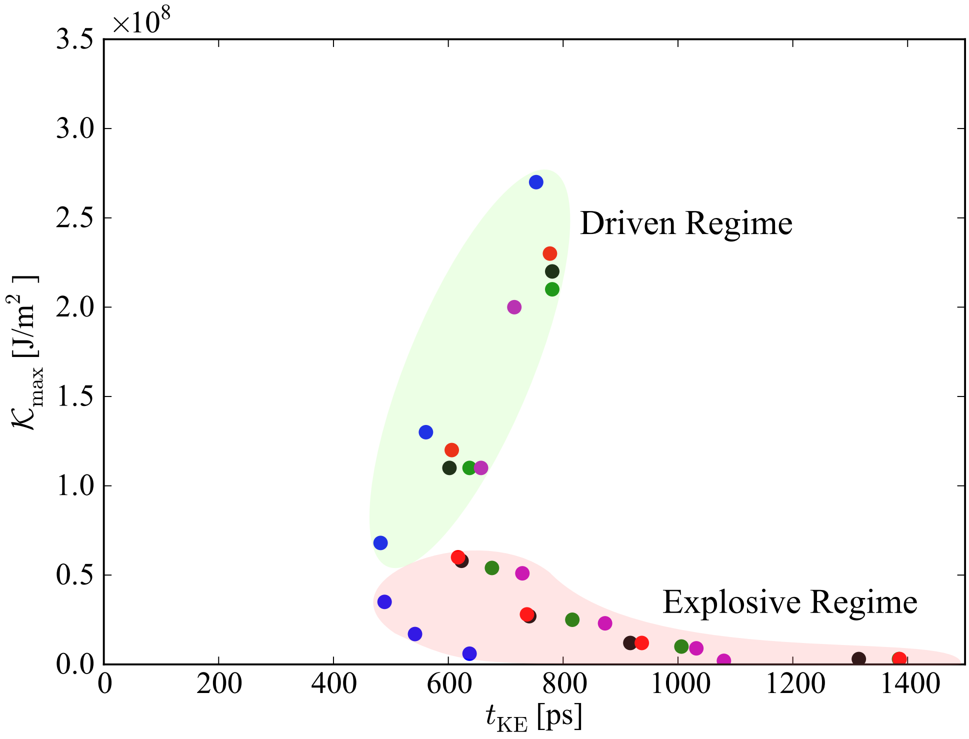

**Figure 7.8: The results presented in Fig 7.6 show two distinct hydrodynamic regimes. When the heating time is short compared with the hydrodynamic response time, the target responds approximately explosively and $t_{\mathrm{KE}}$ decreases with increasing heating time - the explosive regime. When the heating time is long compared with the hydrodynamic response time, an established shock is refuelled and driven to greater strength by the continued heating and $t_{\mathrm{KE}}$ increases with increasing heating time. The maximum areal kinetic energy achieved increases with heating time because the available thermal energy increases - the driven regime.**

have a step-like profile or that the density profile can be controlled to any significant extent, so the fact that there is not a huge spread in the results is favourable. It should be possible to account for the spread in an appropriate shock ignition scheme design. For example, it may prove to be possible to accelerate the regime transition by using a short, high intensity pulse to more quickly establish the blast wave and then scale the intensity back while driving the shock to the required strength. However, if it turns out that shock ignition is more difficult than anticipated and that the tolerances are quite low, then the effect of the density profile on shock wave formation efficiency will need to be considered more carefully.

Attention is now turned to the spread in the measured values for $t_{\mathrm{KE}}$ for a given heating time. This spread is most noticeable in the explosive regime. For example, Fig. 7.8 shows that, for a heating time of 10 ps, the step-like target took $\sim$640 ps to reach maximum areal kinetic energy whereas the linear target took $\sim$1400 ps. An initial understanding of this feature can be achieved by applying the scaling relation for the shock wave development time (Eq. 6.4) to the 10 ps heating time results.

The shock waves generated in those targets with a uniform density region (Figs. 7.1a to 7.1d) very quickly begin propagating through that uniform density region. This means that, by excluding the continuously linear target from the present analysis, the dependence on density in Eq. 6.4 may be treated as a constant across the simulations. The time taken to reach the maximum areal kinetic energy then depends on the size of the heated region and the thermal energy available to generate a forward-going shock wave. Using the measured sizes and energy contents from the simulations, Eq. 6.4 indicates that the step-like target should reach its maximum areal kinetic energy soonest, and the linear target should do so the latest. The Gaussian and exponential targets are ranked in the wrong order when compared with Fig. 7.8. Thus, Eq. 6.4 does broadly give the correct results but does not reproduce the details well. The important point however is that anything other than a step-like target is universally worse for the time taken to reach the maximum kinetic energy and for the amount of kinetic energy developed. The step-like target reaches a maximum areal kinetic energy that is twice that of the linear, Gaussian and exponential targets.

The shock wave generated in the continuously linear target is considered separately because its target density profile is distinctly different from the other targets, i.e. it encounters an increasing density profile compared with a uniform density profile. The propagation of shock waves down density gradients described by a power law ($\rho = Ar^{-\omega}$, where $A$ and $\omega$ are constants) have been considered in the context of supernovae remnants [107, 115]. Replacing the density in Eq. 6.1 with a power law gives,

$$R_s \propto (Et^2)^{\frac{1}{5-\omega}}. \tag{7.1}$$

Then, for a linearly increasing profile, ($\omega = -1$), $\dot{R}_s \propto t^{-2/3}$. In Chapter 6, it was found that $\dot{R}_s \propto t^{-2/5}$ in a uniform density. Thus, a shock wave will decelerate more rapidly when propagating through a linearly increasing density profile compared with through a uniform density. This goes some way to explaining why, despite having by far the longest scale length deposition profile, the continuously linear target reached its maximum areal kinetic energy much sooner than the linear, exponential and Gaussian targets. Based on the measurement of $t_{\mathrm{KE}}$ alone, increasing density gradients may seem beneficial because a shorter time to develop the shock is generally desirable. However, the maximum areal kinetic energy developed in the continuously linear target is one third of the maximum reached in the step-like case.

So far, only the properties of the system after 10 ps of heating have been considered. This does not take into account the effect of an evolving density profile and the subsequent change in the pressure profile. This will undoubtedly affect the formation of a shock wave and is the likely cause of the change in order of the targets along the $t_{\mathrm{KE}}$ axis with increasing heating time. For example, the linear target has the longest $t_{\mathrm{KE}}$ for 10 ps of heating but is the second quickest after 50 ps of heating.

Whatever the cause for the spread in the $t_{\mathrm{KE}}$ that occurs for short heating times, it seems to become less important as the heating time increases. For a heating time of 10 ps, the measured values of $t_{\mathrm{KE}}$ increase by 120% from the fastest to the slowest. This range reduces to just 10% for a heating time of 400 ps. Furthermore, the percentage difference between the extrema in the measured $\mathcal{K}_{\mathrm{max}}$ has reduced from 200% to 35% (although this is a larger absolute spread). This suggests that the effect of the plasma profile on $t_{\mathrm{KE}}$ is lost if one heats for long enough. This makes sense when looking at Fig. 7.5. For longer heating times a greater fraction of the energy is being deposited into a density profile that looks very similar from one target to the next, i.e. it is impossible to say what the starting profiles were from the profiles at 400 ps. Thus, as one heats for longer, the effect of the density shape effectively becomes more like a transient phase in the shock wave formation. The remnant of its influence is left in the conversion efficiency. This is a positive result for shock ignition in which the ignitor pulse is expected to be a few hundred picoseconds long.

## 7.4 Summary

It is unreasonable to expect that the density profile of the dense shell in an imploding shock ignition target will be the perfect step-like profile studied in Chapter 5. To gauge the importance of a shaped density profile in fast electron driven shock wave formation, the exponential pre-plasma profile expected to be produced during target implosion has been mimicked, and the process of shock formation in this target, in a step-like target and in additional targets with alternative density ramps has been compared. Each target was subjected to a 1 PW/cm$^2$, 20 keV Maxwellian beam of hot electrons for various amounts of time, and measurements were made of the maximum areal kinetic energy developed and the time taken to develop it.

Two distinct hydrodynamic regimes have been identified. When the heating time is shorter than the hydrodynamic response time, the targets respond explosively, almost as though they were instantaneously heated. This has been called the explosive regime. As the heating time is increased a general trend of increasing $\mathcal{K}_{\mathrm{max}}$ and decreasing $t_{\mathrm{KE}}$ is followed but becomes increasingly divergent from that expected for purely explosive shock wave generation. This divergence is caused by target deformation and shock wave generation on the timescale of the heating time. It is the case then, that for longer heating times, an increasing fraction of the injected energy is being deposited into a propagating shock wave. This ‘refuelling’ of the shock wave drives it towards a greater maximum kinetic energy which correspondingly takes longer to achieve. This has been called the driven regime.

A rapid transition from the explosive to the driven regime appears to be favourable for more efficient conversion of the fast electron energy to kinetic energy in the shock wave and any deviation from a step-like target gives a universally worse performance. However, the difference between the best and worst performers is approximately 35%. While this is not insignificant, it is plausible that a well designed ignition scheme could account for this level of underperformance. It may be the case that a rapid transition could be encouraged by irradiating the target with an increased intensity before reducing it to a standard shock ignition intensity. According to Eq. 6.4, the increased energy deposition should drive an explosive shock wave more rapidly, which could then be driven to higher kinetic energies.

It is also noted that Eqs. 6.4 and 7.1 give a reasonable account of the spread in the measured values of $t_{\mathrm{KE}}$ in the explosive regime, although the details are not fully explained. This spread becomes less apparent as the heating time is increased and almost lost altogether for the longest heating times considered in this study.

In general the above findings are positive in the context of shock ignition. On the timescales proposed for shock ignition, the density profile shaping does not greatly influence the time taken to drive a shock wave to its maximum areal kinetic energy and has a potentially manageable effect on the conversion efficiency of fast electron energy to shock wave kinetic energy.

# Chapter 8

# Shock Wave Formation in Magnetised Targets

## 8.1 Introduction

The potential to enhance inertial confinement fusion target performance by thermally insulating the hot spot using large magnetic fields has been explored over the years (see Refs. 116–119 and the references therein). For example, magnetised inertial confinement fusion [119] is a variant of inertial confinement fusion in which a spherical target is seeded with a magnetic field of $\sim$10 T. The magnetic field is enhanced by compression to several kT which is sufficient to thermally insulate the hot spot by restricting electron transport. Experiments have demonstrated a 30% enhancement in the neutron yield using this method [120, 121]. In these experiments the seed field has been delivered using the Magneto-Inertial Fusion Electrical Discharge System (MIFEDS) device [122]. This is a vacuum enclosure housing a high-voltage charging power supply, capacitors and a laser-triggered spark-gap switch. It is capable of storing $\sim$100 J of energy and delivering many tens of kA of discharge current in $\sim$400 ns down an external transmission line to a coil. The shape of the coil determines the magnetic field topology and strength.

Magnetic fields of tens of Tesla up to 1 kT have been achieved using laser plasma interactions in which laser generated fast electrons induce a potential difference between two parallel plates which drives a strong current through a wire coil connecting the two plates [123–125]. Using such strong fields, it may be possible to approach the idea of magnetised inertial confinement fusion from the opposite direction. That is, rather than limiting thermal conduction out of the hot spot, it may be possible to use strong magnetic fields to limit the range of incoming laser generated fast electrons so that they deposit their energy near the surface of an imploding spherical target and thereby contribute to the generation of a strong shock wave, such as is used in shock ignition. In this chapter, this idea is explored by simulating fast electron driven shock wave generation in magnetised planar targets using Maxwellian electron populations. The results presented herein represent a preliminary study of the problem and further work should be undertaken to explore it fully. That being said, it is clear that a sufficiently strong magnetic field will localise fast electron energy deposition which subsequently drives a shock wave. Localising the energy deposition mitigates the need for excessive spatial and temporal scales to allow the shock wave to fully develop when using Maxwellian electron populations. However, it is found that a combination of a strong magnetic field and rapid shock wave development means that the energy deposition is more rapidly spatially decoupled from the shock wave. This results in a weaker shock wave than would have otherwise been generated.

## 8.2 Theory

The idea behind this chapter is based on a very simple premise; in the absence of all other forces, an electron with velocity $v$, that is perpendicular to a uniform magnetic field $B$, will orbit the magnetic field lines at the gyro-radius:

$$r_g = \frac{m_e v}{eB}. \tag{8.1}$$

Thus an electron that is injected with velocity $v$, perpendicular to a uniform magnetic field of strength $B$, will travel at most a distance $r_g$, from its source. If over this range there exists a target, the circulating electron will lose energy to the target. In effect, the range over which the electron deposits its energy has been reduced if it would have otherwise propagated a distance greater than $r_g$. It may then be possible to avoid the need for excessive temporal and spatial scales when driving shock waves using fast electrons populations with extended energy distributions (see Chapter 5). It may also be possible to avoid target pre-heat by ordinarily too-hot electrons and instead use them to contribute towards shock wave generation. This idea is explored with a suite of preliminary simulations in which a 30 keV fast electron population is injected into a solid density plastic target. This target is chosen to explore a more experimentally accessible regime than has so far been considered in this thesis. It turns out that this requires magnetic fields on the order of 10 to 100 T. Although it is challenging, progress has been made in achieving such high fields in laser-plasma experiments that have been designed with the aim of making use of the fields in other laser-plasma interactions. It has been shown that high magnetic fields can be achieved by using laser generated fast electrons to induce a potential difference between two parallel plates which drives a strong current through a wire coil connecting the two plates [123–125]. Collectively these experiments demonstrate the potential of achieving magnetic fields of up to 1 kT using a single loop in the coil [125] or lower fields of tens of Tesla that are spatial uniform over $\sim$1 mm using Helmholtz coils [124].

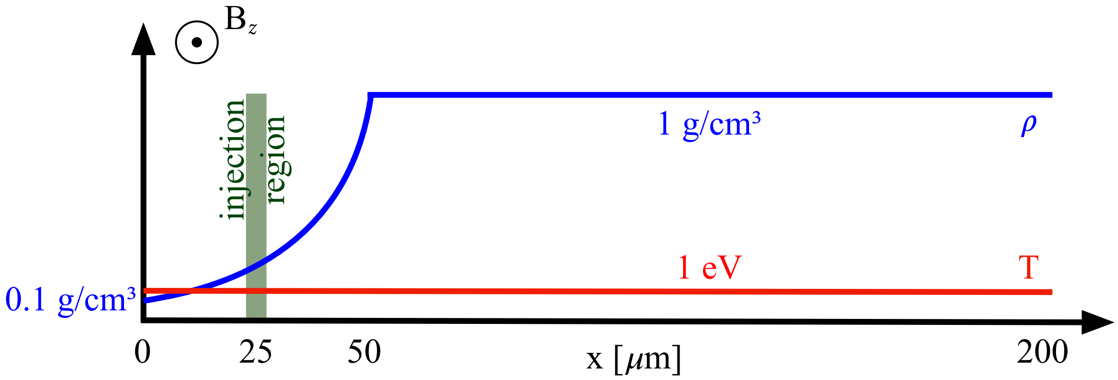

**Figure 8.1: Schematic of the background plasma initial conditions. The stationary, CH target has a 50 $\mu$m exponential density ramp from 0.1 g/cm$^3$ to 1 g/cm$^3$, followed by a 150 $\mu$m uniform density at 1 g/cm$^3$. The temperature is initially uniform at 1 eV. The fast electron population is injected over the region 24—26 $\mu$m with an intensity of 1 PW/cm$^2$ and temperature of 30 keV.**

## 8.3 Description of the Simulation Design

A schematic of the simulation design is shown in Fig. 8.1. It shows a CH target with a density profile consisting of a 50 $\mu$m exponential ramp from 0.1 to 1 g/cm$^3$, and a 150 $\mu$m long uniform density region at 1 g/cm$^3$. The average, fully ionised CH ion has a mass of 6.5m$_p$ and an effective atomic number of $Z = 3.5$. The initial temperature is uniform at 1 eV. The magnetic field is initially uniform and in the $z-$direction. Its initial magnitude is varied from 0 to 100 T between simulations. A 30 keV Maxwellian fast electron population is injected continuously and uniformly over the region indicated at 24—26 $\mu$m, with an intensity of 1 PW/cm$^2$, is beamed with $M = 16$ and represented with harmonics up to $l = m = 17$. The fast electrons encounter open boundaries at both domain walls to avoid the effect of reflected currents on the magnetic field evolution. The injected electrons are equally likely to travel to the left as to the right, so the on-target intensity is 0.5 PW/cm$^2$.

The spatial resolution is $\Delta x = 1$ $\mu$m, the momentum grid has 75 cells with a resolution of $\Delta p = 0.1 p_{\text{th}}$ and a time step of 0.9 of the Courant condition is used throughout. The results presented in this section are preliminary and have not undergone convergence testing. It can be

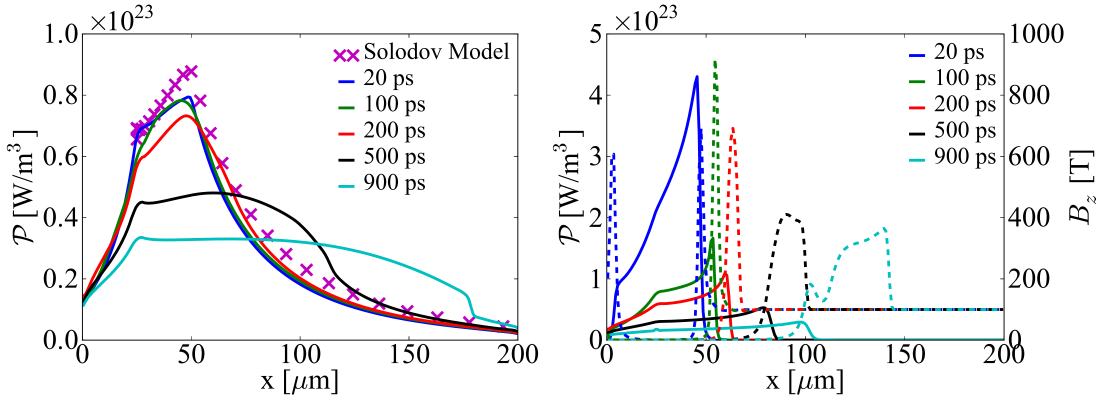

**(a) $B_z$ = 0 T** **(b) $B_z$ = 100 T**

**Figure 8.2: Time evolution of power density deposition (solid) and magnetic field (dashed) profiles produce by a 30 keV Maxwellian electron beam injected with an intensity of 0.5 PW/cm$^2$. Figures 8.3a and 8.3b correspond to initial magnetic fields of 0 T and 100 T, respectively. Figure 8.3a also compares the deposition profile calculated using the hybrid model after 20 ps in the absence of a magnetic field with the deposition profile calculated using Solodov model (crosses).**

expected that greater spatial resolution will refine the fast electron energy deposition profiles, refine the shock wave profiles, and will likely lead to higher maximum pressures and densities. However, the differences between the simulations are stark enough that comparative conclusions can be drawn, even if the absolute measurements of the physical quantities are subject to change.

## 8.4 The Effect of an Externally Applied Magnetic Field

A suite of simulations, initialised as described above, were run with initial magnetic fields in the range of 0 to 100 T. The effect of the magnetic field on the range of the fast electron population can be most easily seen in Fig 8.2. Fig. 8.2a shows the spatial power density deposition profile (solid lines) at various times in the absence of a magnetic field. Also shown is the power density deposition profile calculated using the Solodov model. This was calculated using Eq. 3.56, including scattering and assuming that a 30 keV Maxwellian electron population is injected in the forward direction with an intensity of 0.5 PW/cm$^2$ for 20 ps. There is very good agreement between the

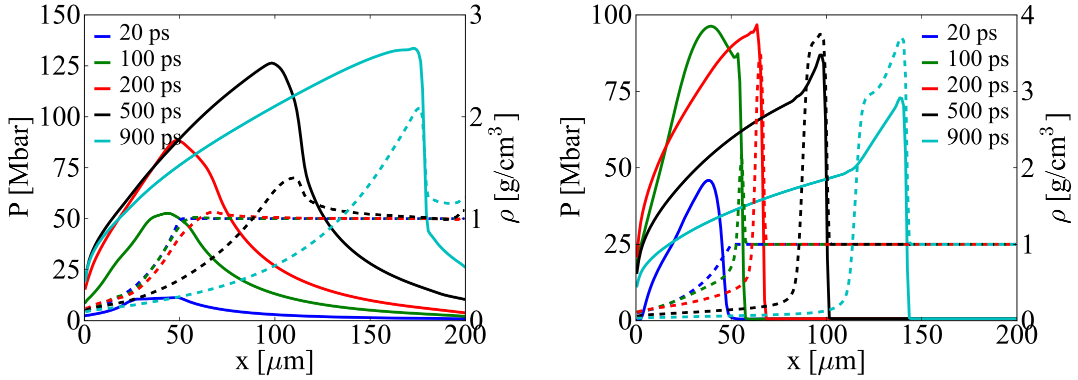

**(a)** $B_z$ **= 0 T**

**(b)** $B_z$ **= 100 T**

**Figure 8.3: Time evolution of the thermal pressure (solid) and density (dashed) profiles produce by a 30 keV Maxwellian electron beam injected with an intensity of 0.5 PW/cm$^2$. Figures 8.3a and 8.3b correspond to initial magnetic fields of 0 T and 100 T, respectively.**

Solodov model and the hybrid model after 20 ps, considering the differences between the models (see Section 3.8.3). Figure 8.2a shows that, in the absence of a magnetic field, the fast electrons are sufficiently energetic to propagate through the length of the target. Figure 8.2b shows that when an initial 100 T magnetic field is applied, the range of the population is significantly reduced. At 20 ps the fast electrons have propagated just 25 $\mu$m from the injection region. However, this field is significantly stronger than expected to be necessary to limit the range to 25 $\mu$m. Equation 8.1 predicts that, for a fast electron velocity of $\sim 10^8$ m/s, a magnetic field of 23 T should limit their range to 25 $\mu$m. Figure 8.2b even shows that after 900 ps, energy is being deposited up to 80 $\mu$m from the source. The difference is that the magnetic field does not remain at its initial magnitude but is reduced by the resistive current term in Ohm's law (Eq 3.84). This can be seen in Fig. 8.2b where the magnetic field becomes negligible in an expanding region around the injection region. Simulations using lower magnetic fields show similar profiles to those in Fig. 8.2b but with more extended power density deposition profiles as the electrons have longer ranges.

It was concluded in Chapters 5 and 6, that shock waves develop more readily when driven by localised energy sources. This is borne out in the thermal pressure and density profiles of the

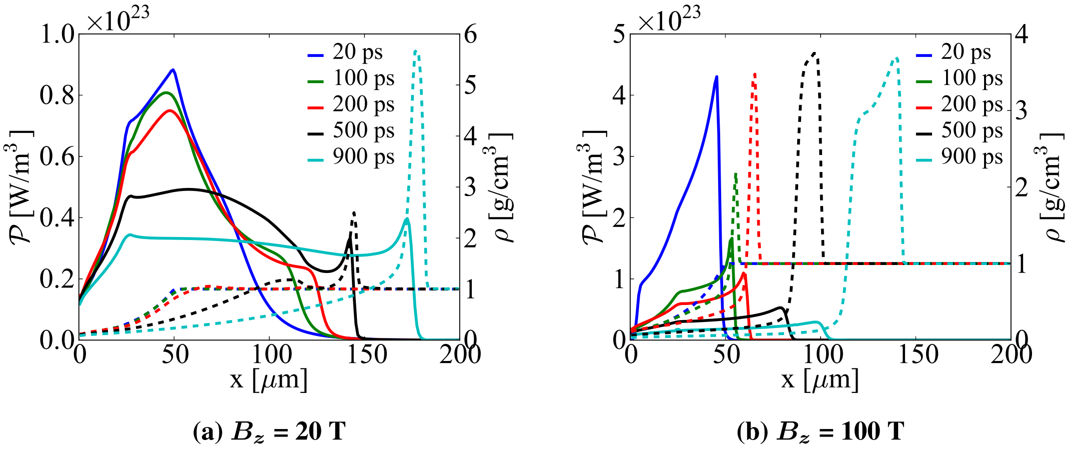

**(a)** $B_z$ **= 20 T**

**(b)** $B_z$ **= 100 T**

**Figure 8.4: Time evolution of power density deposition (solid) and density (dashed) profiles produce by a 30 keV Maxwellian electron beam injected with an intensity of 0.5 PW/cm$^2$. Figures 8.3a and 8.3b correspond to initial magnetic fields of 20 T and 100 T, respectively.**

$B_z = 0$ T (Figs. 8.3a) and the $B_z = 100$ T (Figs. 8.3a) cases. In the former case, the shock has not finished developing by the end of the simulation and has reached a pressure of 135 Mbars and the profiles are similar to those in Fig. 5.5. In the latter case, a peak pressure of 100 Mbars is reached after 100 ps and the profiles are similar to those in Fig. 5.3, i.e. in the case of a strong magnetic field the shock wave develops as though driven by a monoenergetic source. It was also concluded in Chapter 5 that the peak pressure should be only a weak function of the deposition scale length. This is not the case here where both the size of the heated region and the peak pressure decrease with increasing magnetic field strength. For example, when $B_z = 20$ T, a peak pressure of 152 Mbars is reached after 150 ps. That is, the peak pressure is decreased by 35% by increasing the magnetic field strength from 20 T to 100 T.

The decrease in the time taken for the shock wave to develop and the decrease in the peak pressure with increasing magnetic field strength can be explained by the energy deposition being no longer co-located with the shock wave earlier in time. As discussed, a higher magnetic field leads to more rapid shock wave formation. Then, the subsequent compression of the target enhances the density and the strength of the magnetic field (in Fig. 8.2b the magnetic field is amplified from 100

T to 1 kT). Both of these factors reduce the range of the fast electrons and thereby limit the amount of energy being deposited in the shock wave. Figures. 8.4a and 8.4b compare the deposition and density profiles for the $B_z = 20$ T and the $B_z = 100$ T cases, respectively. They show that, as observed when driving shock waves with monoenergetic beams in Chapter 5, the deposition front is eventually no longer co-located with the shock front and tracks the rear of the high density region. Furthermore, when $B_z = 100$ T the deposition front becomes completely spatially detached from the shock wave sometime before 900 ps. On the other hand, in the $B_z = 0$ T case the electrons can always deposit energy in the developing shock wave and therefore contribute to its continued development.

The cessation of energy deposition in the shock wave at earlier times for higher magnetic fields is also responsible for a more rapid decay of the shock pressure. This is the same observation that was made when comparing the use of monoenergetic and Maxwellian beams in Chapter 5. When $B_z = 40$ T, the shock pressure decays approximately linearly at a rate of 0.01 Mbar/ps whereas when $B_z = 100$ T, the shock pressure decays at a rate of 0.04 Mbar/ps.

The effect of the magnetic field is not included in the hydrodynamic module of the hybrid model. Its potential impact on the shock wave dynamics is assessed by considering the plasma-$\beta$ and the Hall parameter. The plasma-$\beta$ is the ratio of the plasma thermal pressure to the magnetic pressure. If the thermal pressure is taken to be on the order of 100 Mbar and the maximum magnetic field of 1 kT, then $\beta = 25$. Using a more average magnetic field of 500 T gives $\beta = 100$. This basic analysis suggests that the effect of the magnetic pressure would be on the order of a few percent and its inclusion is not expected to significantly affect the conclusions that have been made. The Hall parameter is given by $\omega_g \tau_{ei}$, where $\omega_g = eB/m_e$ is the electron gyro-frequency and $\tau_{ei}$ is the background electron-ion collision time. When $\omega_g \tau_{ei} \gg 1$, the background electrons are magnetised and their transport will be affected by the magnetic field. This could indirectly affect the shock wave dynamics through thermal conduction effects. However, even in the $B_z = 100$ T case, the maximum value of the Hall parameter reached throughout the simulation is 0.05. This reduces to 0.003 in the $B_z = 20$ T case. Thus, again the inclusion of the magnetic field in the hydrodynamic module is not expected to significantly affect the conclusions that have been drawn.

## 8.5 Summary

A preliminary study of fast electron driven shock wave generation in magnetised targets has been presented. Sufficiently strong magnetic fields can act to localise the otherwise extended energy deposition profile produced by a Maxwellian fast electron beam. This mitigates the need for extended spatial and temporal scales to allow the shock wave to fully develop, which have so far been a characteristic of shock wave formation driven by Maxwellian beams. The ensuing shock wave structure is similar to those driven by monoenergetic beams. As the shock wave develops, the target density and magnetic field are compressed and amplified. Together these effects can reduce the range of the fast electrons to such a degree that energy is no longer being deposited in the shock front or indeed in the shock wave at all. The higher the initial magnetic field the more rapidly the shock wave develops and the more rapidly deposition no longer occurs at the shock front. The result is a weaker, more rapidly decaying shock wave than would have otherwise been produced. This may be acceptable if the reduction in the required spatial and temporal scales confers some advantage.

The efficiency of shock wave generation using Maxwellian fast electron beams in magnetised targets may be improved by limiting the injection time to the time taken for the energy deposition to become spatially decoupled from the shock front. In this way the driver-target coupling inefficiencies can be minimised. Thus it may be the case that, in comparison to a shock driven in an un-magnetised target, the same strength of shock wave can be produced but in a shorter time and over a shorter distance.

This preliminary study has been performed in a planar geometry in which fast electrons are injected only perpendicular to the magnetic field lines. In a spherical system, such as that used in magnetised inertial confinement fusion, electron transport will occur differently orientated relative to the parallel magnetic field lines depending on their direction of propagation. The resulting deposition profile is unlikely to be spherically symmetric and, depending on the relative importance of fast electron heating in magnetised inertial confinement fusion, this may prove to be detrimental to the generation of symmetric spherically convergent shock waves. Furthermore, it is likely to be challenging to produce initially uniform magnetic fields across the whole target and any asymmetries that occur in the target during compression or in the fast electron population will also affect the uniformity of the field. This in turn will also affect the symmetry of the convergent shock wave. It may then be the case that the usefulness of shock waves generated by localising energy deposition using strong magnetic fields is limited to a planar geometry.

Finally, although the hydrodynamic module does not include the effect of a magnetic field, a consideration of the plasma-$\beta$ indicates that the hydrodynamics are dominated by the thermal pressure, and a consideration of the Hall parameter indicates that the background electrons are not magnetised. Thus, the conclusions that have been drawn are not expected to be significantly affected by the inclusion of magnetohydrodynamic terms or the effects a magnetic field may have on thermal transport.

# Chapter 9

# Conclusions

A 1D planar hybrid model has been developed and applied to the problem of strong shock wave generation by fast electron energy deposition in shock ignition relevant plasmas. It combines a kinetic treatment of relativistic electron transport with a single-fluid, two-temperature hydrodynamic description of the target plasma. Despite its limitations, this model has been successfully used to elucidate some of the governing mechanisms in the problem at hand. A summary of the results of this study is presented, followed by an overview of their implications for shock ignition and potential directions for further work.

## 9.1 Summary of Results

The scope of this thesis was motivated by an initial numerical study on fast electron driven shock wave generation using monoenergetic electron beams in dense, step-like plasmas [43]. The realism of this initial study was first improved by taking a cue from recent particle-in-cell modelling [87–91, 100] and experimental evidence [95, 96, 98, 99], and describing the electron population with a Maxwellian energy distribution. It was found that using a Maxwellian energy distribution, as opposed to a monoenergetic distribution, did not adversely affect the peak shock pressures that can be achieved and that the peak pressures obey a simple scaling law that depends on the electron beam intensity and the target density [12]. This is despite the significant differences in the shapes of their energy deposition profiles in step-like targets. However, it was found that the spatial extent of the heating profile is crucial in determining the temporal and spatial scales required for the peak pressure to be achieved. Shock waves driven by electron populations with Maxwellian distributions take significantly longer than those driven by electron populations with monoenergetic distributions of equivalent mean energies. It is noted that, subsequent to the publication of Fox et al. [12], a very similar study was undertaken by Nicolai et al. [41] and the results of which agree strongly with our own.

A study of blast wave formation in uniform fluids confirms the dependence of shock formation time on the size of the heated region. In this study, a scaling law for the time taken for an initial, localised source of internal energy to drive a blast wave containing its maximum amount of kinetic energy is obtained by dimensional analysis and confirmed using the hydrodynamic module of the hybrid model. This scaling law also shows the dependence of the shock wave formation time on the amount of internal energy available to drive the blast wave and the ambient density. Difficulties were encountered when trying to reproduce the dependence on the size of the heated region by fast electron heating of step-like targets. This is due to the inter-related nature of the size and shape of the heated region, the energy available to drive a blast wave and the pressure ratio between the peak pressure in the heated region and the pressure of the ambient medium. This demonstrates some of the difficulties that may be encountered if fine control over shock wave formation is required.

The effect of the target density profile on shock wave formation was considered. It was found that any deviation from a step-like target was detrimental to the efficiency of converting fast electron energy into shock wave kinetic energy. Two hydrodynamic regimes of shock wave formation are identified - the explosive regime and the driven regime. It appears that a more rapid transition from the explosive to the driven regime is favourable for driver efficiency. The greatest disparity between targets in the time taken for the shock wave to contain its maximum kinetic energy is exhibited in the explosive regime. The scaling law for blast wave formation obtained previously successfully describes the broad trends in this observation but does not reproduce the details well. This is likely due to the evolution of the system on the time scale of shock wave formation. The effect of the initial target density profile becomes less noticeable in the driven regime with the spread in the time taken to reach the maximum kinetic energy being significantly reduced. The spread in the maximum kinetic energy is an artefact of the density profile and its effect on the transition time.

Finally, a preliminary study on enhancing localised fast electron energy deposition using externally applied strong magnetic fields has demonstrated that the spatial and temporal scales required to generate shock waves using electron populations with extended energy distributions can be reduced. However, this approach seems to be self limiting in that the energy deposition becomes spatially decoupled from the shock front at earlier times and from the shock wave altogether if the magnetic field is strong enough. This results in a weaker shock wave than would have otherwise been generated.

## 9.2 Conclusions

The generation and characterisation of fast electron populations is one of the major unknowns in shock ignition. Some effort has been made elsewhere, both experimentally and numerically, to begin to address this problem. It is becoming apparent that it is reasonable to expect the generation of moderately hot electron populations with approximately Maxwellian energy distributions, although the conversion rate of laser energy into hot electrons is not so well understood. Nonetheless, it has been demonstrated here that, at least in principle, these hot electrons can be used to drive strong shock waves in shock ignition relevant plasmas and generate sustained shock pressures of several hundred Mbars. Such pressures are required of the ignitor shock to ignite the hot spot in shock ignition. However, careful consideration should be made of the temporal and spatial scales required for these shocks to develop. If the fast electron population is too hot, the scale length of its deposition profile will not be contained within the length of the target plasma. In this case, a shock wave will not fully develop and the desired peak pressures will not be reached. Instead the plasma will have been nearly uniformly pre-heated which is not conducive to hot spot ignition.

It appears that the shape of the target density profile is of secondary importance when compared with the problem of matching the hot electron temperature with the target density. It is found that when the fast electron heating time is comparable to the length of ignitor pulse, the target profile does not greatly affect the time taken for the shock wave to contain its maximum kinetic energy but it does affect the magnitude of that maximum with the variation in our study being approximately 35%. While this is not insignificant, this variance should be manageable within an ignition scheme design, assuming that the tolerances of shock ignition are not too low. It would be interesting to investigate if the shock wave generation regime change could be hastened and the driver efficiency improved for non-step-like targets by temporally shaping the beam intensity.

Given the demonstrated capacity of fast electrons to generate strong shock waves it may be worth considering an alternative approach to shock ignition in which the generation of fast electrons is not avoided but actively sought. Then, with a carefully considered assembly phase to generate an appropriate density, it may be possible to use fast electrons as the dominant driver of the ignitor shock. This may have the advantage of reducing the total laser energy because fast electrons can more efficiently transport their energy through the corona and to higher densities than thermal electrons. As it stands, the hybrid model has the advantage of treating fast electron energy deposition fully kinetically but it does not include the thermonuclear burn or radiation transport physics that would be required to complete such a study. In principle, and as a first step, it could be coupled to a more complete radiation-hydrodynamics model, although preferably these routines would be added to the hybrid model itself.

The hybrid model is capable of extending the study of fast electron driven shock wave generation to other inertial confinement fusion schemes. For example, magnetised inertial confinement fusion [119] involves applying a magnetic field across the pellet prior to implosion. The magnetic field is enhanced by compression and produces higher temperature hot spots by restricting electron cooling mechanisms. Experiments have demonstrated a 30% enhancement in the neutron yield using this method [120, 121]. Focus has been on limiting electron transport out of the hot spot but preliminary results show it may be the case that a strong, externally applied magnetic field can also affect fast electron driven shock wave generation by retarding electron transport perpendicular to the field lines and thereby localise energy deposition. The potential to generate experimentally useful, strong magnetic fields has been demonstrated [123–125]. It is not immediately clear if this effect would be beneficial to the magnetised inertial confinement fusion scheme, given its inherently spherical nature. Alternatively, this effect may be of use in planar scenarios and where limited spatial or temporal scales may be an issue. The model is capable of performing studies in more experimentally accessible regimes, say with plastic targets at solid density. This offers up the opportunity to validate the model against experimental data.

Fast electron driven shock wave formation is clearly an area of physics rich with potential applications and interesting fundamental physics. To explore this fully requires a number of improvements to the hybrid model. The need for burn physics and radiation transport has already been mentioned. Further improvements to the hydrodynamic module would include a more realistic equation of state, the effect of magnetic fields and the capability to handle multiple materials.

If a more substantial development task was undertaken it would desirable to have a 2D model with axial symmetry. This would allow for the study of 2D effects on fast electron transport and energy deposition, such as filamentation, as well as the implications of the need for extended lengths of plasma for shock wave formation as it undergoes spherical convergence.

These concluding statements demonstrate the progress that has been made in our understanding of the potential role of fast electrons in shock wave generation in the context of shock ignition but also serve to illustrate a few of the possible directions in which this work can continue. This is, of course, discounting the possibilities that have not yet been considered.

# References

[1] P. Scherrer, C. Frei, R. Whitney, H. W. Schiffer, K. Rose, D. A. Rieser, A. Al-Qahtani, and P. Thomas, *World Energy Scenarios: Composing energy futures to 2050* (World Energy Council, 2013).

[2] J. Nuckolls, L. Wood, A. Thiessen, and G. Zimmerman, Nature **239**, 139 (1972).

[3] J. D. Lindl, P. Amendt, R. L. Berger, S. Gail Glendinning, S. H. Glenzer, S. W. Haan, R. L. Kauffman, O. L. Landen, and L. J. Suter, Phys. Plasmas **11**, 339 (2004).

[4] E. I. Moses, R. N. Boyd, B. A. Remington, C. J. Keane, and R. Al-Ayat, Phys. Plasmas **16**, 041006 (2009).

[5] C. Cavailler, Plasma Phys. Control. Fusion **47**, B389 (2005).

[6] D. Besnard, Eur. Phys. J. D. **44**, 207 (2007).

[7] J. Ebrardt and J. M. Chaput, J. Phys.: Conf. Ser. **244**, 032017 (2010).

[8] J. D. Lindl, Phys. Plasmas **2**, 11 (1995).

[9] M. Tabak, J. Hammer, M. E. Glinsky, W. L. Kruer, and S. C. Wilks, Phys. Plasmas **1**, 5 (1994).

[10] R. Betti, C. D. Zhou, K. S. Anderson, L. J. Perkins, W. Theobald, and A. A. Solodov, Phys. Rev. Lett. **98**, 155001 (2007).

[11] W. L. Kruer, *The Physics of Laser Plasma Interactions* (Addison-Wesley Publishing Company, 2003).

[12] T. E. Fox, A. P. L. Robinson, and J. Pasley, Phys. Plasmas **20**, 122707 (2013).

[13] T. J. M. Boyd and J. J. Sanderson, *The Physics of Plasmas* (Cambridge University Press, 2007).

[14] L. D. Landau and E. M. Lifshitz, *Fluid Mechanics* (Elsevier, 2011), 2nd ed.

[15] L. Spitzer, *Physics of Fully Ionized Gases* (New York: Interscience Publishers, 1956).

[16] Y. T. Lee and R. M. More, Phys. Fluids **27**, 1273 (1984).

[17] Y. B. Zel'dovich and Y. P. Raizer, *Physics of Shock Waves and High-Temperature Hydrodynamic Phenomena* (Dover Publications, Inc., 1966).

[18] M. A. Liberman and Velikovich, *Physics of Shock Waves in Gases and Plasmas* (Springer-Verlag, 1986).

[19] I. P. Shkarofsky, T. W. Johnston, and M. P. Bachynski, *The Particle Kinetics of Plasmas* (Addison-Wesley Publishing Company, 1966).

[20] M. N. Rosenbluth, W. M. MacDonald, and D. L. Judd, Phys. Rev. **107**, 1 (1957).

[21] S. Atzeni, in *Laser-Plasma Interactions and Applications* (Switzerland: Springer, 2013).

[22] M. E. Glinsky, Phys. Plasmas **2**, 2796 (1995).

[23] A. R. Bell, J. R. Davies, S. Guerin, and H. Ruhl, Plasma Phys. Control. Fusion **39**, 653 (1997).

[24] J. R. Davies, A. R. Bell, and M. G. Haines, Phys. Rev. E. **56**, 6 (1997).

[25] J. Meyer-Ter-Vehn, Nucl. Fusion **22** (1982).

[26] S. Atzeni and J. Meyer-ter Vehn, *The Physics of Inertial Fusion* (Oxford: Clarendon Press, 2004).

[27] S. E. Bodner, J. Fusion Energy **1**, 221 (1091).

[28] M. D. Rosen, Phys. Plasmas **6**, 1690 (1999).

[29] R. Betti and C. D. Zhou, Phys. Plasmas **12**, 110702 (2005).

[30] M. C. Herrmann, M. Tabak, and J. D. Lindl, Nucl. Fusion **41**, 99 (2001).

[31] V. A. Shcherbakov, Sov. J. Plasma Phys. **9**, 240 (1983).

[32] W. Theobald, R. Betti, C. Stoeckl, K. S. Anderson, J. A. Delettrez, V. Y. Glebov, V. N. Goncharov, F. J. Marshall, D. N. Maywar, R. L. McCrory, et al., Phys. Plasmas **15**, 056306 (2008).

[33] S. Atzeni, X. Ribeyre, G. Schurtz, A. J. Schmitt, R. Betti, and L. J. Perkins, Nucl. Fusion **54**, 054008 (2014).

[34] S. Atzeni and G. Schurtz, Proc. SPIE **8080**, 808022 (2011).

[35] M. Dunne, Nature Phys. **2**, 2 (2006).

[36] S. Atzeni, A. Schiavi, and C. Bellei, Phys. Plasmas **14**, 052702 (2007).

[37] S. Atzeni, J. R. Davies, L. Hallo, J. J. Honrubia, P. H. Maire, M. Olazabal-Loumé, J. L. Feugeas, X. Ribeyre, A. Schiavi, G. Schurtz, et al., Nucl. Fusion **49**, 055008 (2009).

[38] L. J. Perkins, R. Betti, K. N. LaFortune, and W. H. Williams, Phys. Rev. Lett. **103**, 045004 (2009).

[39] X. Ribeyre, G. Schurtz, M. Lafon, S. Galera, and S. Weber, Plasma Phys. Control. Fusion **51**, 015013 (2009).

[40] D. Batani, S. D. Baton, A. Casner, S. Depierreux, M. Hohenberger, O. Klimo, M. Koenig, C. Labaune, X. Ribeyre, C. Rousseaux, et al., Nucl. Fusion **54**, 054009 (2014).

[41] P. Nicolai, J. L. Feugeas, M. Touati, X. Ribeyre, S. Gus'kov, and V. T. Tikhonchuk, Phys. Rev. E. **89**, 033107 (2014).

[42] A. R. Bell and M. Tzoufras, Plasma Phys. Control. Fusion **53**, 045010 (2011).

[43] S. Gus'kov, X. Ribeyre, M. Touati, J. L. Feugeas, P. Nicolai, and V. T. Tikhonchuk, Phys. Rev. Lett. **109**, 255004 (2012).

[44] X. Ribeyre, S. Gus'kov, J. L. Feugeas, P. Nicolai, and V. T. Tikhonchuk, Phys. Plasmas **20**, 062705 (2013).

[45] J. Breil and P. H. Maire, J. Comput. Phys. **224**, 785 (2007).

[46] B. Dubroca, J. L. Feugeas, and M. Frank, Eur. Phys. J. D. **60**, 301 (2010).

[47] P. Nicolai, J. L. Feugeas, C. Regan, M. Olazabal-Loumé, J. Breil, B. Dubroca, J. P. Morreeuw, and V. T. Tikhonchuk, Phys. Rev. E. **84**, 016402 (2011).

[48] A. R. Bell and R. J. Kingham, Phys. Rev. Lett. **91**, 035003 (2003).

[49] A. R. Bell, A. P. L. Robinson, M. Sherlock, R. J. Kingham, and W. Rozmus, Plasma Phys. Control. Fusion **48**, R37 (2006).

[50] U. Ziegler, J. Comput. Phys. **196**, 393 (2004).

[51] C. K. Birdsall and A. B. Langdon, *Plasma Physics via Computer Simulation* (Taylor and Francis, New York, 1991).

[52] R. J. Kingham and A. R. Bell, J. Comput. Phys. **194**, 1 (2004).

[53] A. P. L. Robinson and M. Sherlock, Phys. Plasmas **14**, 083105 (2007).

[54] M. Tzoufras, A. R. Bell, P. A. Norreys, and F. S. Tsung, J. Comput. Phys. **230**, 6475 (2011).

[55] J. R. Davies, Phys. Rev. E. **65**, 026407 (2002).

[56] J. J. Honrubia and J. Meyer-ter Vehn, Nucl. Fusion **46**, L25 (2006).

[57] S. Kar, A. P. L. Robinson, D. C. Carroll, O. Lundh, K. Markey, P. McKenna, P. A. Norreys, and M. Zepf, Phys. Rev. Lett. **11**, 055001 (2009).

[58] B. Ramakrishna, S. Kar, A. P. L. Robinson, D. J. Adams, K. Markey, M. N. Quinn, X. H. Yuan, P. McKenna, K. L. Lancaster, J. S. Green, et al., Phys. Rev. Lett. **105**, 135001 (2010).

[59] A. P. L. Robinson, Ph.D. thesis, Imperial College London (2005).

[60] P. Colella and P. R. Woodward, J. Comput. Phys. **54**, 174 (1984).

[61] W. H. Press, S. A. Teukolsky, W. T. Vetterling, and B. P. Flannery, *Numerical Recipes in Fortran 77* (Cambridge University Press, 2006), 2nd ed.

[62] C. J. Joachain, *Quantum Collision Theory* (North-Holland, 1987), 3rd ed.

[63] International Commission on Radiation Units and Measurements, Tech. Rep. 37, Bethesda, MD, USA (1984).

[64] A. A. Solodov and R. Betti, Phys. Plasmas **15**, 042707 (2008).

[65] A. Kurganov, S. Noelle, and G. Petrova, SIAM J. Sci. Comput. **23**, 707 (2001).

[66] C. R. Evans and J. F. Hawley, ApJ **332**, 659 (1988).

[67] B. van Leer, J. Comput. Phys. **23**, 276 (1977).

[68] J. D. Huba, *NRL Plasma Formulary* (NRL/PU/6790-98-358, 1998).

[69] R. C. Malone, R. L. McCrory, and R. L. Morse, Phys. Rev. Lett. **34**, 12 (1975).

[70] R. J. Mason, Phys. Rev. Lett. **47**, 9 (1981).

[71] A. R. Bell, R. G. Evans, and D. J. Nicholas, Phys. Rev. Lett. **46** (1981).

[72] J. P. Matte and J. Virmont, Phys. Rev. Lett. **49**, 26 (1982).

[73] A. R. Bell, Phys. Fluids **28**, 6 (1985).

[74] T. H. Kho and M. G. Haines, Phys. Fluids **29**, 2665 (1986).

[75] G. J. Rickard and A. R. Bell, Phys. Rev. Lett. **62**, 23 (1989).

[76] V. N. Goncharov, O. V. Gotchev, E. Vianello, T. R. Boehly, J. P. Knauer, P. W. McKenty, P. B. Radha, S. P. Regan, T. C. Sangster, S. Skupsky, et al., Phys. Plasmas **13**, 012702 (2006).

[77] A. Marocchino, M. Tzoufras, S. Atzeni, A. Schiavi, P. Nicolai, J. Mallet, V. T. Tikhonchuk, and J. L. Feugeas, Phys. Plasmas **20**, 022702 (2013).

[78] E. M. Lifshitz and L. P. Pitaevskii, *Physical Kinetics* (Pergamon Press, 1981).

[79] T. D. Arber and R. G. L. Vann, J. Comput. Phys. **180**, 339 (2002).

[80] G. A. Sod, J. Comput. Phys. **27**, 1 (1978).

[81] M. Brio and C. C. Wu, J. Comput. Phys. **75**, 400 (1988).

[82] C. R. Menyuk, N. M. El-Siragy, and W. M. Manheimer, Phys. Fluids **28**, 3409 (1985).

[83] A. Simon, R. W. Short, E. A. Williams, and T. Dewandre, Phys. Fluids **26** (1983).

[84] C. S. Liu, Phys. Fluids **19**, 967 (1976).

[85] C. Garban-Labaune, E. Fabre, C. E. Max, R. Fabbro, and F. Amiranoff, Phys. Rev. Lett. **48**, 15 (1982).

[86] R. Betti, W. Theobald, C. D. Zhou, K. S. Anderson, P. W. McKenty, S. Skupsky, D. Shvarts, V. N. Goncharov, J. A. Delettrez, P. B. Radha, et al., J. Phys.: Conf. Ser. **112**, 022024 (2008).

[87] O. Klimo, S. Weber, V. T. Tikhonchuk, and J. Limpouch, Plasma Phys. Control. Fusion **52**, 055013 (2010).

[88] O. Klimo, V. T. Tikhonchuk, X. Ribeyre, G. Schurtz, C. Riconda, S. Weber, and J. Limpouch, Phys. Plasmas **18**, 082709 (2011).

[89] O. Klimo and V. T. Tikhonchuk, Plasma Phys. Control. Fusion **55**, 095002 (2013).

[90] S. Weber, C. Riconda, O. Klimo, A. Heron, and V. T. Tikhonchuk, Phys. Rev. E. **85**, 016403 (2012).

[91] C. Riconda, S. Weber, and A. Heron, Phys. Plasmas **18**, 092701 (2011).

[92] R. P. Drake, R. E. Turner, B. F. Lasinski, K. G. Estabrook, E. M. Campbell, C. L. Wang, D. W. Phillion, E. A. Williams, and W. L. Kruer, Phys. Rev. Lett. **53**, 18 (1984).

[93] S. P. Regan, N. B. Meezan, L. J. Suter, D. J. Strozzi, W. L. Kruer, D. Meeker, S. H. Glenzer, W. Seka, C. Stoeckl, V. Y. Glebov, et al., Phys. Plasmas **17**, 020703 (2010).

[94] W. Theobald, K. S. Anderson, R. Betti, R. S. Craxton, J. A. Delettrez, J. A. Frenje, V. Y. Glebov, O. V. Gotchev, J. H. Kelly, C. K. Li, et al., Plasma Phys. Control. Fusion **51**, 124052 (2009).

[95] W. Theobald, R. Betti, K. S. Anderson, O. V. Gotchev, D. D. Meyerhofer, C. Ren, A. A. Solodov, C. Stoeckl, V. A. Smalyuk, J. A. Delettrez, et al., LLE Review **119**, 117 (2009).

[96] W. Theobald, R. Nora, M. Lafon, A. Casner, X. Ribeyre, K. S. Anderson, R. Betti, J. A. Delettrez, J. A. Frenje, V. Y. Glebov, et al., Phys. Plasmas **19**, 102706 (2012).

[97] T. R. Boehly, D. L. Brown, R. S. Craxton, R. L. Keck, J. P. Knauer, J. H. Kelly, T. J. Kessler, S. A. Kumpan, S. J. Loucks, S. A. Letzring, et al., Opt. Commun. **133**, 495 (1997).

[98] P. Koester, L. Antonelli, S. Atzeni, J. Badziak, F. Baffigi, D. Batani, C. A. Cecchetti, T. Chodukowski, F. Consoli, G. Cristoforetti, et al., Plasma Phys. Control. Fusion **55**, 124045 (2013).

[99] S. D. Baton, M. Koenig, E. Brambrink, H. P. Schlenvoigt, C. Rousseaux, G. Debras, S. Laffite, P. Loiseau, F. Philippe, X. Ribeyre, et al., Phys. Rev. Lett. **108**, 195002 (2012).

[100] M. Hohenberger, W. Theobald, S. X. Hu, K. S. Anderson, R. Betti, T. R. Boehly, A. Casner, D. E. Fratanduono, D. D. Meyerhofer, R. Nora, et al., Phys. Plasmas **21**, 022702 (2014).

[101] R. G. Evans, Laser and Part. Beams **1**, 231 (1983).

[102] V. S. Imshennik, Sov. Phys. Dokl. **5**, 263 (1960).

[103] A. P. L. Robinson, D. J. Strozzi, J. R. Davies, L. Gremillet, J. J. Honrubia, T. Johzaki, R. J. Kingham, M. Sherlock, and A. A. Solodov, ArXiv e-prints (2013), `1304.1040`.

[104] G. I. Taylor, Proc. R. Soc. London A **201**, 159 (1950).

[105] L. I. Sedov, *Similarity and Dimensional Methods in Mechanics* (New York: Academic Press, 1959).

[106] G. I. Taylor, Proc. R. Soc. London A **201**, 175 (1950).

[107] R. A. Chevalier, ApJ **207**, 872 (1976).

[108] T. A. Leonard and M. F. J., J. Appl. Phys. **46**, 3562 (1975).

[109] S. F. Gull, M. N. R. A. S. **161**, 47 (1973).

[110] S. F. Gull, M. N. R. A. S. **171**, 263 (1975).

[111] D. F. Cioffi, C. F. McKee, and E. Bertschinger, ApJ **334**, 252 (1988).

[112] R. C. Dohm-Palmer and T. W. Jones, ApJ **471**, 279 (1996).

[113] J. C. Wheeler, T. J. Mazurek, and A. Sivaramakrishnan, ApJ **237**, 781 (1980).

[114] D. L. Book, Shock Waves **4**, 1 (1994).

[115] R. A. Chevalier, ApJ **258**, 790 (1982).

[116] I. R. Lindemuth and R. C. Kirkpatrick, Nucl. Fusion **23**, 263 (1983).

[117] A. Hasegawa, H. Daido, M. Fujita, K. Mima, M. Murakami, S. Nakai, K. Nishihara, K. Terai, and C. Yamanaka, Phys. Rev. Lett. **56**, 2 (1986).

[118] R. C. Kirkpatrick, I. R. Lindemuth, and M. S. Ward, Fusion Technol. **27**, 201 (1995).

[119] O. V. Gotchev et al., J. Fusion Energy **27**, 25 (2008).

[120] P.-Y. Chang et al., Phys. Rev. Lett. **107**, 035006 (2011).

[121] M. Hohenberger et al., Phys. Plasmas **19**, 056306 (2012).

[122] O. V. Gotchev, J. P. Knauer, P.-Y. Chang, N. W. Jang, M. J. Shoup III, D. D. Meyerhofer, and R. Betti, Rev. Sci. Instrum. **80**, 043504 (2009).

[123] H. Daido, F. Miki, K. Mima, M. Fujita, K. Sawai, H. Fujita, Y. Kitagawa, S. Nakai, and C. Yamanaka, Phys. Rev. Lett. **56**, 8 (1986).

[124] C. Courtois, A. D. Ash, D. M. Chambers, R. A. D. Grudy, and N. C. Woolsey, J. Appl. Phys. **98**, 054913 (2005).

[125] S. Fujioka, Z. Zhang, K. Ishihara, K. Shigemori, Y. Hironaka, T. Johzaki, A. Sunahara, N. Yamamoto, H. Nakashima, T. Watanabe, et al., Sci. Rep. **3**, 1170 (2013).